Mapping the Elastic Response of Epithelial Apical Cell Membranes Suspended Across Porous Array

Dissertation
zur Erlangung des Grades
"Doktor der Naturwissenschaften"
im Promotionsfach: Chemie

am Fachbereich Chemie, Pharmazie und Geowissenschaften
der Johannes Gutenberg-Universität Mainz

Tamir Fine

Mainz, 2009

Dekan: Prof. Dr. D.Sc. h.c. Wolfgang Hofmeister

Tag der mündlichen Prüfung: 14.01.10

ABSTRACT

As the elastic response of cell membranes to mechanical stimuli plays a key role in various cellular processes, novel biophysical strategies to quantify the elasticity of native membranes under physiological conditions at a nanometer scale are gaining interest. In order to investigate the elastic response of apical membranes, elasticity maps of native membrane sheets, isolated from MDCK II (Madine Darby Canine kidney strain II) epithelial cells, were recorded by local indentation with an Atomic Force Microscope (AFM). To exclude the underlying substrate effect on membrane indentation, a highly ordered gold coated porous array with a pore diameter of 1.2 μm was used to support apical membranes. Overlays of fluorescence and AFM images show that intact apical membrane sheets are attached to poly-D-lysine coated porous substrate. Force indentation measurements reveal an extremely soft elastic membrane response if it is indented at the center of the pore in comparison to a hard repulsion on the adjacent rim used to define the exact contact point. A linear dependency of force versus indentation ($-dF/dh$) up to 100 nm penetration depth enabled us to define an apparent membrane spring constant (k_{app}) as the slope of a linear fit with a stiffness value of $(0.56 \pm 0.3)\, mN/m$ for native apical membrane in PBS. A correlation between fluorescence intensity and k_{app} is also reported. Time dependent hysteresis observed with native membranes is explained by a viscoelastic solid model of a spring connected to a Kelvin-Voight solid with a time constant of 0.04 s. No hysteresis was reported with chemically fixated membranes. A combined linear and non linear elastic response is suggested to relate the experimental data of force indentation curves to the elastic modulus and the membrane thickness. Membrane bending is the dominant contributor to linear elastic indentation at low loads, whereas stretching is the dominant contributor for non linear elastic response at higher loads. The membrane elastic response was controlled either by stiffening with chemical fixatives or by softening with F-actin disrupters. Overall, the presented setup is ideally suitable to study the interactions of the apical membrane with the underlying cytoskeleton by means of force indentation elasticity maps combined with fluorescence imaging.

TABLE OF CONTENTS

1. INTRODUCTION

The plasma cell membrane functions as a continuous dynamic interface between the cell interior and the extracellular environment (Yeagle 2005, Alberts 2005). Cell membranes react rapidly to morphological changes of the cells as well as to the chemical and physical conditions of their environment by shape readjustments and curvature formation (McMahon and Gallop 2005, Steltenkamp et al. 2006, Dai et al. 1998). In addition, apical membranes of epithelial cells also exhibit stabilized curvatures which exist permanently in the form of microvilli (McMahon and Gallop 2005). Membrane shape readjustments are necessary to maintain the homostasis of cells in various dynamic processes, such as osmolarity, cellular division, differentiation, growth, death, locomotion, migration, viral budding, and vesicle trafficking. Therefore, quantitative data for cell mechanics on various length scales is pivotal in understanding how cells respond to external mechanical stresses.

The physical properties of cell membranes: softness, heterogeneity and flexibility, allow the deformation of cells as a response to external forces that are routinely present in the cellular environment. A material reservoir in the form of surface folds and invaginations enables the membrane to buffer alterations in tension (Raucher and Sheetz 1999) in order to accommodate area changes (stretching). The external mechanical stress applied on epithelial apical membranes is borne largely by actin filaments (Janmey 1996). Actin filaments form an underlying support to bind the membrane to the cytoskeleton and to the junctions between neighboring cells. These filaments are characterized by a persistence length of 18 μm, which is mostly suitable to resist tension applied on the cell. Biophysical techniques to measure elasticity of cells include micropipette aspiration (Xu and Shao 2008), cell poking (Daily et al. 1984), optical tweezers (Hochmuth et al. 1996), magnetic beads (Bausch et al. 1998), and the Atomic Force Microscope (Rotsch and Radmacher 2000). The latter is a powerful tool to investigate the elasticity of both living cells and native membranes due to two main reasons: (1) the sensitivity of the AFM allows the detection of a wide range of forces-from 5 pN to 100 nN (Müller et al. 2009). (2) It provides high spatial resolution under physiological conditions which is mostly suitable for elasticity mapping of heterogeneous biological samples, such as native membranes. The elastic response is measured by force indentation curves and analysis of the approaching curve with a proper contact model (A-Hasssn et al. 1998, Steltenkamp et al. 2006, Zelenskaya et al. 2005, Mathur et al. 2001). In addition, it is feasible to combine AFM with optical microscopes to correlate structure with mechanics.

In this work, the AFM was also used as a nanoindenter together with fluorescence imaging in order to characterize the elastic response of native apical membranes prepared from the MDCK II kidney epithelial cell line (Sambuy and Rodriguez-Boulan 1988). Differentiated epithelial cells are polarized, meaning that they exhibit both structural and functional segregation between the apical and the basolateral membranes facing the extracellular environment and the underlying cultivating substrate, respectively (Simons and Ikonen 1997, Nelson and Veshnock 1986, Ojakian and Schwimmer 1998). The apical membrane of MDCK cells is characterized by microvillar and planar

sub domains (Poole et al. 2004, McAteer et al. 1986). Recently, a new method to address the elastic properties of MDCK II basolateral membrane fragments was reported by using porous substrate in conjunction with indentation experiments carried out with an AFM (Lorenz et al. 2009). In this thesis, the elastic response of the MDCK II apical membrane was investigated from two types of samples: (1) Whole cells cultivated on a porous chip. (2) Apical membrane fragments detached from living cells and transferred to a gold coated functionalized chip, thereby possessing the properties of the initial cellular membrane. In comparison to elasticity measurements of apical membranes recorded from whole cells, those with isolated membranes allow accurate analysis by excluding the influence of inner cellular structures, such as organelles, the cells' cytoskeleton and osmotic pressure, on the membrane elastic response. In the present investigation, a highly ordered porous Si/SiO_2 chip was used as a substrate (Danelon et al. 2006, Lorenz et al. 2009) since it provides three main advantages over a solid support: (1) $SiSO_2$ substrate is biocompatible and it can be functionalized to support isolated membranes. (2) As the membrane sheets seal the pores, it allows free indentation across the pores with an AFM tip without disturbance from the underlying stiff substrate. For thin deformable films, such as cell membranes, the effect of the supported substrate on the recorded elastic response cannot be neglected (Dimitriadis et al. 2002). Hence, the use of a porous substrate improves the measurement's accuracy. Soft sample in liquid possess surface forces, such as van der Walls and adhesion, which can cause significant deformation even before a tip-sample contact is established (Peticha and Sutton 1988, Butt et al. 2005). Therefore, force indentation curves were also recorded from the adjacent rim in order to estimate the exact contact point. (3) The special geometry of the porous substrate can also serve as a grid to localize isolated membranes with optical microscopes for AFM measurements (Lorenz et al. 2009).

Overall, in order to elucidate physical properties of epithelial apical membranes, elasticity maps of free standing native and chemically treated isolated membranes were carried out together with fluorescence and force modulation measurements. In addition, high resolution images of the apical cell surface of MDCK II cells were recorded in order to shed light on the topographical organization of apical membrane microvilli.

1.1 Epithelial cells

In vivo, epithelial cells line the cavities and the free surfaces of the external and the internal parts of the body to form a permeability barrier between two compartments (Alberts 2005). For instance, transporting epithelial cells form a barrier between the blood supply and the ultrafiltrate in the kidney. For this function the cells are tightly bound together into sheets by cell-cell adhesion protein complexes which allow only vectorial transport of ions and solutes (Yeaman et al. 1999). Cell polarization is initiated by cues originating from the cell-cell contacts and the extracellular matrix (Drubin and Nelson 1996). These signals induce the formation of basal membrane domains which transmit signals to the cytoskeletal filaments (actin and microtubules) and the endocytic apparatus to reorganize the plasma membrane and the cytoplasm (figure 1.0). Polarized epithelial cells consist of

an apical membrane with microvilli facing the lumen and a basolateral membrane contacting the neighbouring cells and the underlying extracellular matrix.

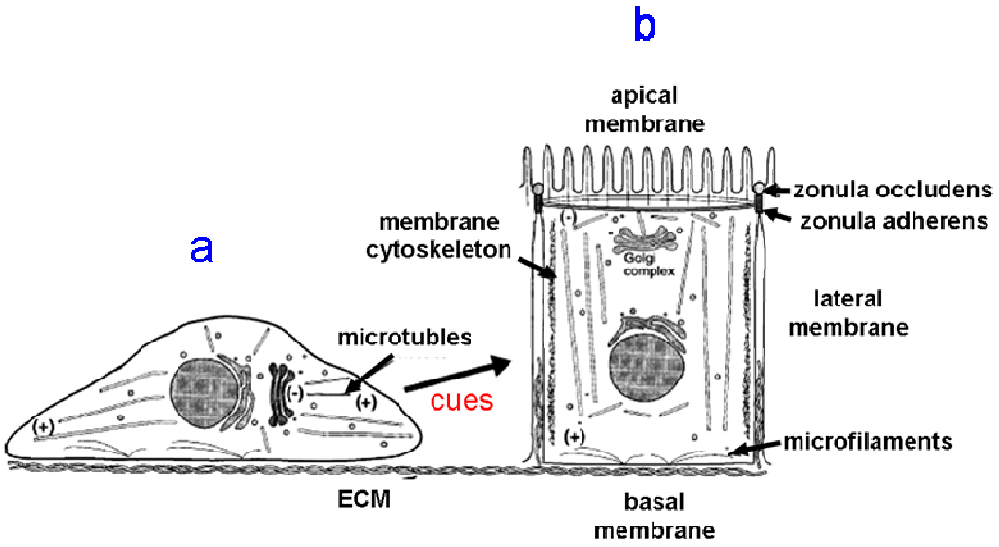

Figure 1.0: Comparison between non-polarized (a) and polarized (b) epithelial cell. Extrinsic cues originating from cell-cell and cell extracellular matrix contacts initiate cell polarization leading to a complete separation between the apical and the basolateral membranes (Yeaman et al. 1999).

Cell polarization is maintained by tight junctions and intracellular sorting of membrane components. Proteins are sorted in the *trans*-Golgi-network (TGN) into distinct vesicles, which are delivered either to the apical or to the basolateral membrane domains (Simons and Wandinger-Ness 1990). There are four kinds of membrane junctions (figure 1.1) between neighboring cells:

1) Tight junctions. 2) Adherens junctions. 3) Gap junctions. 4) Desmosomes.

Tight junctions seal adjacent epithelial cells in a narrow band just beneath the apical membrane, thus blocking the movement of integral membrane proteins between the apical and the basolateral membrane poles. In addition, they function as gates to regulate the solute flux across the cell membrane. They are constructed from three types of transmembrane proteins: Occludin, Claudins and Junctional Adhesion Molecules. These proteins are connected with the actin cytoskeleton by adaptor proteins, such as Zona Occludens 1 (ZO1), ZO2 and ZO3. Some of these proteins can also act as receptors for several viruses and bacterial toxins. Adherens junction proteins are responsible for initiating and maintaining cell-adhesion and they are composed of E-Cadherins (Calcium dependent adhesion molecules) and Catenins. E-cadherins from adjacent cells are bound together at the cell borders and they are connected to the cytoskeleton by Catenins. Gap junctions are intercellular channels with a diameter of 2 nm. They consist of 6 copies of transmembrane proteins called connexins enabling small molecules up to a molecular weight of 1 kDa to pass through. Desmosomes are localized patches that keep two adjacent cells tightly together. They are bound to intermediate filaments, such as Keratin. A monolayer of epithelial cells is regarded as simple epithelium whereas two or more layers of cells are called compound epithelium. Simple epithelial cells consist of distinct

apical and basolateral endocytic trafficking pathways (Bomsel and Alfsen 2003). They function as vesicular transporters used for recycling, degradation and transcytosis from one pole of the membrane to the opposite one.

The extracellular matrix (ECM) is a complex mixture of structural and functional macromolecules, which play a key role in tissue and organ morphogenesis as well as cell structure and function (Rosso et al. 2004). *In vitro*, cells form their own ECM as they come in contact with matrices and scaffolds. They synthesize different types of molecules in the surrounding space, according to a well defined program of differentiation (Adams and Watt 1993). The ECM provides a continuous flow of signals from the extracellular environment to the cells in order to maintain cell proliferation and organization. It is composed of five groups of macromolecules: (1) Collagens: proteins responsible for cell attachment, spreading, cell differentiation and movement. (2) Glycosaminoglycans (GAGs): linear polysaccharides formed by repeating disaccharide units. (3) Adhesive glycoproteins: responsible for cell binding and contain repeated amino acid sequences. For example: RGD (Arg-Asp-Val), LDV (Leu-Asp-Val) and REDV (Arg-Gly-Asp-Ser). (4) Elastic fibers: composed of the protein elastin. (5) Proteoglycans: forming specific complexes responsible for hydration and spatial organization. In addition, they act as receptors on the cell surface and bind to collagen and growth factors.

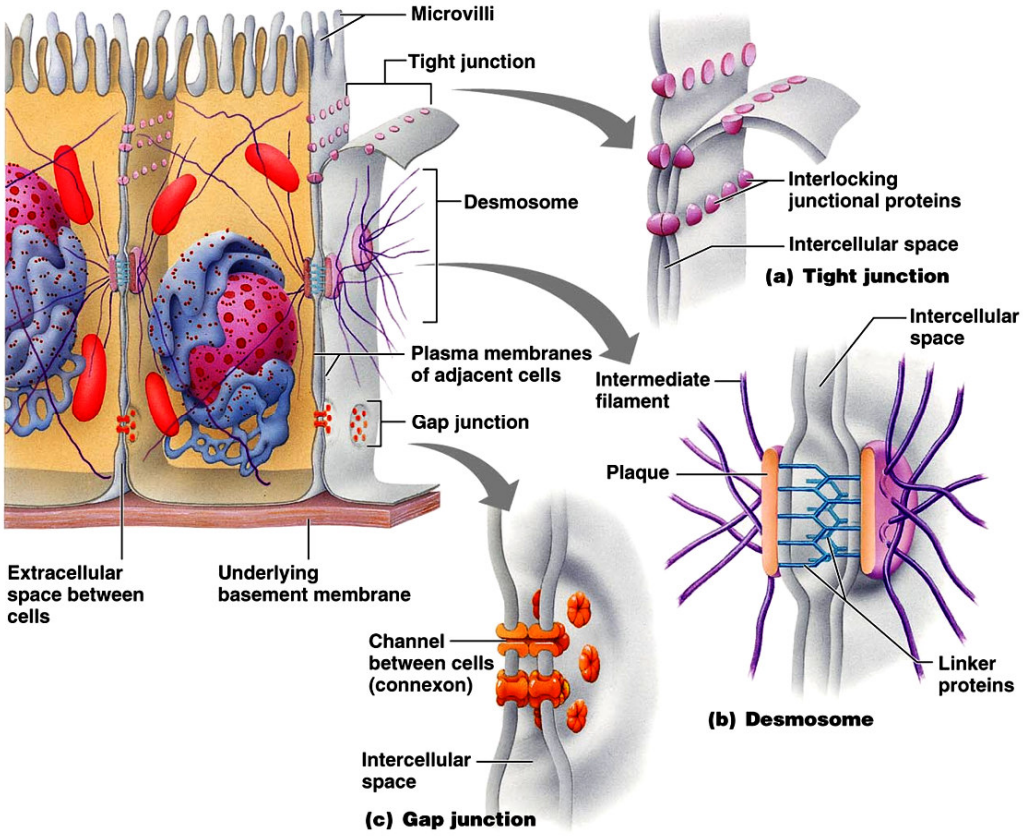

Figure 1.1.: Schematic of columnar polarized epithelial cells showing the apical (microvilli) and basolateral (facing the basement membrane) plasma membrane domains. Cellular junctions (a-c) are located at the lateral membrane between adjacent cells. (Marieb 2000)

1.2 MDCK cells

The adherent epithelial MDCK II (Madin-Darby canine kidney, strain II) cell line was used (figure 1.2) to prepare apical membranes out of three main reasons: (1) it is a well characterized cell line showing features of distal kidney tubular transporting epithelia. (2) It allows the preparation of both apical and basolateral membrane fragments. (3) This cell line is robust and the cells are able to form a monolayer with firm contacts on Si/SiO_2 porous substrate. This cell line was originated from the distal tubule of a dog kidney (ATCC-CCL34). MDCK I and MDCK II are two cell sublines which differ in their trans-epithelial electrical resistance, 3000 ohm/cm^2 and 100 ohm/cm^2, respectively (Shaw 2002). Transepithelial resistance is an indicator for the cell monolayer tightness. Both cell lines retain many of the differentiated properties of transporting epithelia, such as the formation of functional tight junctions, apical and basolateral membrane domains, apical membrane microvilli, a primary cilium, vectorial ion transport, and polarized distributions of plasma membrane lipids and glycoproteins. *In vitro*, Apical-basolateral segregation begins at around 24 h following cell seeding (Meder et al. 2007) and it is completed after 3 days of cell cultivation (figure 1.1D).

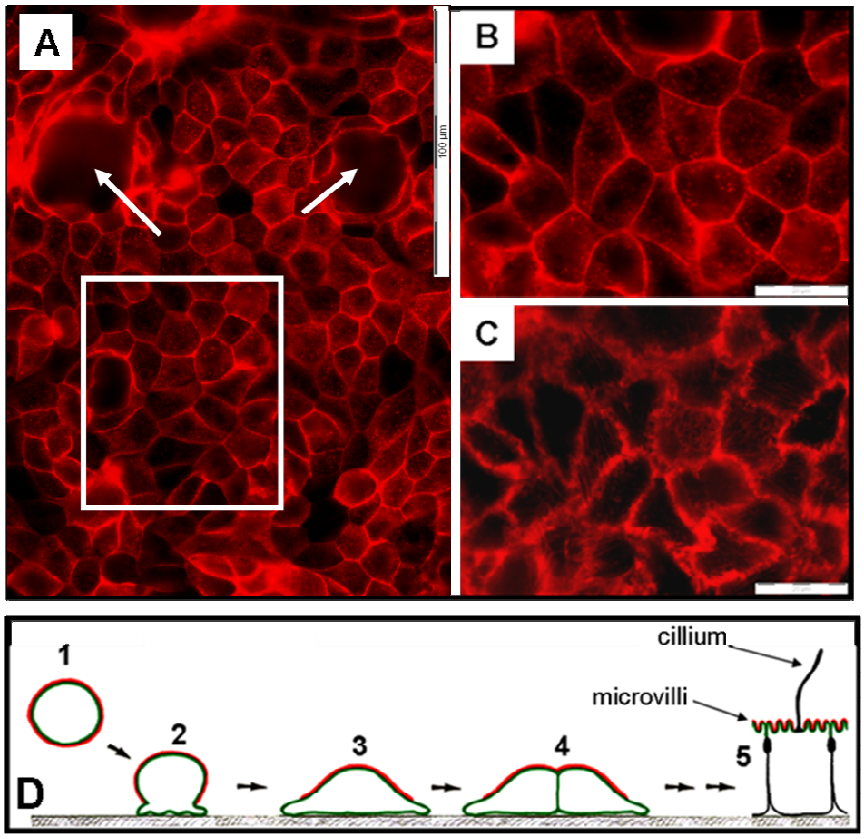

Figure 1.2: Confluent MDCK II cell monolayer. F-actin was labeled with *Phalloidin*-Alexa546. A: Hemicysts (domes) are marked with arrows. Scale bar is 100 µm. Top (B) and bottom (C) views of the cells refer to the marked area in A. Scale bar is 20 µm. D: Schematic of MDCK II membrane polarization process (Meder et al. 2007). 1: Cells in suspension. 2: Cell attachment to substrate. 3: Beginning of apical-basolateral membrane domain separation. 4. Cell monolayer formation. 5. The green and the red contours represent apical membrane proteins. Fully differentiated cells consist of apical membrane proteins, microvilli and a primary cilium.

1.3 Plasma cell membrane organization

The plasma membrane (Plasma from Greek *plassein*: to mold) is the outer surface of the cell which separates the intracellular volume from the outside environment. It forms a semipermeable barrier for the exchange of molecules between the cell and its environment as water and small molecules can diffuse freely through the membrane. In addition, the membrane provides mechanical support for polymer networks, such as F-actin, it regulates the osmotic pressure of the cell and it takes part in the cellular signal transduction processes. Plasma membranes consist of a 5-10 nm non homogeneous lipid bilayer, exoplasmic and cytoplasmic leaflets, to which proteins are attached by their hydrophobic domains. The cell lipid bilayer is composed of amphiphilic molecules of fatty acids with a hydrophilic head group and two long lipophilic hydrocarbon chains. The name lipid comes from Greek word *lipos*, for fat. Lipid compounds dissolve in nonpolar solvents, such as choloroform or diethyl ether and they are defined by the physical operation used to isolate them. Faty acids are long-chain carboxylic acids that are mostly found as esters of glycerol, that is, triacylglycerol.
The overall lipid composition, which makes about 50% of the membrane mass, (depending on the cell type), is as follows: glycerophospholipids (50-90%), glycolipids (5%), and cholesterol (5-25%).

Glycerohospholipids contain saturated and unsaturated hydrocarbon chains, C_{16}-C_{18} atoms in length, connected to a hydrophilic head group of glycerol by a phosphate ester bond. Double bonds in the hydrocarbons chains are usually in cis configuration resulting in a kink of the chain (Boal 2002). Glycerophosphlipids are possible acceptors for hydrogen bonds (Cremesti et al. 2002). Phosphatidylcholine (PC) is the most abundant phospholipid in the exoplasmic leaflet of the membrane, whereas phosphatidlethanolamine (PE) and phosphatidylserine (PS) are concentrated in the inner membrane leaflet (Allan 1996).

Glycosphingolipids are present on the outer leaflet of the cell membranes, possessing antigenic properties and act as receptors for antibodies, lectins and certain toxins (Cremesti et al. 2002). They are the major lipid component in epithelial brush border apical membranes, consisting of a hydrophilic oligosaccharide chain linked glycosidically to ceramide (Yeagle 2005). It is composed of a long chain amino alcohol sphingosine substituted with an acyl fatty acid, C_{16}-C_{24} in length. Since these lipids are saturated and hydroxylated, they act as potential donors and acceptors of hydrogen bonds (Cremesti et al. 2002). Tight interactions between ceramide-rich molecules due to the formation of extensive hydrogen bonds give rise to phase separation between ceramide-rich and ceramide-poor molecules (Kolesnick et al. 2000). According to the sugar chains, glycosphingolipids can be classified into cerebrosides and gangliosides (figure 1.3). In cerebrosides, mono or polysaccharide chains are linked to a ceramide, whereas in gangliosides a sugar chain, composing of N-acetyl-neuraminic acid, galctose and glucose, is linked to the C-1 hydroxyl group of ceramide (Yeagle 2005).

Cholesterol is an unsaturated alcohol of four planar aromatic rings with one polar OH group and an isooctyl hydrocarbon attached to a cyclopentanyl ring at carbon 17. All side chains are located on the same side of the ring in ß configuration which restricts the motion of neighboring lipids. Cholesterol reduces the permeability of the membrane and increases its mechanical stress and it takes part in the formation of domains such as rafts and caveolae (Barenholz 2002). It orients in the membrane with its OH group positioned towards the aqueous interface in the surrounding of an ester bond of glycerophospholipids. The cell adjusts the lipid composition of its membranes in order to maintain the membrane fluidity irrespective of the ambient temperature and of other external conditions.

Lipids can also be classified by their molecular shape (Burger 2000): (1): Cylinder shaped lipids, consisting of a head group and hydrophobic alkyl domains of similar diameter, include phospholipids with long alkyl chains found in cell membranes: PC, PS and sphingomyelin. These lipids self associate to a bilayer structure. (2) Cone shaped lipids such as PE, consisting of a small head group relative to the hydrophobic domains, self associate to an inverted micellar structure. This group of lipids induces a negative spontaneous curvature by promoting the bending of a membrane towards the extracellular medium. (3) Inverted cone shape lipids contain a large head group relative to a small hydrophobic domain. This type of lipids, including single chain lipids, phospholipids with short alkyl groups (8 or less) and detergents, induces a positive spontaneous curvature which corresponds to membrane bending towards the cytoplasm.

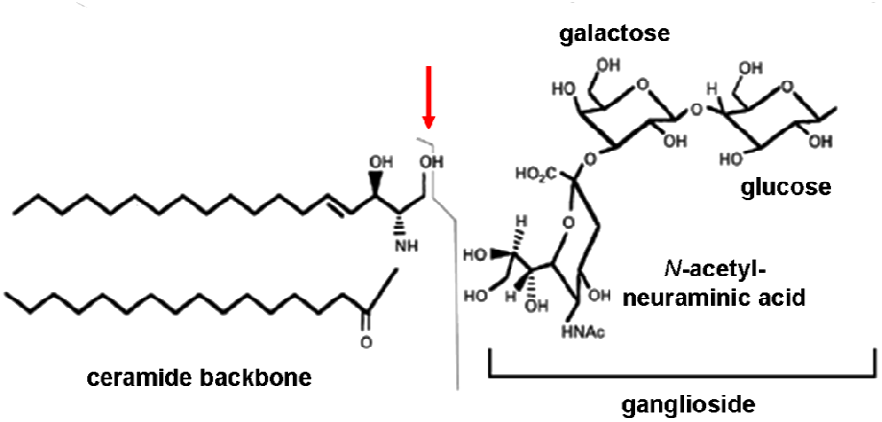

Figure 1.3: Schematic of a ganglioside with a ceramide backbone. The red arrow points at the C-1 hydroxyl group of ceramide where the sugar chain is linked. (Merrill et al. 2001).

Membrane proteins take part in various biological functions, including signal transduction, endocytosis, and ion channels. Around 30% of the open reading frames in the human genome encode membrane proteins and they serve as target for the majority of drugs used. Membrane proteins are classified into two main groups: integral and peripheral proteins. Integral proteins can be further categorized into two subgroups: (1) Transmembrane proteins, which cross the membrane by direct hydrophobic interactions with the lipids. (2) Lipid anchored proteins that use a lipid anchor, named glycosylphosphatidylinositol (GPI), to bind indirectly to sphingolipids in the membrane. These

proteins are either exoplasmic or cytoplasmic such as kinase proteins. Peripheral proteins attach noncovalently to the integral proteins and they are loosely bound to the membrane.

The fluid-mosaic model (Singer and Nicolson in 1972) describes the membrane as a lipid bilayer with freely diffused proteins (figure 1.4). The lipids are in a disordered liquid state, meaning that they can diffuse freely and mix in the plane of the bilayer leaflet.

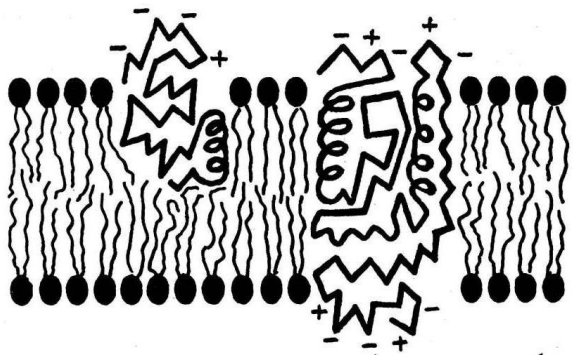

Figure 1.4.: Schematic of plasma membrane cross section with transmembrane (integral) proteins. Hydrophilic parts (+/-) of the proteins face the aqueous solution (cytoplasm or extracellular), whereas the hydrophobic parts are buried inside the membrane (Singer and Nicolson 1972).

The mosaic is made of proteins that are inserted into the fluid membrane. Membrane assembly is governed by the hydrophobic force, as lipids form a bilayer to minimize their contact with water. This force is also responsible for keeping the proteins inside the membrane as the hydrophobic parts of the proteins interact with the lipids, whereas their charged polar groups face the aqueous environment. The absence of strong attractive forces keeps the membrane both fluid and deformable.

As models for cell membrane organization are still evolving, the updated concept suggests that cell membranes consist of lipid domains and subdomains (Simons and Ikonen 1997). For example, differentiated epithelial cells consist of apical and basolateral membrane domains. The apical membrane is enriched with sphingomyelin, glycosphingolipids which form together with cholesterol dynamic lipid domains termed rafts. Lipid rafts are about 20 nm in size (Pralle et al. 2000) assembled by self association of long saturated hydrocarbon chains. Lipid rafts are organized in liquid ordered phases among the liquid disordered phase of the non raft membrane region (Brown and Laondon 1997). Another group of lipid domains includes endocytic membrane invaginations which are formed spontaneously together with membrane bound proteins, such as caveolin and clathrin (Sens and Turner 2004). Caveolae are 100 nm Ω-shaped invaginations (Rothenberg et al. 1992) involved in signal transduction and intracellular transport (Gilbert et al. 1999). Overall, the cell membrane functions as an important co-player in various physiological and pathological processes, such as signal transduction, vesicle trafficking, viral budding, osmotic pressure homeostasis, adhesion and tension regulation (Raucher and Sheetz 1999).

1.4 Apical membrane

In vivo, the apical membrane of renal epithelial cells is defined as the membrane part facing the cavity of the nephron. It can be described in terms of microvillar and planar subdomains with an outer coating layer of glycocalyx, which is about 70-100 nm in thickness. This layer consists of a large number of negatively charged sugar moieties of proteoglycans (PG) and glycosaminoglycans (GAGs) that are tightly connected to the microvillar cell surface (Kovbasnjuk and Spring 2000). PGs are uncovalently bound to GAGs through cationic bridges, whereas GAGs are bound to the transmembrane proteins. The glycocalyx layer limits the diffusion of molecules based on size and surface charge. Microvilli are hair like membrane folds projecting from the apical membrane surface with an outer diameter of 60-70 nm (Lange and Gratzke 2001). The length of a single microvillus varies among cells, up to a maximal length of 80 μm reported from the epithelial cells lining the epididymis (Pacini et al. 1980). An average length of 0.4 μm was reported from kidney epithelial cells (Gorelik et al. 2003). The microvillar apical membrane surface is a typical feature of differentiated epithelial cells during arrested growth (Go/G1) phases (Drenckhahn and Dermitzel 1988, Friedrich et al. 1989). Microvilli are formed by exocytic vesicles transported from the golgi complex to the apical membrane to form microvilli nucleation sites (Lange and Gartzke 2001). In rapidly growing undifferentiated cells, exocytic vesicles, containing lipids and proteins, are integrated into the plasma membrane by forming small surface protrusions (blebbing). Both lipids and proteins are inserted into the membrane by lateral diffusion (figure 1.5A). During cell differentiation, triggered by depletion of metabolic substrates and serum factors at high cell density, a layer of proteoglycans stabilize the exocytic vesicles (figure 1.5B). As a result, microvilli nucleation sites are formed, whereas lateral diffusion of proteins and lipids from the vesicles into the membrane is inhibited. Actin filaments growing into the nucleation sites (figure 1.5C) form microvillar shaft structures. The molecular scaffold of microvilli is composed of a parallel actin bundle (PAB) which are organized in uniform polarity and they are cross linked by actin binding ptoteins (ABP), such as espin, villin and fimbrin (DeRosier and Tilney 2000). Microvilli's length is tightly regulated by a balance of actin polymerization and depolymerization (Loomis et al. 2003). It was found out that the ABP espin initiates microvilli elongation by cross linking two F-actin binding sites from opposed filaments. An initial elongation rate of 5 nm/s was recorded from living A6 kidney epithelial cells by using Scanning Ion Conductance Membrane Microscopy (Gorelik et al. 2003), suggesting a dynamic process of actin assembly and disassembly. For instance, extreme elongation of microvilli on the apical side of neuronal cells was reported following metabolic stress (Shepard and Park 1994). During microvilli elongation lipids flow from the plain membrane surface into the growing microvilli serving as lipid sinks. The transition from a planar surface of the membrane into the microvillar shaft results in spatial lipid crowding due to the difference between the circumference of the inner and the outer membrane leaflet (figure 1.5D). Consequently, about 10-15% of the lipids have to relocate (flip) to the inner leaflet in order to match the spatial organization. The tip of a microvillus is termed:

"entrance compartment" (Lange et al. 1996), which is separated from the cytoplasm by a tight bundle of actin filaments serving as an efficient diffusion barrier. It also allows the microvilli to take part in the natural defense system of the cells against environmental hazardous, such as lipophilic compounds.

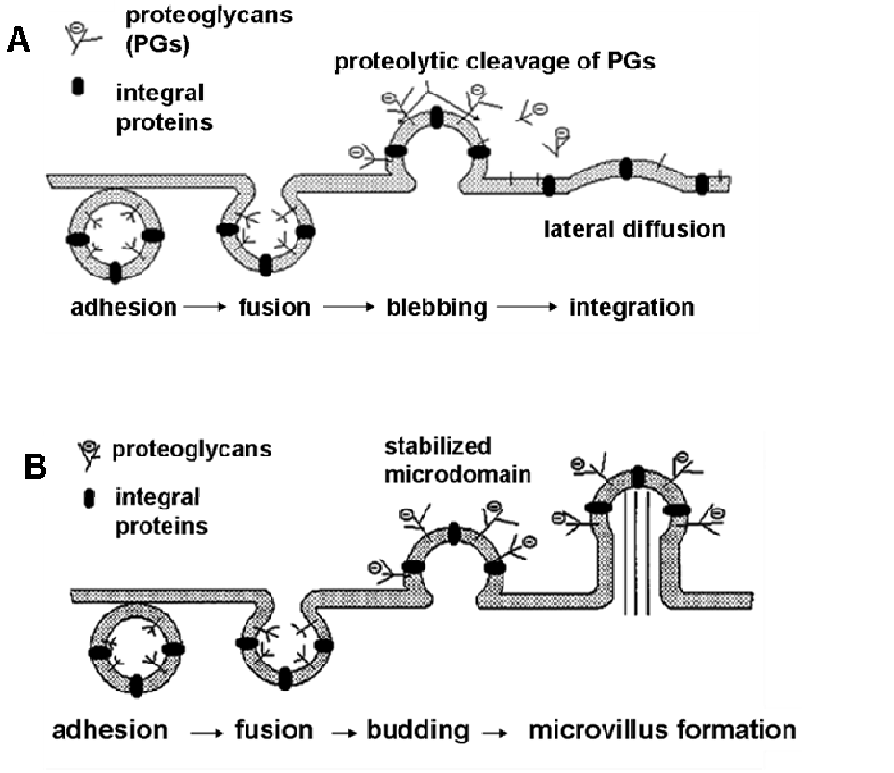

Figure 1.4.: A: Exocytosis of lipids and proteins to the membrane. B: Formation of apical membrane microvili during cell differentiation. C: Microvilli nucleation sites leads to the formation of microvilli schafts. D: Mircovilli cross section with an outer diameter of 60 nm, inidicating the lipid flipping zone due to the circumference between the inner and the outer membrane leaflet. (Lange and Gartzke 2001)

Microvilli increase the membrane surface area, thus increasing the cell absorptive capacity and the available area for transport and enzymatic activity. On cultured cells they increase the surface area to facilitate spreading and cytokinesis without causing membrane rupture. In addition to that they are also capable of contracting like fingers flexing. A simple calculation to evaluate the contribution of microvilli to the cell's surface area is based on the ratio of a hemisphere (microvillus) to its two-

dimensional projection, which is 2 (Colarusso and Spring 2002). A more comprehensive approach to model microvillous membranes is based on a periodic function (Aizenbud and Gershon, 1982):

$$Z = A\cos\left(2\pi l_x^{-1} x\right)\cos\left(2\pi l_y^{-1} y\right).$$

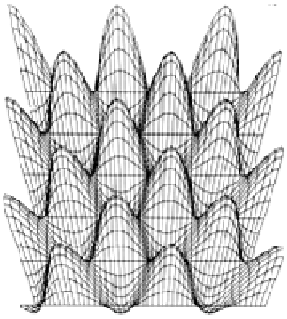

Figure 1.6.: Two dimensional representation of the periodic equation for non planar membrane surface, where A = 0.75 μm and $l_x = l_y = 0.2$ μm (Aizenbud and Gershon, 1982).

Z is the microvillus membrane surface, A is the the microvillus' length and l_x and l_y refer to the length of the unit cell dimensions along x and y. The surface is considered periodic along x and y resembling the surface of an" egg carton" (figure 1.6).

The apical membrane of fully differentiated mammalian cells consists of a single primary non-motile cilium (Anderson et al. 2008). Primary cilia function as mechanosensors and chemosensors coated by the plasma membrane and connected to the cytoplasmic mictotubules. It has an axoneme structure of nine doublet microtubules which extend from the basal body. Since primary cilia lack a central pair of micotubules, they are designated: 9+0. The length of primary cilia expressed in epithelail epithelial kidney cells can reach up to 55 μm, whereas those of MDCK cells are about 8 μm in length (Praetorius and Spring 2001). Malfunction of the primary cilium is related to several human diseases (Yoder 2007), such as the Autosomal Dominant Polycystic Kidney Disease (ADPKD).

1.5 Force resisting filaments

The response of cells to mechanical stress, termed mechanotransduction, is controlled by the cytoskeleton. It is composed of three types of filaments (figure 1.5): F-actin microfilament (F for filamentous), intermediate filaments (IF) and microtubles (MT). These filaments are linear polymers of the proteins actin, vimentin and tubulin, respectively, determining the rheological properties of the cell. Based on their chemical structure, they can be categorized (Käs et al. 1996) as semiflexible (F-actin), rod like (MT) and flexible (IF). On the one hand, in order to carry out biological functions, such as cell division and movement, the cytoskeletom must by highly deformable. On the other hand it must also be rigid in order to maintain the structural integrity of the cell. Both actin filaments and microtubules are able to polymerize and depolymerize rapidly according to the cells' needs, whereas intermediate filaments are less dynamic (Steltenkamp et al. 2006). F-actin is a semi-flexible polymer of G-actin (globular-actin) monomers forming a network of double helix structures of two polymer chains (figure 1.7d2). A filament is defined as semi-flexible if its persistence length is of the same

order as its contour (Wagner et al. 2007). The persistence length is a mechanical property relating to the part of the filament which appears straight. It is related to the distance between two cross links of the filament network and it can be derived from images recorded in light, electron or atomic force microscopy. The ratio between the length of the filament and its persistence length determines its stiffness (Käs et al. 1996).

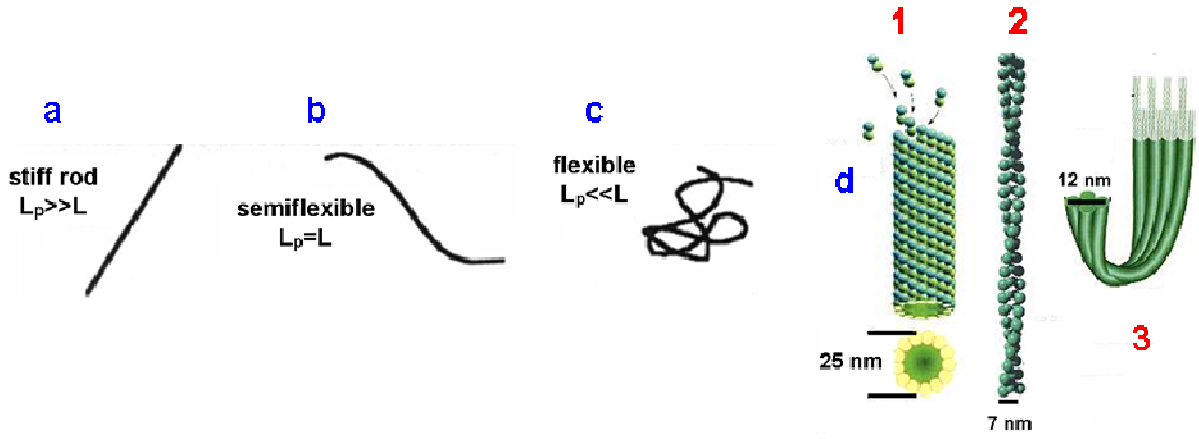

Figure 1.7: The relation between the polymer's length, *L*, and its persistence length, L_p, determines its stiffness (Käs et al. 1996). The letters a, b, and c refers to microtubules (d1) F-actin (d2) and intermediate filaments (d3), respectively. Flexible polymers, such as intermediate filaments, exhibit overlapping random coil configuration. d: illustration from: www.tutorvista.com

Quantitatively, the persistence length (λ_p) can be defined as follows (Wagner et al. 2007): $K = \frac{\lambda_p}{k_B T}$.

K refers to the applied force which is required to deform a filament: $K = E\pi\frac{a^4}{4}$. *E* is the Young's modulus, *a*: the filament's radius and kB_T: thermal energy.

Actin filaments can elongate up to an order of 100 µm with a persistance length of 18 µm which is very long compared to synthetic polymers but significantly shorter than that of MT, 5000 µm (Gitts et al. 1992). They play a multifunctional role in cells, such as cell motility driven by gel-sol transitions of actin networks, force generation in muscles, resistance to the cellular tension and the formation of membrane extensions in the form of lamellopodium and microvilli. Each filament is 7 nm wide with a mass per unit length of: 16 kDa/ nm. G-actin has a molecular mass of 42 kDa and cellular concentration of 1-5 mg/ml. G actin monomers associate spontaneously at the ends of the filaments near the plasma membrane. The growth rate at the two ends: pointed and barbed are different. The pointed end is more static with a low growth rate, whereas the barbed end is more dynamic with a faster growth rate. This process can be stopped by capping proteins that bind to the growing ends. F-actin filaments are mostly concentrated beneath the cell membrane as a network called "terminal web". These networks are cross linked mainly by α-actinin and filamin exhibiting the highest cellular filament rigidity that fluidize when high strains are applied (Janmey et al. 1991). This characteristic is

consistent with the function of F-actin in cell motility, as stable protrusions can deform rapidly in response to controlled filament rupture. In addition, they structure the cell-cell junctions and cytoplasmic projections such as microvilli and pseudopodia. Actin filaments can also form dense rigid bundles that are cross linked with the molecular motor myosin. These bundles termed stress fibers are capable of force generation for cell contraction, cytoskeleton reorganization and compression resistance (Stamenovic and Ingber 2002).

Ifs are 12 nm in diameter (figure 1.7d3) and they are clustered around the nucleus, radiating peripherally to contact the cell borders. Their molecular composition differs among cell types (Herrmann and Harris 1988). The main intermediate filament protein expressed in epithelial cells is keratin, which is divided into type I and type II according to its primary structure. Keratin filaments are assembled from type I/II heterodimers. These filaments lack polarity and they exhibit low resistance to deformation at low strains. At larger strains they are able to sustain large deformation without breaking by increasing stiffness (Wagner et al. 2007) in order to maintain the integrity of the cell.

MTs are relatively long filaments arranged in hollow cylindrical geometry with an outer diameter of 25 nm (figure 1.7d1). They possess a high persistence length indicating that they are rigid rods over cellular dimensions, and therefore, suitable to withstand compression stress. They serve as tracks for intracellular motor proteins and to move chromosomes and mitotic spindles to opposite sites of the cell during mitosis (Alberts et al. 2005). In addition, they form the core of cilia and flagella, which function to generate force and movement in certain cell types.

Tensegrity (from tension integrity) is a structural model to describe the mechanical properties of adherent cells (Ingber et al. 1981). It suggests that the mechanical response is controlled by changing the level of prestress existing in the cytoskeleton (Stamenovic and Ingber 2002). The cellular prestress is maintained by forces from contractile actin filaments. These forces are transferred over to intermediate filaments and resisted by the focal adhesions between adjacent cells and between the cell and the extracellular matrix. Changes in the level of prestress, thus the force balance, may alter the cells' stiffness by structural rearrangements within the cytoskeleton.

1.6 Elastic and viscoelastic response

The mechanical properties of materials can be characterized according to their response to an external force represented by loading and unloading curves (Butt et al. 2005). Figure 1.8 displays a typical stress (σ) versus strain (ε) curve. Stress versus strain can be regarded as force versus displacement. Normal stress (σ) is the force applied perpendicular to the surface (F/A) and its unit is (N/m^2) which is equivalent to pressure (Pa) and energy density (J/m^3). A normal strain (ε) is the change in length relative to the initial length ($\Delta L/L_0$) and it is dimensionless. This curve is divided into two main parts: (1) A linear elastic regime at low strains (a-b in the graph). (2) Plastic response at

higher stress and strain values (b-d). The yield point (b) indicates he transition from elastic to plastic deformation and point d indicates the maximal strain in which a rupture occurs. The slope of stress/strain in the linear regime (a-b) is calculated to assess the material's elasticity represented by the Young's modulus, an intrinsic property of the material: $E = \frac{\sigma}{\varepsilon}$.

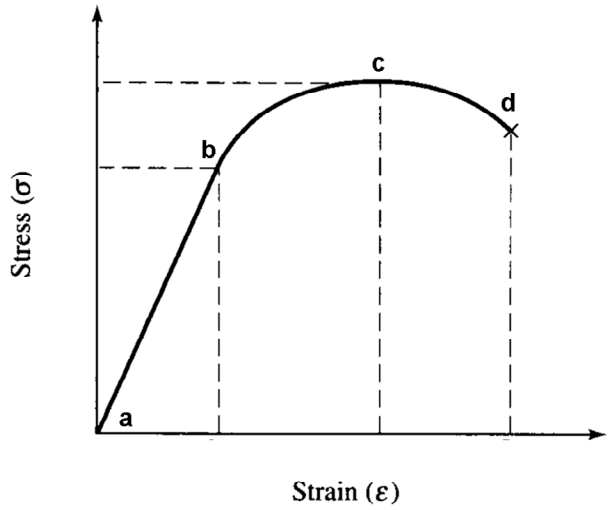

Figure 1.8: Stress/strain curve. A linear elastic deformation is shown at small stress values (a-b), whereas a plastic region (c-d) corresponds to higher stress values.

If the stress (deformation force) and the strain (the amount of deformation) are linearly related, the deformation is considered elastic, indicated by a complete shape recovery upon unloading (relaxation). Plastic response is typical to materials which show almost no recovery during unloading Most polymers and biomaterials including cells and biological tissues are categorized as viscoelastic (figure 1.9), exhibiting both solid and fluid-like characteristics (Ferry 1980, Marcus and Hochmuth 2002). The ratio of the applied stress to the rate of strain of a liquid defines the viscosity (Herrmann and Harris 1998): $\sigma = \eta \frac{d\varepsilon}{dt}$ .Viscoelastic materials slowly retain their original shape after removing the loading force, whereas a plastic material will not return to its original shape. In elastic response, the loading and the unloading curves overlap, whereas a viscoelastic response is characterized by a gap between the loading and the unloading curves due to the dissipated energy (Butt et al. 2005). Viscoelastic materials are significantly influenced by the rate of stressing or straining, so called: "time dependent materials" (Findley et al. 1989). A complete shape recovery is limited by the viscosity of the material. The area enclosed by the loading and unloading curves represents the dissipated energy termed hysteresis (Boschung et al. 1994). The area under the loading curve is the work done on the sample and it represents the total energy provided to the sample. This energy (E_{total}) is transferred to the elastic strains (E_{el}), whereas part of it is released as heat by plastic flow ($E_{dissipated}$):

$E_{tot} = E_{diss} + E_{el}$.

The overall dissipated energy (E_{diss}) is composed of plastic (E_{pl}), electrostatic (E_{elec}), friction-drag (E_d) and adhesion (E_{adh}) energy: $E_{diss} = E_{pl} + E_{elec} + E_{adh} + E_d$.

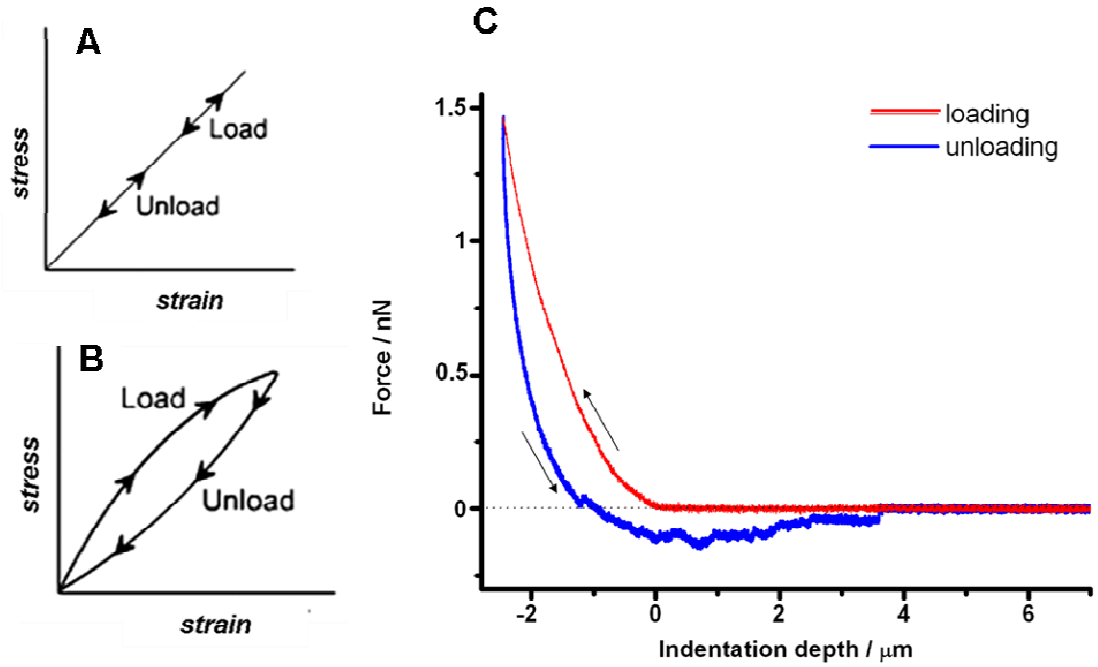

Figure 1.9: A: Elastic response demonstrating a complete overlap between loading and unloading curves. B: Viscoelastic response with a typical bellied-shape unloading curve. C: Force indentation curve recorded from the nuclear region of a living MDCK II cell exhibiting a viscoelastic response.

To explain the viscoelastic response, it is helpful to use mechanical models consisting of elastic springs and dashpots (Zhang 2005). Viscoelasticity of cells can be represented by a Kelvin-Voigt model, which is a two-element mechanical model (figure 1.1.0A) composing of a spring connected in parallel to a dashpot (Xu and Shao 2008, Evans et al 2005, Hochmuth et al. 1979). A spring represents the restoring elastic force upon unloading, which is proportional to the spring constant (k) according to Hook's law. A dashpot, consisting of a cylinder with a piston immersed in viscous liquid, represents a fluid-like behavior.

The viscous response is time and temperature dependent and the applied force is proportional to the speed. The equilibrium of forces between the external force (applied load) and the deformation of the sample represented by the elastic force and the damping (viscosity) is as follows (Kuchařová et al. 2007): $F_{ext} = F_k + F_\mu = k\Delta L + \mu \frac{dL}{dt}$

To estimate the degree of viscoelasticity, a relaxation time for shape recovery was defined (Hochmuth et al. 1979). It is the ratio between the viscosity constant and the elasticity constant:

$t_c = \frac{\eta}{\mu}$.

The relaxation time of cell deformation is relative short, 1-0.1 s, compared to that of polymers (Zhang and Zhang 2007). This means that if the indentation time of cells is in the same order as the time constant (t_c), the viscous effect, thus the hysteresis effect, is significant. To minimize this effect, indentation time must be increased.

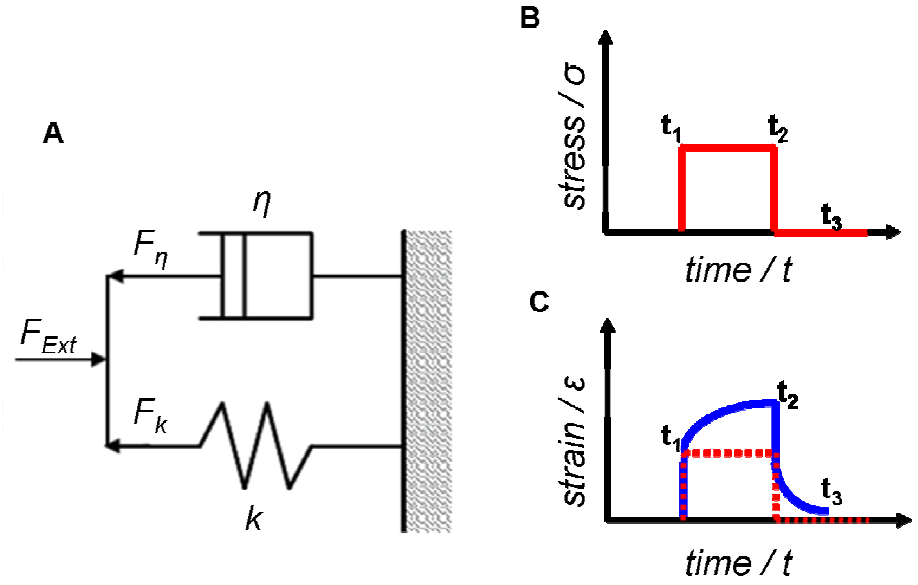

Figure 1.1.0: A: Illustration of the Kelvin-Voigt two-element mechanical model (Kuchařová et al. 2007). B-C: Viscoelastic creep and relaxation test.

A typical viscoelastic creep is illustrated in figure 1.1.0B-C. Creep is defined as slow continuous deformation of a material under constant stress (Findley et al. 1989). The sample is exposed to constant stress (B: t_1-t_2) and the resulted strain (C: t_1-t_3) is recorded as a function of time. The sample's initial response to the constant stress indicates an elastic behavior (red dotted line) followed by a flowing behavior (blue line) due to the viscosity. As the load is removed, an elastic shape recovery is followed by a gradual response over time.

1.7 Elastic properties of cell membranes

Cell membranes have relative large stretching modulus (K_s): 50 k_BT/ nm^2, and quite small bending rigidity (κ_b): 5-10 k_BT (10^{-19} J). Bending resistance is defined as the resistance to produce curvature in the surface (Evans 1974). k_BT represents an energy value as k_B is Boltzman constant (J/T) and T is the temperature in Kelvin (K). On the one hand, cell membranes have a small resistance to indentation and therefore they are easily deformed. On the other hand, membrane stretching is limited to 5 % extension in order to avoid membrane ruptures. Bending of a symmetric lipid bilayer from a planar (zero curvature) to a curved shape leads to the compression of the upper leaflet and to the stretching of the bottom leaflet. Compression is opposed by steric interactions of the lipid molecules whereas stretching is opposed by the water plus lipid surface tension.

Figure 1.1.1 illustrates the lipid monolayer structure at three different states: A is the planar form without curvature, B is the compressed state with a positive curvature, and C is the stretched or extended state with a negative curvature.

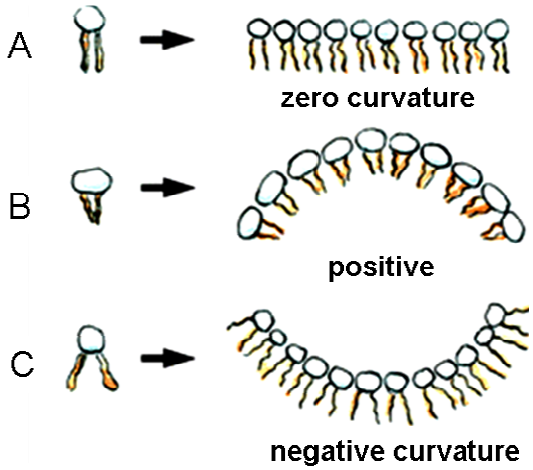

Figure 1.1.1: Membrane deformation results either in positive (A) or negative (B) curvature of the lipid bilayer (A). (Parthasarathy and Groves 2007).

Cell membrane deformation is a dynamic process which is governed by the interactions of lipids with proteins (McMahon and Gallop 2005). It enables the cell to carry out various biological processes, such as movement, division, extension and vesicle trafficking. There are five main mechanisms to explain cell membrane bending:

(1) Lipid composition. The chemical properties of lipids determine their molecular shape (cylinder, cone, or inverted cone) (Boal 2002). Therefore, the spatial distribution of lipids in the membrane leaflets give rise to the formation of negative or positive curvatures depending on the molecular geometry of the lipids. For example, PE is a cone shaped lipid inducing a negative curvature. In addition, enzymes can modify the size of the lipid head group thus changing the lipid molecular shape (Hammond et al. 1984). Flippases, which mobilize lipids from one membrane leaflet to another, can change the distribution of lipids in the membrane (Farge et al. 1999) thus influencing the curvature of the membrane.

(2): Integral transmembrane proteins with an intrinsic conical shape. For instance the receptor for acetylcholine (Unwin 2005), contributing to the formation of curvature as the membrane lipids mould around its shape.

(3): Assembly and disassembly of the cytoskeleton underlying the membrane lead to the formation of membrane curvature by effecting the membrane tension (Raucher and Sheetz 2000). For example, local actin polymerization results in the formation of endocytic invaginations (Marrifield et al. 2005).

(4): Peripheral proteins that embrace the lipids as a scaffold cause to membrane deformation. For example, the protein dynamin binds to inositol leading to the formation of a tubular shape deformation (Hinshaw and Schmidt 1995).

(5): Interaction of amphipathic helices with a lipid bilayer results in a positive membrane curvature. Amphipathic helices are stretches of α-helix containing both polar and hydrophobic parts. The interaction of the non polar domain with the lipid hydrophobic chains causes spatial rearrangements and the formation of membrane curvature (Ford et al. 2002).

2. THE OBJECTIVES OF THIS THESIS

The objectives of this thesis are as follows:

1) Investigating the effect of the porous substrate geometry on the cells' morphology and elasticity.

2) Shedding light on the topographical organization (length, density and diameter) of MDCK II apical membrane microvilli.

3) Optimizing a protocol for immobilizing native apical cell membranes on porous chips.

4) Mapping and modeling the elastic response of free standing apical membranes at physiological conditions and following chemical treatments.

3. INSTRUMENTATIONS AND METHODS

3.1 Atomic Force Microscopy

Atomic force microscopy (AFM) belongs to the SXM family, where S stands for scanning, X for the physical principle behind a particular instrument and M for microscopy. The principle of operation is shown in figure 2.0. It is based on an ultra sharp tip (20 nm tip radius) supported on a 300 µm long cantilever acting as a spring. The tip serves as a force sensor as it interacts locally with the sample surface. The cantilever is connected to a piezo scanner together with a laser detection system to record the cantilever deflection. Due to a feedback mechanism that can provide a controlled relative movement between the sample and the tip, a three-dimensional image of the surface is obtained (Binnig et al. 1986).

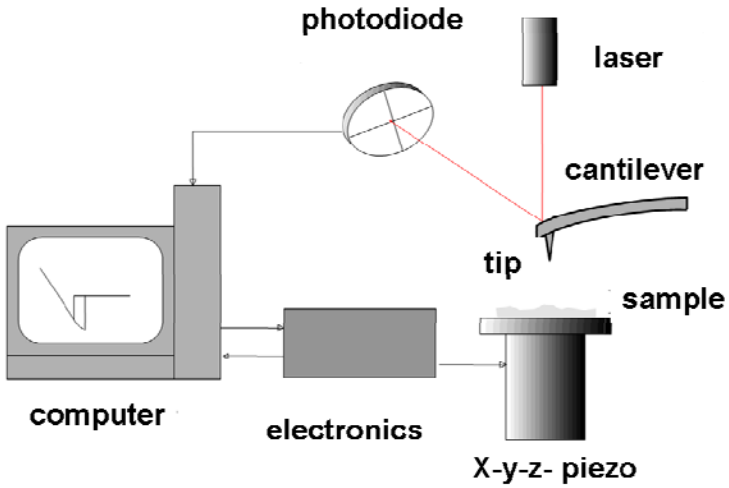

Figure 2.0: AFM principle of operation. (From "Rastersondenmikroskopie Skript", AG Janshoff).

Surface imaging microscopes include: electron tunnelling (scanning tunneling microscopy: STM), surface repulsive forces (AFM), photon tunnelling with a fiber optic tip (scanning near field optical microscopy), magnetic interaction with a magnetized probe (scanning magnetic microscopy) and ionic conduction with a glass pipette. The AFM has become the method of choice in the fields of structural biology and cell mechanics owing to two main reasons: (1) living cells and biomolecules can be scanned under physiological conditions without sample modification. (2) Mechanical properties and force interactions at nanoscale resolution can be investigated by means of force spectroscopy (Müller et al. 2009).

3.1.1 Imaging modes

Figure 2.1 displays a force versus tip sample separation curve indicating the distance regimes between the tip and the sample used for contact mode, intermittent mode (tapping mode), and non-contact mode measurements. In the contact mode, carried out at the repulsive force regime, the tip adheres to the surface with a defined force and the surface is scanned with the movement of the piezo scanner in the x,y,z directions. Contact mode measurements are carried out at the repulsive force regime (from the red point upwards on the force curve).

In the intermittent contact mode, the cantilever is oscillated at its resonant frequency over the surface. The cantilever taps the surface at the minimum points of the oscillation. The amplitude is used as a setpoint and the height of the cantilever over the surface is adjusted through a feedback loop by the piezo scanner. As the cantilever taps the surface, a phase shift occurs while the amplitude remains the same. This phase shift is used to create a phase image which gives information about the chemical properties of the surface. In the attractive mode, the tip is suspended about 40-50 Å above the sample surface as long as attractive van der Waals forces cause the tip to come into contact with the surface.

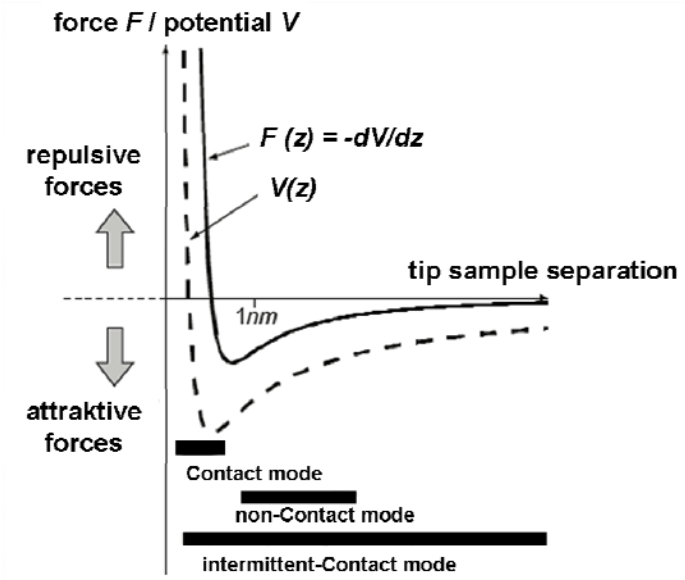

Figure 2.1.: Force/ tip sample separation curve indicating the AFM imaging modes in relation to the tip sample separation. (From "Rastersondenmikroskopie Skript", AG Janshoff). Contact mode measurement is carried out in the repulsive force regime.

Contact mode:

In contact mode two types of imaging are possible: one with a constant deflection of the cantilever while recording the vertical position of the piezo (constant force mode), and a second mode with a constant vertical position of the piezo while recording the deflection of the cantilever (constant height mode). The constant force mode is the one used to measure corrugated surfaces exhibiting height alterations. In liquid, biological samples are characterized by the presence of surface forces, such as van der Waals and adhesion forces. As soon as the van der Waals attractive forces exceed the spring constant of the cantilever, the tip "jump" into contact with the sample (Butt et al. 2005). The presence of adhesion forces draw the tip even deeper to the surface' leading to sample deformation (Pethica et al. 1988). As the tip senses changes in the sample height, the cantilever bends and the shifting position of the laser beam on the Position-Sensitive-Detector (PSD) is recorded. This signal is amplified up to 1000 fold (Marti et al. 1988) allowing the detection of small deflection (< 1 nm) with high sensitivity. In order to maintain a constant force between the tip and the sample, a z feedback loop is employed (Osten 2006). The difference between the setpoint, used as a reference, and the

recorded input signal reflects the deviation from the constant force and the goal of the feedback loop is to zero this difference. The output of the loop is z voltage applied to the piezo in order to adjust its position relative to the sample in z direction to keep a constant force. The feedback loop (figure 2.2) is regulated by proportional-integral-differential (PID) gain controls. P gain amplifies the error between the setpoint and the input signal in order to establish the size of the required correction signal. It defines a proportional band which is proportional to the magnitude of the response to the error signal. The resulting output signal (Y) can be written as follows: $Y = K_p(W - X)$. In this equation, K_p is the proportional gain constant, W is the setpoint and X is the error signal. This response results in an offset which can be corrected by the integral gain that integrates the deviation from the setpoint over a small period of time. The resultant integral gain output can be written as follows: $Y = K_I \int (W - X) dt$. In this equation K_I is the integral gain constant. High gain feedback significantly improves the sample's tracking performance compared with low gain feedback. In order to adjust the gains to optimal values, a line by line trace/retrace oscilloscope was used during scanning. When the gains are too low, no overlap between the trace and retrace lines is reported as the tip loses its contact with the sample. When the gains are too high, an overshot is recorded which can also be heard as noise.

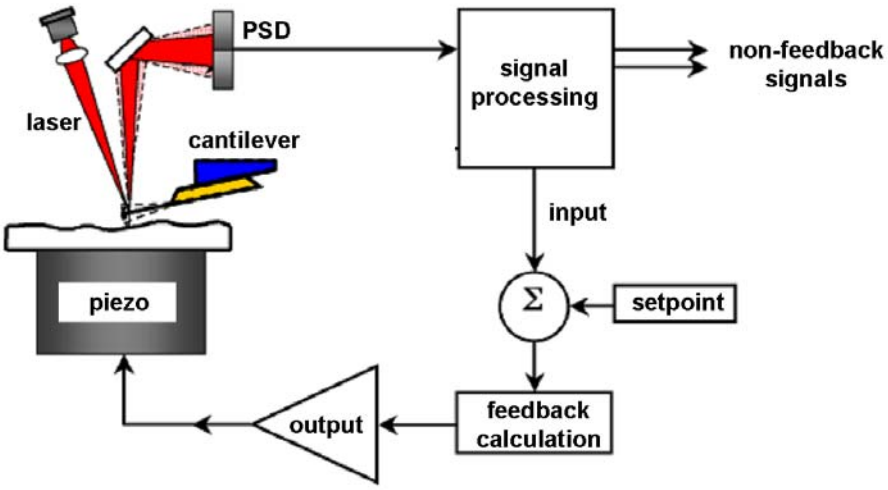

Figure 2.2: Schematic of a feedback loop control (www.asylum.com). The input signal represents the error signal and the setpoint is the reference signal. The output of the loop is the voltage signal channeled to the z piezo. It is constantly adjusted according to the input signal in order to zero the deviation from the setpoint.

The height image is generated by assembling successive line scans that requires a certain amount of time depending on the number of pixels. In constant force mode, each line scan represents a plot of the sample height measured by the voltage applied to the vertical piezo to keep the tip in contact with the sample at the preset constant deflection or force. The error signal image (deflection image) and the lateral image are generated from the non-feedback signals.

3.1.2 Force spectroscopy

Measuring forces on the molecular level is the second application possible with the AFM. It enables to apply well-defined small forces on a sample with spatial resolution and it can be used as a nanoindenter on soft samples to measure elastic properties. Force curves are measured by monitoring the force (or deflection) as the cantilever tip is approached and withdrawn from the surface by the vertical movement of the piezo. An AFM force curve, measured in liquid, can be divided into three parts: (1) the tip and the sample are far separated from each other and there is no force interaction. This noncontact line is straight with the exception of optical effects that can produce sinusoidal oscillation. (2) As the tip approaches the sample, long range electrostatic forces take place between the tip and the sample. A point of instability exists just before the tip touches the sample. In this point the tip jumps to the surface to establish contact ("snap on") due to the attractive van der Waals forces, which are weak intermolecular interactions. They originate from the interaction energy between permanent and instant electric dipole and decrease with distance as $1/r^6$. (3) The tip is in stable contact with the sample where hard repulsive Pauli forces exist.

For rigid samples (surface stiffness S >> spring constant K) the sample is not deformed and both tip and piezo movements are linearly coupled in a contact line which represents zero separation between them (Weisenhorn et al. 1993). The amount of deflection in the touching regime is equal to the amount of the Z piezo movement. Therefore, this regime of the curve is used for force calibration to covert the volt signal to deflection (nm) ("sensitivity slope"/ Invols). In this case, a plot of the force against the tip-sample separation would have a slope of 1. In order to convert the deflection signal to force (nN), the Invols value is multiplied by the cantilever spring constant according to Hook's law. For soft samples (surface stiffness S << spring constant) such as cells, the sample is deformed or indented. Figure 2.2 shows a typical force indentation curve reported from the nuclear region of a fixated MDCK II cell.

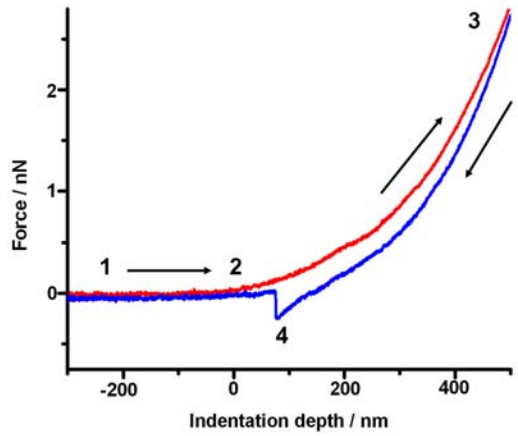

Figure 2.2.: Force indentation curve recorded from a fixated MDCK II cell in hypotonic solution. The y axis is the force and the x axis is the indentation depth. Approaching curve is shown in red and retracting curve is shown in blue.

The flat line represents the baseline where the cantilever is far away from the sample and no force is recorded (1). Point 2 represents contact point of the cantilever with the sample termed "snap on". From point 2 to point 3 the cantilever indents the sample at the repulsive force regime. The z piezo movement is larger than the cantilever deflection. Point 3 represents the maximal force used to indent the cell. Point 4 indicates the adhesion formed as the tip is pulled away from the cell surface, "snap off".

3.1.3 Cantilevers and force calibration

Since the cantilever is the sensor element of the AFM, its physical properties influences the measurement's performance. Commercially available cantilevers are made of silicon or silicon nitride covered with a native oxide layer of 1-2 nm thickness. The top side of the cantilever is coated with a layer of gold to increase its reflectivity. The cantilever is fabricated on chips of a few mm size. The tip is a few microns long and it is positioned at the end of the cantilever as the apex of the tip determines the imaging quality. The cantilever as a planar spring has two important physical properties: a spring constant ranging from (0.005 – 50) Nm^{-1} and a resonant frequency. The mass (m) of the cantilever and its spring constant (k) influence the resonance frequency (f) as follows:

$$f = \frac{1}{2\pi}\sqrt{\frac{k}{m}}$$

The smaller the mass m, the higher is the resonance frequency f and the bigger is the spring constant k. For accurate measurements of imaging and spectroscopy, it is necessary to calculate the spring constant (k) and to know the tip sharpness (its radius). For small deflections, the cantilever is approximated as a simple harmonic oscillator. If the tip is far from the sample, its motion is due to the thermal noise fluctuations. The Hamiltonian equation describes such a system as follows (Hutter and Bechhoefer 1993):

$$H = \frac{P^2}{2m} + \frac{m\omega^2 q^2}{2}.$$

P is the momentum, q is the oscillator displacement, m is the mass and ω is the resonant angular frequency of the system. According to the equipartition theorem, the average value of each quadratic term is equal to the Boltzmann constant and the temperature as follows:

$\frac{m\omega^2 q^2}{2} = \frac{k_B T}{2}$. As: $\omega^2 = k/m$, the thermal oscillation equation can be rewritten as follows:

$$k = \frac{k_B T}{q^2}.$$

The power spectral density of the fluctuations has a Lorentzian shape curve and the spring constant is calculated by a Lorentzian fit of the resonance peak.

Figure 2.3 shows thermal noise spectra of a contact mode cantilever TR800 from Olympus in PBS. In liquid, the resonance peak is typically lower than that recorded in air due to hydrodynamic damping.

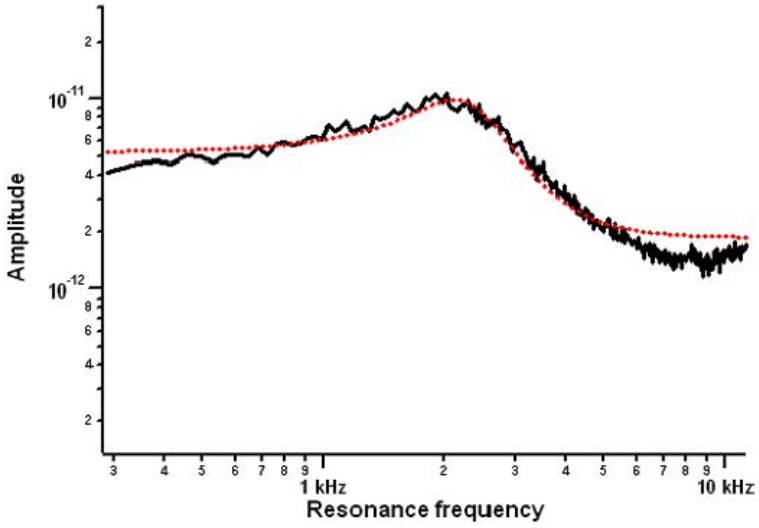

Figure 2.3.: Cantilever thermal noise measurement to determine the spring constant. The x axis is the frequency (kHz) and the y axis is the power spectral density of displacement fluctuations ($Å^2$). The red line is the Lorentzian fit. A spring constant of 0.02 N/m was recorded.

Three types of contact mode cantilevers were used for AFM measurements:

(1) MSCT AU with silicon nitride tips from Veeco Instruments (Mannheim, Germany). Figure 2.4 shows the V-shaped C lever cantilever, characterized by a nominal spring constant of 0.01 N/m, a length of 320 µm and a tip radius of 20 nm.

(2) Soft type OMCL-TR400PB cantilever from Olympus (Germany). The chip is fabricated with two V-shaped cantilevers of 0.1 and 0.02 N/m. Both are gold coated with a tip radius of 40 nm.

(3) CSC37 contact mode cantilever from *µmasch* (Spain) with rectangular geometry and a spring constant of 0.3 N/m.

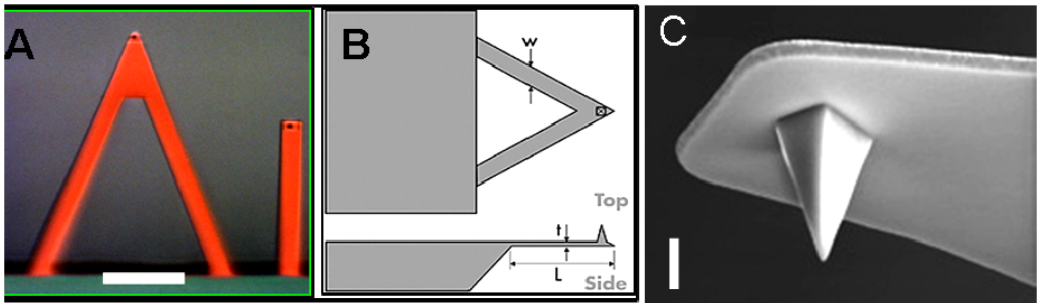

Figure 2.4.: MSCT cantilever (Veeco). A: Light microscope image of the pyramid shaped C lever (0.01 N/m nominal spring constant) used both for imaging and force spectroscopy. Scale bar is 100 µm. B: Schematic showing both top and side view. C: SEM image of the cantilever tip supplied by the manufacturer Veeco. The scale bar is 1 µm and the tip height is 3 µm.

3.1.4 AFM resolution

The possibility to obtain high spatial resolution with AFM measurements depends more on the properties of the sample than on the device itself (Weisenhorn et al. 1993). Deformation of soft samples is a major limitation for high resolution: when the tip comes into contact with a soft sample,

it compresses into the surface until the contact area becomes large enough to balance the applied force. If the tip is modeled as a stiff sphere of radius *R* with a very large Young's modulus (*E*) and the scanned sample is modeled as a soft surface with a much smaller *E* modulus, the radius of contact *a* (nm) can be expressed as follows (Shao et al.1996):

$a = \frac{3}{4}\left[\frac{FR\left(1-\nu^2\right)}{E}\right]^{1/3}$. *F* is the applied force and ν is the Poisson's ratio.

In case that ν = 0.33 this equation can be rewritten as:

$a = 15.5\left(\frac{FR}{E}\right)^{1/3}$.

To obtain smaller contact area thus better resolution, the rigidity of the sample (Young's modulus) must be as high as possible and the applied imaging force must be as small as possible. The sharper the tip (smaller radius), the smaller is the contact area and the higher is the resolution. Since the apex of most tips is rather blunt with a large radius of curvature, it is also assumed that small protrusions on its blunt surface are responsible for the obtained high resolution. The applied force must be as small as possible. However, in order to maintain a stable imaging, the applied force must be at least several times larger than the thermal noise of the cantilever. Otherwise, the tip will disengage spontaneously from the surface.

Another approach, relating the image resolution *d* to the geometrical characteristics of the tip radius and the sample, is as follows (Bustamante and Keller 1995):

$d = \sqrt{2R}\left(\sqrt{\Delta z} + \sqrt{\Delta z + \Delta h}\right)$.

d is the minimum separation at which two point objects are resolved. In this model, the topographical image of a point object is broadened or narrowed by the size of the tip. The tip has a parabolic shape with a radius *R*.. Two point objects are broadened by the tip and they appear as inverted parabolas. Δz is defined as the minimal depression between two parabolas and Δh is the height difference between the two objects. The limitations of this model are that it does not take into account compression and deformation characterizing the indentation of soft sample. In addition, it cannot explain a few nanometer resolution images of biological samples (Müller et al. 1998) obtained in contact mode with commercial tips (5-30 nm tip radius). It was suggested that only a very small tip asperity interacts with the sample, whereas the larger part of the tip apex balances the tip-sample interactions by electrostatic forces (Müller et al. 1999). A spatial resolution of 1 nm was reported for extracted and immobilized biomembrane patches (Müller and Engel 2007), 50 nm for animal cells (Grimellec et al. 1998) and 10 nm for microbial cells (Dufrêne et al. 2008).

To summarize, the resolution of soft samples can be improved as follows: (1) increasing the Young's modulus of the sample by chemical fixation (Butt et al. 1990). (2) Reducing the total adhesive forces of the sample's surface, such as van der Waals forces, by using sharp tips and solutions (Hartmann 1991) containing ions (buffers). (3) Minimizing the applied force during imaging.

3.1.5 Molecular Force Probe (MFP-3D) design

In this study, the MFP-3D from Asylum Research (Santa Barbara, U.S.A) was used both for imaging and force spectroscopy. Figures 2.5 shows the instrument set up and a cross section of the AFM head. For detection, a beam from a laser diode is focused onto the end of the cantilever. As the cantilever bends the position of the reflected beam is monitored by the photodiode. Since the system is rigidly built, no vibration isolation is necessary to obtain an image and even when the entire system has a relatively large movement, the relative movement between the tip and the sample is small.

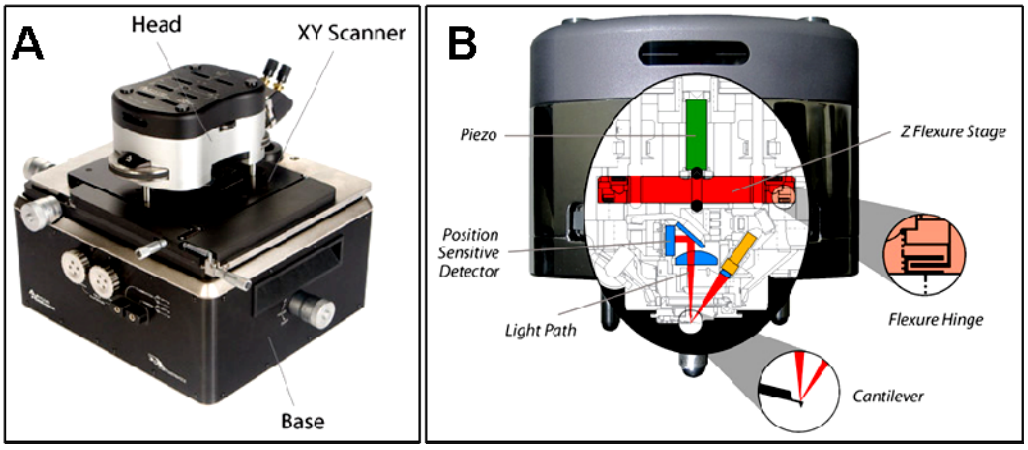

Figure 2.5.: MFP- 3D set up from Asylum Research is composed of an AFM head, a scanner, capable of nm length cantilever positioning in x,y,z directions, and a base. B: AFM head cross section illustrating the piezo location in relation to the laser beam path. The laser beam is focused on the cantilever and then it reflects to a mirror directing the beam to the photodiode. (www.asylumresearch.com)

3.1.6 Biological applications of AFM

The AFM is ideally suitable for the investigation of biological surfaces (Poole et al. 2004, Grimellec et al. 1998, Braet et al. 1998) owing to two main reasons: (1) the measurement requires minimal preparation of the tested sample in comparison to other imaging techniques, such as SEM. In addition, mild sample's pretreatments minimize possible artifacts. (2) The measurement can be performed under physiological conditions. The most critical step in the preparation is the immobilization of the sample onto a rigid supporting substrate. This step is necessary to avoid vibration during imaging and to resist the removal of the specimen by the cantilever tip (Yang et al. 1993). Immobilizing is possible by using adhesive compounds and biomolecules. Non-specific surface coatings include Poly-D-lysine (Butt et al. 1990), so called "molecular glue", whereas a specific coating refers to antibodies (Morris et al. 1999). Imaging of individual cells poses several difficulties, such as cell displacing and artifacts due to the height difference between the cell edge and the substrate. Cell immobilizing techniques include a scanned pipette to hold the cell against the cantilever tip (Ohnesorge et al. 1997), cell entrapment in porous media or in gel medium such as agar (Morris et al. 1999). Overall, the AFM has been used to image various biological samples, ranging from biopolymers such as DNA, proteins, to whole cells. In addition, it allows the investigation of dynamic cellular processes, such as mesenchymal stem cells growing on micropatterned silicon

(Zahor et al. 2007). The AFM is capable of detecting a wide range of forces (5 pN-100 pN) which is relevant to that involved in cellular processes (Müller et al. 2009). In addition, it allows the quantification of the cells' elasticity represented by the Young's modulus *E* (Rotsch and Radmacher 2000, Mathuret al. 2001, Steltenkamp et al. 2006). The relation between the sample's stiffness, k_s, and the Young's modulus, *E*, is (Butt et al. 2005): $k_s = \frac{3}{2} a E_{tot}$, whereas $\frac{1}{E_{tot}} = \frac{3}{4}\left(\frac{1-\nu_s^2}{E_s} + \frac{1-\nu_t^2}{E_t} \right)$. The stiffness and theYoung's modulus of the sample and the tip are designated: k_s, E_s, k_t, E_t, respectively. The tip-sample contact radius and the Young's modulus of the sample plus the tip is E_{tot}. Since the stiffness of the cell is much smaller than that of the tip ($k_s << k_t$), the relation between the sample's stiffness and the Young's modulus is: $k_s = 2a\left(\frac{E_s}{1-\nu_s^2} \right)$.

The analysis of force indentation curves recorded from cells is based on the Herz model (Herz 1881), describing the elastic deformation of two elastic, homogenous, and nonadhesive spherical surfaces touching each other under load. A general equation (Pelling et al. 2007) to relate the applied force *F* to the indentation, δ, is: $F = A\delta^n$. *A* is a constant including both the elastic constant *K* and the tip geometry: $K = \frac{E}{\left(1-\nu^2\right)}$ (Mahaffy et al. 2004).

The force indentation equation can be applied with different tip geometry, such as: sphere (parabolic), cone, and a flat end cylinder (A-Hassan et al. 1998). For a cone shaped tip, *n* is equal to 2, which means that a log-log plot of force versus indentation will give a slope of 2.

The following non linear relation between indentation depth *h* and force *F* was used to extract the Young's modulus of the cells (Sneddon 1965): $F\left(h\right) = \frac{2E}{\pi\left(1-\nu^2\right)\tan\alpha} h^2$. In this equation, α is the half opening angle of the cantilever (35^0) and ν is the Poisson ratio which is defined as the ratio between the radial strain and the vertical strain. This relation is true only to the case that the indentation depth, *h*, is much smaller than the sample thickness *h* ($d >>$h) in order to avoid the contribution of the underlying substrate (Domke and Radmacher 1998). Since the adhesion of the surface is neglected (Sneddon 1965, Herz 1881), it can be applied only when the adhesion force is much smaller than the maximum load (Butt et al. 2005). In general, the fitted part of the approaching curve must not exceed 10% of the maximal indentation depth (Butt et al. 2005) which corresponds to small forces. There are two limitations for this relation: firstly, the Poisson's ratio ν is assumed constant which is not the case for the inhomogeneous surfaces of cells (Butt et al. 2005, Steltenkamp et al. 2006). Secondly, it is impossible to determine the exact contact point of the cantilever with the cell. As the tip jumps into contact, the presence of adhesion and van der Waals forces lead to

indentation even before a tip-cell contact is established (Butt et al. 2005). The elasticity of cells can also be quantified by recording force indentation curves as the tip scans a defined area of the cell, so called force mapping (Radmacher 1994). The cell topography at different loading forces as well as the local Young's modulus can be calculated by analyzing the recoded force indentation curves (Rotsch and Radmacher 2000). This type of measurement is especially attractive for heterogeneous surfaces, such as those of cells. However, the limitation of this technique is the relative long acquisition time (about 1.5 h for 30 x 30 map grid) leading to thermal drift. Thermal drift refers to temperature fluctuations resulting in non linear response of the piezo. There are three main factors contributing to the cell stiffness E: (1) osmotic pressure. (2): The plasma membrane. (3): The inner organelles, such as the nucleus and the cytoskeleton. The Young's modulus varies among cells. Typical values of animal cells are as follow: MDCK II epithelial cells: 6 kPa (Steltenkamp et al. 2006), human fibroblasts: 5 kPa (Bushell et al. 1999), smooth muscle cells: 5-8 kPa (Engler et al. 2004), skeletal muscle cells: 25 kpa (Mathur et al. 2001), cardiac muscles: 100 kPa (Mathur et al. 2001).

3.1.7 Drag force

Hydrodynamic drag forces exist between the cantilever in motion and the aqueous solution and between the cantilever and the sample. Drag forces acting on the cantilever due to its moition in liquid (A-Hassan et al. 1998, Hoh and Engel 1993) are proportional to the cantilever velocity, the medium viscosity and the tip sample separation (Alcaraz et al. 2001, Zelenskaya et al. 2005). Taking into account the sample's length scale L (cell membrane) and the applied canilever velocity ($V_0 << 1$ cm/s), these forces operate at Newtonian fluid and Stoke's flow conditions with low Re values: ($Re = \rho V_0 L/\eta << 0$) (Morris et al. 1999, Fan and Fedorov 2003). As the cantilever approaches the sample, the hydrodynamic drag forces increase accordingly (Roters and Johannsmann 1996). The relation between the drag force acting on the cantilever, F_d, and the tip sample separation $h + d_{eff}$ can be modeled as follows (Alcaraz et al. 2001):

$$F_d = \frac{6\pi\eta a_{eff}^2}{h + d_{eff}} v_{tip}$$

In this relation, h is the distance between the cantilever and the sample, d_{eff} is the effective height of the tip, a_{eff} is the effective radius of the tip and v_{tip} is the cantilever velocity.

As the tip is in contact with the sample, friction forces between the tip and sample cause the cantilever to bend forward (Hoh and Engel 1993), indicated by an offset with the contact line of the force indentation curve (hysteresis). As the tip retracts, the cantilever bends upward indicated by an opposite offset of the line. These friction forces increase with the cantilever velocity indicated by the increasing hysteresis. Force indentation measurements recorded on

viscous surfaces (living MDCK II cells) at high cantilever velocity (>10 µm/s), lead to a distortion of the elastic response (Steltenkamp et al. 2006, Butt et al. 2005).

3.1.8 Imaging based on force distance curves

The pulsed force mode (PFM) is a non resonant intermediate contact mode measurement, which extends the imaging possibilities and reduces the shear forces between the cantilever and the sample. PFM is an "all in one" combination of topography, adhesion, stiffness, viscosity, energy dissipation, contact time and long range forces that can be analyzed and imaged simultaneously. In addition, it enables to record force curves with high speed. During the measurement a sinusoidal voltage is used to modulate the Z piezo with oscillation amplitudes of typically 20-500 nm at a frequency of 100 Hz-2 kHz. Figure 2.8 shows a typical PFM cycle. The oscillated cantilever is pushed to the repulsive regime and images are obtained by measuring different parts of the Pulse force curve (figure 2.9). The points shown in figure 2.8 indicated the contact area of the cantilever with the sample (from point A to point D). At the lowest point of the piezo oscillation the tip is out of contact with the sample. The highest point of oscillation represents the maximal force or cantilever deflection (figure 2.8B).

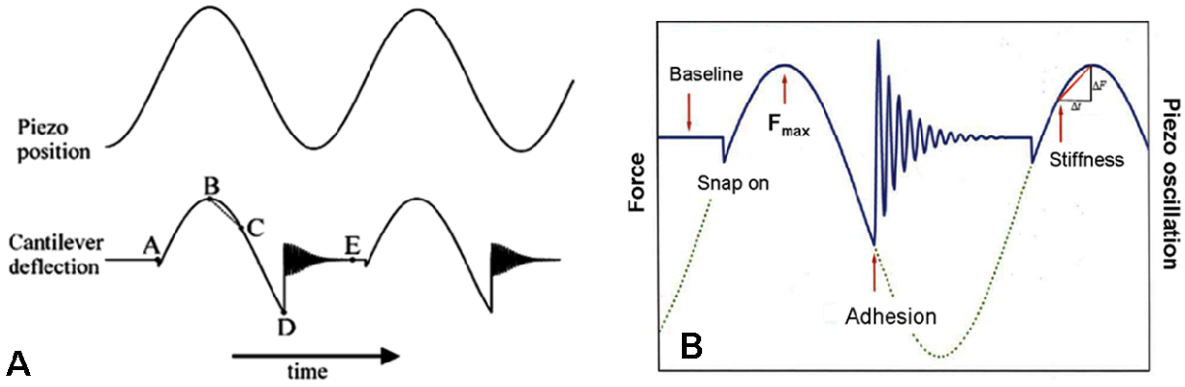

Figure 2.8.: A: The upper curve represents the piezo sinusoidal oscillation in z direction. The lower curve illustrates a typical PFM cycle, as the cantilever deflection (force) is plotted against the time. Point A is the contact point between the cantilever and the sample. The peak of the amplitude (Point B) represents the maximal deflection used for the feedback control. The slope between points A and B is proportional to the stiffness of the sample. Point D is the minimum value of the force curve and it is proportional to the adhesion force. Point E is the baseline: long range forces (Butt et al. 2005).B: Superposition of the cantilever deflection with the z piezo oscillation.

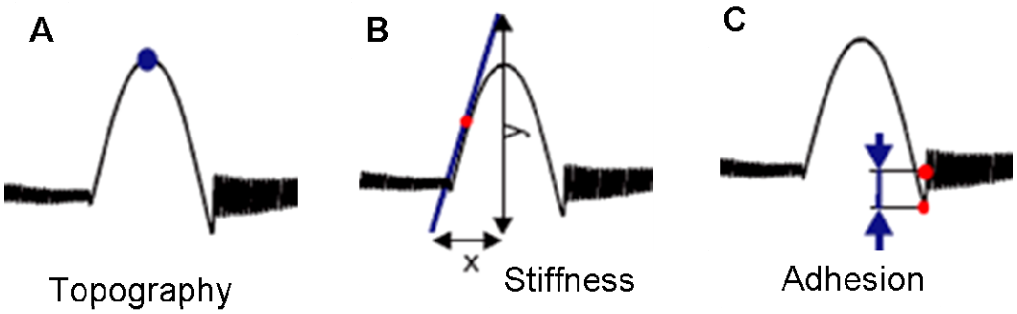

Figure 2.9.: Illustrations of different parts of the pulsed force curve used to obtain Images in PFM. A: maximal force (toography). B: linear slope (stiffness). C: snap off distance (adhesion).

3.2 Force indentation curve analysis

AFM images were analyzed with the program: Scanning Probe Image Processor (SPIP), Image Metrology, Lyngby, Denmark. Force indentation curves were analyzed by using the program IGOR (Wavemetrics, Lake Oswego, OR). According to Hooke's law, the loading force, *F*, is proportional to the deflection of thecantilever, *d*, and the spring constant of the cantilever, *k*: $F = -kd$.

Force indentation curves, taken on a rim covered with apical membranes, were used as a reference to determine the exact contact point between the cantilever and the membrane. For indentation curves taken in the middle a pore, the same z piezo movement causes a smaller deflection of the cantilever as a result of free indentation across the pore. In this case a force distance curve with a smaller slope is obtained.

3.3 Fluorescence and Epifluorescence microscopy

Fluorescence is a physical phenomenon referred to the absorption and emission of light by organic and inorganic molecules. It takes about 10 ns between light absorption and fluorescence emission, named also "cold light" as very little heat production is involved. Fluorochromes (Fluorophores) are specific dye molecules consisting of conjugated double bonds in their chemical structure with a high quantum yield. If fluorophores absorb light that is appropriate to their absorbance range, electrons are excited to a higher energetic level. Then, part of the energy is lost by vibration, rotation and transfer to other molecules. From this level the energy drops to a ground state and the rest of the energy is released as fluorescent light with lowered photon energy and lowered wavelength. Fluorescence activity can be schematically illustrated using a Jablonski energy diagram. Fluorophores can classified into three groups: (1): Fluorochromes that require binding molecules such as antibodies or lectins to label proteins, lipids or other functional groups on the membrane surface. For example *Phalloidin* conjugated to Alexa488 (2): Fluorochromes that bind directly to their target molecules and they do not necessarily require a transportation system. For example, DiI and DAPI (3) Fluorescent protein produced by organisms themselves such as the green fluorescent protein (GFP) or cell line genetically modified to express this type proteins. For example, MDCK II cells expressing the enhanced yellow fluorescent protein (eYFP).

Fading is a general term for reduction in fluorescence intensity with time and photobleaching refers to the irreversible decomposition of fluorescent molecules in the excited state due to interaction with molecular oxygen before light emission. Raising the fluorescence intensity can be achieved either by higher dye concentration to stain the sample or by increasing the intensity of the excitation light. However, increasing the dye concentration may be inefficient, since fluorophors close to the upper sample surface can absorb enough light to reduce the portion available to the rest of the sample. Increasing the lamp intensity leads to fluorophore saturation. A fluorescence microscope is based on the fluorescence phenomenon of fluorochromes and has become a powerfull instrument to investigate a biological specimen. It is composed of four main parts (figure 2.1.0): (1) light source to excite the fluorescence of a fluorochrome. (2) A set of filters which includes excitation filter letting only the

required range of wavelength to pass through, dichromatic mirror which reflects light below a given wavelength and permitting longer wavelengths to pass through, and emission filter restricting the emitted light color to the best fitting the fluorochrome. (3) An objective with a good light gathering capacity, a good light transmission for the wavelength used and low autofluorescence. (4) A camera required to transfer the optical image to a digitized one on a computer screen. Monochrome cameras are more preferable than a color one due to the additional beam splitting and wavelength selection components of colored cameras. A CCD camera offers high signal to noise ratio and the ability to quantify intensity and intensity distribution. An epifluorescence microscope is a type of fluorescence microscope, in which the objective used by the illuminating light is also used by the emitted fluorescent light in conjunction with a dichroic mirror. In a basic setup, light from a lamp source passes through a filter and then it is reflected from a dichroic mirror towards the sample. The emitted fluorescent light passes through the same dichroic mirror and a second filter to the eyepiece. Object-to-image transformation takes place simultaneously and parallel to all object points. To computerize the optical image, two steps are required: First the continuous-tone optical image is digitized by dividing it into small separate square shaped blocks, which are named pixels. In the second step, called pixel quantization, each pixel is assigned a discrete brightness value. To optimize the image acquisition, an intensity histogram was used which is capable of controlling the overall intensity, contrast, dynamic range and image saturation. As the pixel count (y axis) is plotted against the intensity level (x axis), the overall contrast is best obtained when the histogram covers the whole dynamic range without creating saturation at the right side of the histogram. The maximal lateral resolution with optical microscopes is about 200 nm as it is limited by light diffraction. This diffraction, named Airy disc, is created when a sample detail is illuminated within a microscope and it is defined as a distribution of a bright central spot with a primary maximum and minima separated by dark regions. Microscope resolution is defined as the smallest distance apart at which two points can be distinguished on the sample. The smaller the Airy disk, the higher is the resolution. However, higher resolution results in smaller depth of field. According to the Rayleigh criterion, the minimum separation between two Airy disks for which they can be seen separated defines the resolution.

The lateral resolution depends linearaly on the emitted wavelength (λ_{em}) and the numerical aperture ($NA = n \sin \mu$) of the objective: $R = \frac{\lambda_{em}}{2NA}$.

The NA depends on the type of objective used. n is the diffraction index of the medium between the front lens of the objective and the specimen and μ is equal to one half the angular aperture. The greater μ, the greater is the numerical aperture.

We acquired fluorescence images with an upright epifluorescence microscope BX 51 (from Olympus, Hamburg) equipped with A CCD monochrome camera and water immersion objectives (refractive index of water is 1.33): x40, NA = 0.8 and x100, NA = 1.0.

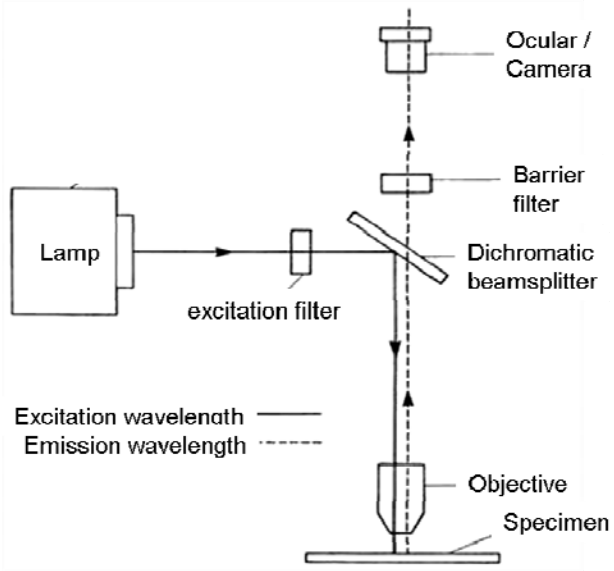

Figure 2.1.0: Schematic of epifluorescence microscope illustrating its main parts: lamp as a light source, a set of excitation and emission filters with a beam splitter (dichromatic mirror), Objective and an ocular.

3.4 Confocal Laser Scanning Microscopy (CLSM)

The CLSM uses a powerful laser beam to obtain sharp fluorescence images of biological samples with a high signal to noise ratio. The principle of operation is based on point by point scanning and point by point detection from the focus plane of the sample. To block out of the focus emitted light, it is designed with a small aperture, called pinhole, positioned in front of the photo multiplier (PMT) detector in a conjugated plane to the intermediate image plane (figure 2.1.1A). The diameter of the pinhole is variable and the light passing through form an Airy disc as a result of light diffraction. The central band of this diffraction is used to normalize the size of the pinhole to an Airy Unit value. The smaller the pinhole, the narrower is the peak of the light diffraction pattern and the better is the resolution. To quantify the fluorescence intensity distribution, a point spread function (PSF) is defined and it relates to the maximal width of the light diffraction at 50% drop of maximal intensity. In addition to sharp fluorescence images, it is possible to quantify molecular dynamics by bleaching a specific fluorescent area on the sample, and a three dimensional image can also be obtained by optical sectioning of the sample. The thickness of each slice (vertical resolution) depends on the NA of the objective enabling to achieve a slice thickness of a few hundreds nm.

3.5 Fluorescent markers

The fluorescent markers, used in this study to label cell membranes and cells, can be categorized into two groups: (1): Lipid labeling with DiI (2): Protein labeling with *Phalloidin* Alexa488/ *Phalloidin* Alexa546 (F-Actin staining) and MDCK apical membrane glycoprotein (gp135) labeling with monoclonal antibody (mAb) 3F2. To label whole cells, a fluorescent DNA probe, DAPI, was used.

DiI: A lipid analogue which belongs to the family of cyanine dyes that have been used to investigate the structure and dynamics of both cell membranes and artificial lipid bilayers. DiI is an amphiphilic, molecule, having a polar head group connected to two hydrophobic alkyl chains. This molecule is bilaterally symmetric with each half consisting of a positively charged conjugated ring and an attached long hydrocarbon chain. A bridge of three methane groups joins the two rings. The length of the hydrophobic hydrocarbon chains alters their partitioning into the bilayer and the dye is designated $DiIC_n$ (n = 12, 14, 16, 18 …). DiI-C_{18} diffuses into the cell membrane as the hydrocarbon chains are embedded in the lipid bilayer parallel to the phospholipid acyl chains with their conjugated bridge chromophore parallel to the surface of the cell. DiI absorbs maximally at 546 nm and its maximum emission is at 563 nm with a bright orange-red fluorescence. It has no detrimental effects when incubated with living cells. Besides visualizing the plasma membrane, DiI has been applied to measure lipid mobility in membranes and to assess cell fusion. To label MDCK II living cells, 2 µl volume of $DiIC_{18}$ (Sigma: 42364) dye solution (3 mg/ml stock solution in DMSO) was added directly to the cells in the cultivating dish (30 min incubation time at 37^{o}C). In general, chemical fixation of cells/membrane fragments before or after DiI staining resulted in artifacts. Both apical and basolateral membranes fragments were prepared from DiI labeled cells.

Phalloidin-Alexa488/Alexa546: To label F-Actin, Alexa488/Alexa546 flurophores conjugated to *phalloidin* (Initrogen: A12379) were used. *Phalloidin* is a toxin isolated from the deadly *Amanita phalloides* cap mushroom. It consists of a bicyclic heptapeptide with a thioether bridge between cysteine and tryptophan residues that form an inner ring structure. Fluorescent *phalloidin* has the same affinity for different actin filaments size and it bind in a stoichiometric ratio of about one *phalloidin* molecule per actin subunit in cells. This conjugate is small in size (12-15 Å in diameter) and with 2 kDa molecular weight. The dye is both photostable and independent of pH range from 4.0 to 10.0. In addition, labeling does not prevent actin binding proteins (ABP) from binding to F-Actin. Native membranes were stained with 3.3 µM Phalloidin-Alexa488 solution in PBS for 45 min. Cells were fixated before F-actin labeling in order to increase to increase the permeability of dye into the cells. The fixation protocol is detailed in 3.1.0.

3F2 mAb: A monoclonal antibody (mAb against) against a specific membrane glycoprotein (gp135) expressed on the apical membrane of MDCK II cells. gp135 is a transmembrane protein linked to the cytoskeleton (Ojakian and Schwimmer, 1988), which has been identified as a podocalyxin participating in the formation of a preapical domain during MDCK II cell polarization. This protein changes its localization on the membrane surface during cell polarization. In terminally polarized cells, the expression of gp135 is confined to a subdomain of the apical membrane. 3F2 mAb was a generous gift provided by Prof. G. Ojakian (State University of New York Downstate Medical Center, Brooklyn). For immunofluorescence labeling, samples were incubated with 3F2 mAb (undiluted supernatant from hybridoma cells) for 45 min at 4^{0}C, washed with PBS and then incubated with goat anti mouse Ab conjugated to FITC (Sigma: F-0257) for 30 min at 4^{0}C.

DAPI**:** 4', 6'-diamidino-2-phenylinodole (DAPI) is a DNA probe which can bind strongly to AT rich regions in the minor groove of the DNA. In addition, it can intercalate with GC and AT sequences. This fluorochrome belongs to the second group of fluorochromes as having an inherent binding capability. It absorbs maximally at 358 nm with light emission that appears blue/cyan at 461 nm.

3.6 Scanning Electron Microscopy (SEM)

SEM is a type of electron microscope characterized with a high spatial resolution (1 nm), a large depth of field and high magnification capabilities. The use of an electron beam instead of visible light in optical microscopes enables to achieve high resolution. Electrons as electromagnetic waves are characterized with a small wave length and high energy. According to the resolution criteria, the smaller the wavelength, the higher is the resolution. To obtain an image, a beam of electrons is first generated in an electron gun which operates as a cathode. This electron gun is made of tungsten filament and it is supplied with voltage. Electrons are then attracted through an anode and they are condensed by a condenser lens to a small point focused on the sample by an objective. Since electrons are negatively charges, they can be focused by electromagnetic lenses used in the electron microscope setup. Surface scanning is possible by scan coils which create a magnetic field deflecting the beam over the sample. The interactions of electrons with the sample increase by accelerating the electron beam. The higher the atomic number, the lower are the sample-electron interactions. Both a secondary electron beam and back scattered electrons collect the emitted electrons to generate a volt signal. This signal is then processed to produce a focused topographical image. In addition, the secondary electron beam allows the acquisition of a three dimensional image and the back scattered electron beam enables to obtain a sharper image giving information about the sample composition. The degree of the electron beam penetration into the sample is controlled by the applied voltage. To achieve a high resolution topography image, a small indentation of a few nm is applied. Both the generation and the maintenance of electron beam require vacuum conditions. In addition, organic materials, such as biological samples, must be chemically fixated, dried and coated with a thin layer of gold to become conductive. SEM measurements of both cells and membranes were carried out by Gunnar Glasser (Leo Gemini 1530, Zeiss Göttingen) in MPIP Mainz.

3.7: MDCK II cell culture

MDCK II cells were cultivated on plastic dishes or porous chips in MEM medium supplemented with 10% v/v FCS, 2 mM L-glutamin and100 µg/ml penicillin/ streptomycin. To detach confluent cells, 0.05 % trypsin-EDTA solution (10 min incubation time at 37^{o}C) was used followed by centrifugation and resuspension in fresh medium. Cells were seeded (10^6 cells /ml) on porous chips (1.2 µm and 2 µm pore size) positioned in a plastic dish and were cultivated in 6% humidified incubator at 37^{o}C. In these conditions, a preconfluent cell monolayer (incomplete coverage of the substrate with cells) was obtained following 24h. Complete cell coverage was reached after 48 h and highly confluent cells were obtained following 72h. Every two days the cells were fed with a fresh medium.

3.8: Si/SiO_2 porous substrate

Porous silicon chips were obtained from fluXXion B.V., Eindhoven, NL. We used 5x5 mm size chips with 1.2 and 2.0 µm pore size. The geometry of the chips (14 pore rows and 10 pore columns) was used to localize membrane fragments and cells for AFM imaging. As Si/SO_2 substrates exhibit autofluorescence, figure 2.1.8 shows CLSM images (A and B) and AFM height image of 1.2 µm diameter size porous Si/SiO_2 substrate.

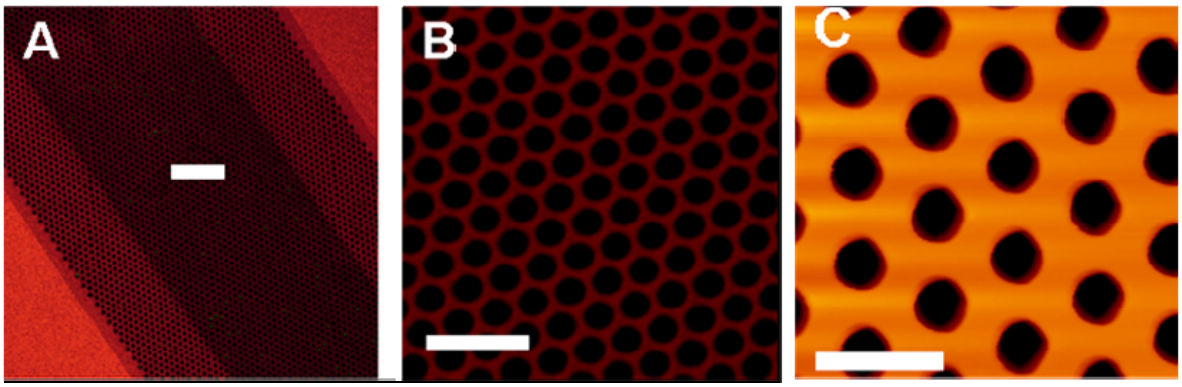

Figure 2.1.8.: A and B: CLSM images of autofluorescent Si/SiO_2 porous chip. A: Scale bar is 20 µm. B: Scale bar is 5 µm. C: AFM height image. Scale bar is 3 µm.

To reduce autofluorescence, 5 nm chromium and 60 nm gold were coated on the chip surface by thermal evaporation (Steltenkamp et al. 2006). Gold coated chips were stored and cleaned with ethanol. To remove organic material, the chips were cleaned in plasma cleaner by using Argon gas for 5 min. In this cleaning method, the chips are positioned in a reactor vessel which allows controlled insertion of Argon gas at a pressure of 1 Pa. Due to the applied electric field at a pressure of 1 Pa, ions and electrons are formed. These molecules react with the surface and diminish the organic material. To remove cellular material, used chips were incubated with Piranha solution (30% H_2O_2 + 30% H_2SO_4) for 30 min followed by rinsing with distilled water for 3 h.

3.9: Preparation of apical membrane sheets for AFM/fluorescence

The preparation protocol is as follows (figure 2.1.9 A): confluent MDCK II cells were washed with PBS and then were incubated with distilled water for 3 min (B). To enhance electrostatic adhesion between the substrate and the membranes, the chips were incubated with 1 mg/ml poly-D-lysine (Sigma: P6407, lyophilized, sterilized, MW = 70,000-150,000) solution for 10 min followed by thorough rinsing with ultrapure water. Then, the chips were gently pressed on the cells' apical surface for 20 min to form a conformal surface contact (C). By lifting the chips off the cells, were the apical membranes transferred to the poly-D-lysine coated chips with their cytoplasmic side facing up (D). To visualize both apical and basolateral membrane fragments, various fluorescence markers were used (E-N). Membrane samples were immediately stored in PBS at 4^0C or fixated for later use.

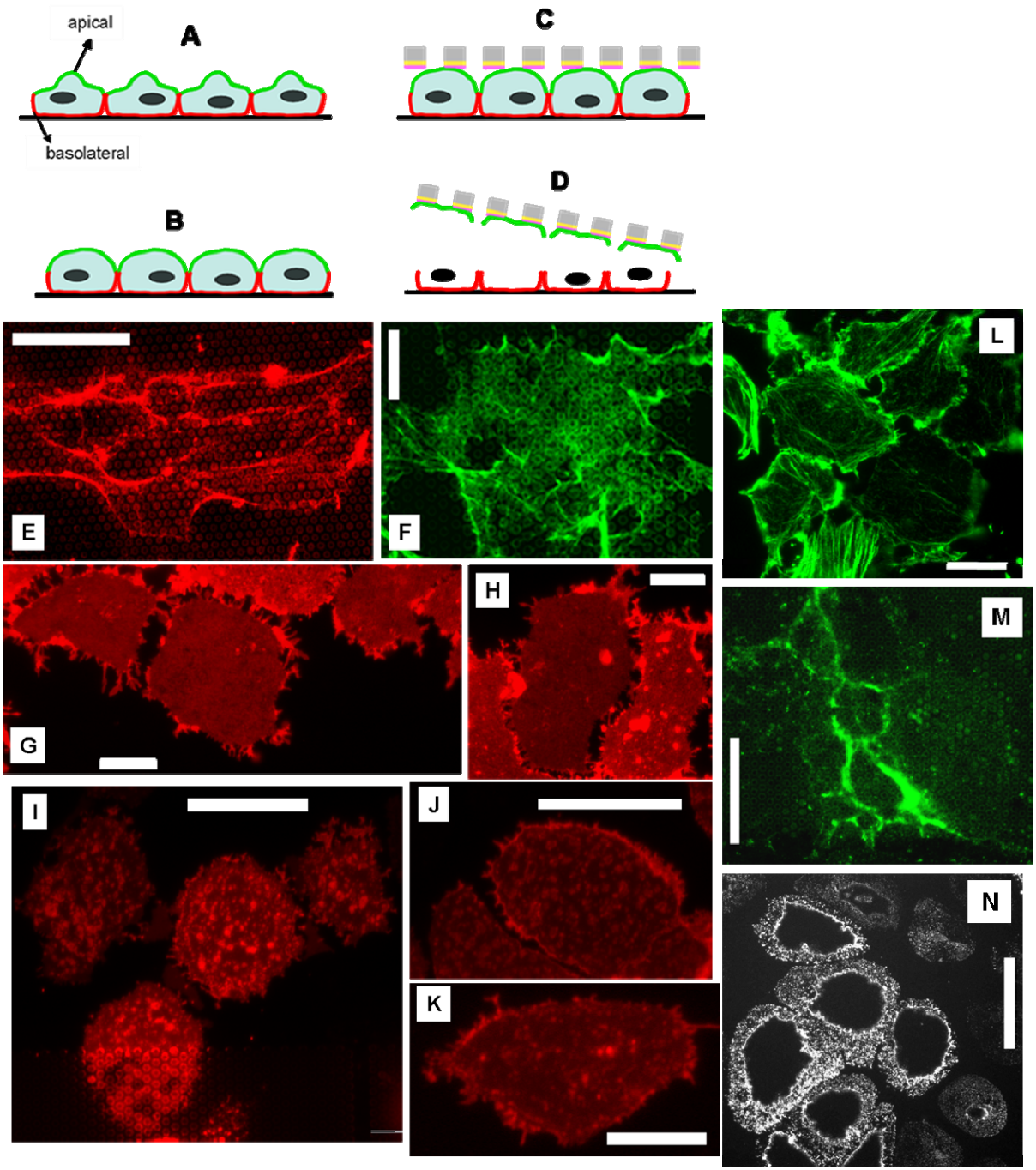

Figure 2.1.9.: A-D: Illustration of apical membrane preparation on porous chip and the remaining basolateral fragments. The green contour represents the apical membrane and the red contour represents the basolateral membrane. Collection of apical and basolateral membranes (cytoplasmic side) labeled with various fluorescence markers. E-F: apical membrane sheets transferred onto porous substrate and labeled with *Phalloidin* alexa546 (red) and *Phalloidin* alexa488 (green) for F-actin staining. Scale bar is 20 µm. G-H: basolateral fragments remained attached to the petri dish and were labeled with DiI for lipid staining. Scale bar is 10 µm. I-K: Apical membrane transferred to the pores and the rim and labeled with DiI. I-J: scale bar is 20 µm. K: scale bar is 10 µm. F-actin labeling with Phalloidin-alexa488: L: Basolateral membrane fragments. Scale bar is 10 µm. M: free standing apical membrane fragments. Scale bar is 20 µm. N: apical membrane fragments transferred to a glass labeled with anti gp135 mAb (MDCK apical membrane marker) and a secondary Ab conjugated to FITC. Scale bar is 20 µm.

Cellular aggregates were removed by shear stress (Nermut 1989) with a stream of PBS injected from a syringe with a 25 gauge canula (outer diameter: 0.5 mm). To extract cholesterol, apical membrane fragments were incubated with 20 μM MBCD (methyl β cyclodextrin, Sigma: C4555) in PBS for 30 min at 25˚C.

3.1.0: AFM measurement of living cells

To estimate the degree of cell coverage on the porous substrates, a Phase contrast microscope (Olympus) was used. Just before AFM measurements, the cells were washed by dipping the chips in a PBS (138 mM NaCl, 13 mM Na_2HPO_4, 1.5 mM KH_2PO_4, 2.7 mM KCl, 1 mM $MgCl_2$, 0.1 mM $CaCl_2$) solution for a few seconds. Then the chips were transferred to a self-designed measuring cell (Mainz University workshop) filled with PBS. The purpose of this measuring cell was to keep the chip immobilize in a buffer solution during AFM measurements. Top view optic of the AFM (Asylum, Santa Barbara, USA) allowed the localization of cells of interest due to the special geometry of the chip. Force indentation curves were recorded immediately after imaging from the nuclear and edge regions of the cells. All measurements were carried out at 25^{o}C.

3.1.1: Fixation

The purpose of fixation is to preserve the structure of biological samples against destructive autolytic processes (Butt et al. 1990, 2005). Aldehydes penetrate rapidly into cells and membrane samples because of their low molecular weight. Two types of fixatives were used:

1) Paraformaldehyde (PFA): polymerized formaldehyde.

2) Glutardialdehyde (GDA): a five carbon compound containing two terminal aldehyde groups. Aldehydes react with amino groups of lysine, resulting in the formation of protein meshwork and a progressive increase in sample's firmness and stiffness. GDA can also react with lipids, carbohydrates and nucleic acids. Cells treated with paraformaldehyde are partially permeablized and they remain osmotically active. Glutataldehyde penetrates tissues slower than paraformaldehyde, but due to its bifunctionality it is capable of crosslinking proteins into a permanent state. Membrane sample were fixated with 4 % w/v PFA in PBS for 45 min or with 0.5% v/v GDA in PBS for 10 min. The following fixation steps were used before cell labeling with fluorescence markers (*Phalloidin*-alexa488/546 from Invitrogen, anti gp135 mAb, DAPI) in order to increase the membrane permeability: 2 % GDA for 30 s, 3% PFA for 20 min and 0.2% v/v Triton X-100 for 2 min. Two types of preparations were used to fixate cells in order to resolve the apical membrane microvilli (Braet et al. 1998, Morris et al. 1999, Kirby et al. 1998) with AFM: (a) preconfluent cells (seeding conc.: 10^6 cells/ml, 24 h cultivation time) cultivated on porous chip were fixated with 1% GDA in PBS overnight at 4^{o}C and then stored in PBS. In this case the chip was always kept in liquid. (b) Confluent/ preconfluent cells were cultivated on porous chips and were fixated as follows: (1) cell washing by dipping the chips in PBS solution for 10 s. (2) fixation in 3% GDA in PBS solution for 1 h. (2) The chips were dipped in increasing concentration of ethanol solutions: 50%, 70%, 90%, 100% for 3 s. (3) The chips were air dried for a few seconds and then stored in PBS. In general, the samples

were immediately measured with AFM in PBS. For a later use, the chips were stored in PBS at 4^0C. To induce microvilli swelling, confluent cells were incubated with MQ water for 3 min followed by fixation with 3% GDA in MQ. The samples were stored and measured in MQ water in order to maintain hypotonic conditions. For SEM imaging, both cells and membrane samples were fixated overnight in 4% PFA and then 1 h in 3% GDA. The sampled were dipped in increasing concentration of ethanol solutions for 3 s and then air dried for 1 h at room temperature.

3.1.2: F-actin depolymerization

To remove F-actin filaments from apical membrane samples, gelsolin (Hirata et al. 2005, Funatsu et al. 1990, Yin and Stossel 1979) and DNAse I (Podolski and Steck 1988, Hitchcock et al. 1976) as actin disrupters were used (Hirata et al. 2005. Gelsolin binds specifically to F-actin, thus promoting actin capping and decomposition.Apical membrane samples were incubated with 20 µg/ml gelsolin (www.cytoskeleton.com HPG6: human recombinant) for 30 min at 37^0C. Gelsolin buffer solution contains: 125 mM potassium acetate, 1.8 mM $CaCl_2$, 0.8 mM $MgCl_2$, 12 mM glucose and 25 mM HEPES, and protease inhibitors:10 µg/ml leupeptin and 20µM Calpain inhibitor I at pH 7.0. DNAseI interacts with F-actin and leading to its depolymerisation. As the exact mechanism is unknown, one possible explanation is that DNAseI binds to loosening sites of filament intra-strands. Another explanation is that DNAseI induces a change in the structure of the actin monomer which leads to dissociation of monomers from the filaments. Membrane samples were incubated with 5 U DNAseI (Invitrogen: 18047-019) for 3 h at 37^0C in reaction buffer containing: 10 mM Tris-HCl, 2.5 mM $MgCl_2$, 0.5 mM $CaCl_2$ at pH 7.5.

4. ELASTICITY OF MDCK II CELLS CULTIVATED ON POROUS SUBSTRATE AND MICROVILLI ORGANIZATION

4.1 Introduction

Cultivation of cells *in vitro* on a three-dimensional porous Si/SiO_2 substrate provides two main advantages over a planar rigid substrate: 1) it increases the nutrient supply into the cells because both apical and basal membranes are exposed to the same concentrations of nutrients, thus to the same microenvironment. This leads to normal cell polarity in comparison to cells cultivated on a flat two-dimensional substrate (Cukierman et al. 2001). 2) Micrometer size pores improve the spatial freedom of the cells which is necessary for their movement (Atala 2008). Previous studies have shown that the physical properties of the cultivating substrate, such as stiffness and geometry, induce changes both in cell morphology (Zahor et al. 2007, Yim and Leong 2005) and in biological functions, such as protein expression, cytoskeletal organization and adhesion (Choquet et al. 1997, Byfield et al. 2009), cell density (Lorenz et al.2009), cell viability (Wang et al. 2000), gene expression and cytokine production (Cukierman et al. 2001). According to the tensegrity model (Stamenović et al. 2006) mammalian cells maintain an isometric tension, "prestress", generated by contractile actin filaments, in order to sustain structural stability. The stiffness of the substrate is necessary to resist the forces generated by adherent cells (Wang et al. 2002), which feed back into the cells. The mechanical properties of the cells, such as tension, adhesion and stiffness are controlled by the level of prestress. Changing of the prestress level promotes restructuring of the cytoskeleton effecting biochemical reactions in the cell. The first part of this chapter is dedicated to question whether the special geometry of the porous substrate can influence the elastic response of the cells. The purpose of the second part is to shed light on the organization of apical membrane microvilli during cell polarization regarding density, height and length.

4.2 AFM and fluorescence imaging of MDCK II cells

To correlate fluorescence and height images of the same cells, the special geometry of the porous substrate was used, allowing the localization of labeled cells with epifluorescence microscope for AFM measurements. Figure 4.0 shows a merge image (C-D) of F-actin labeled confluent cells with AFM height. The cells were fixated with glutardialdehyde and stained with *Phalloidin*-Alexa488. Top view of the cells reveals the apical membrane (A), whereas the bottom focus plane reveals the pores beneath the cells (B). Confluent cells are tightly bound together by firm tight junction complexes at the cells' borders. These complexes, containing high concentration of F-actin filaments at the cell borders, are clearly visible with fluorescence images as intensified fluorescence areas (D). Highly confluent epithelial cells establish a terminally polarized cell monolayer with a complete segregation between the apical and basolateral membranes. The apical marker protein, gp135, is a transmembrane glycoprotein connected to the cytoskeleton (Ojakian and Schwimmer 1988, Meder et al. 2005). Terminally polarized cells express this glycoprotein only in apical membrane domains except for an exclusion area at the center of the membrane referring to the outgrowth area of the primary cilium

(Meder et al. 2005). Confluent cells were labeled with 3F2 anti gp135 mAb in order prove cell polarization (figure 4.1A).

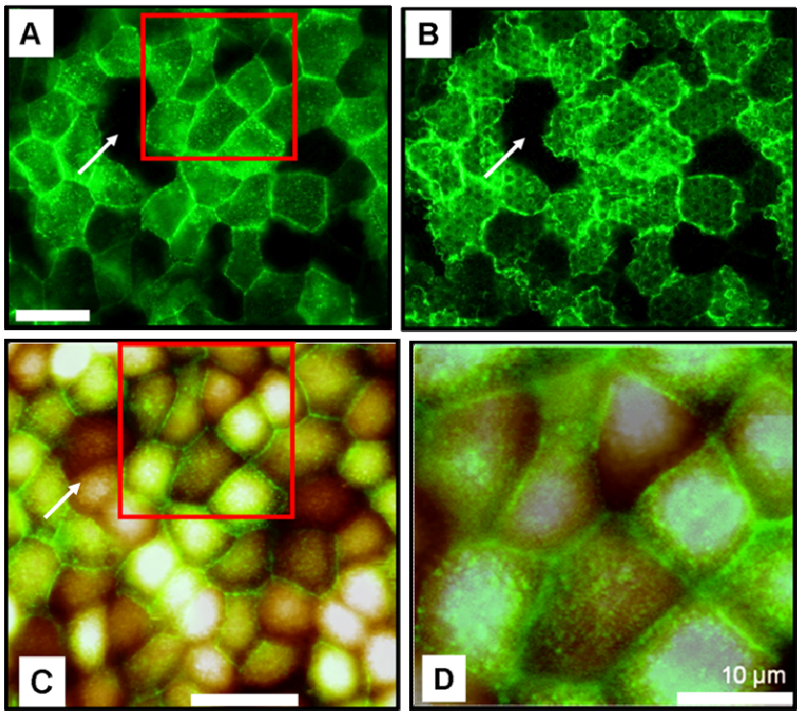

Figure 4.0: Top (A) and bottom view (B) of confluent MDCK II cells cultivated on porous substrate, fixated with GDA and labelled with *Phalloidin* Alexa488 (F-actin). Scale bar is 25 µm. C: Merge of height with the fluorescence image shown in A. D: Height superimposed with fluorescence image of the cells outlined in A and B. Scale bar is 10 µm.

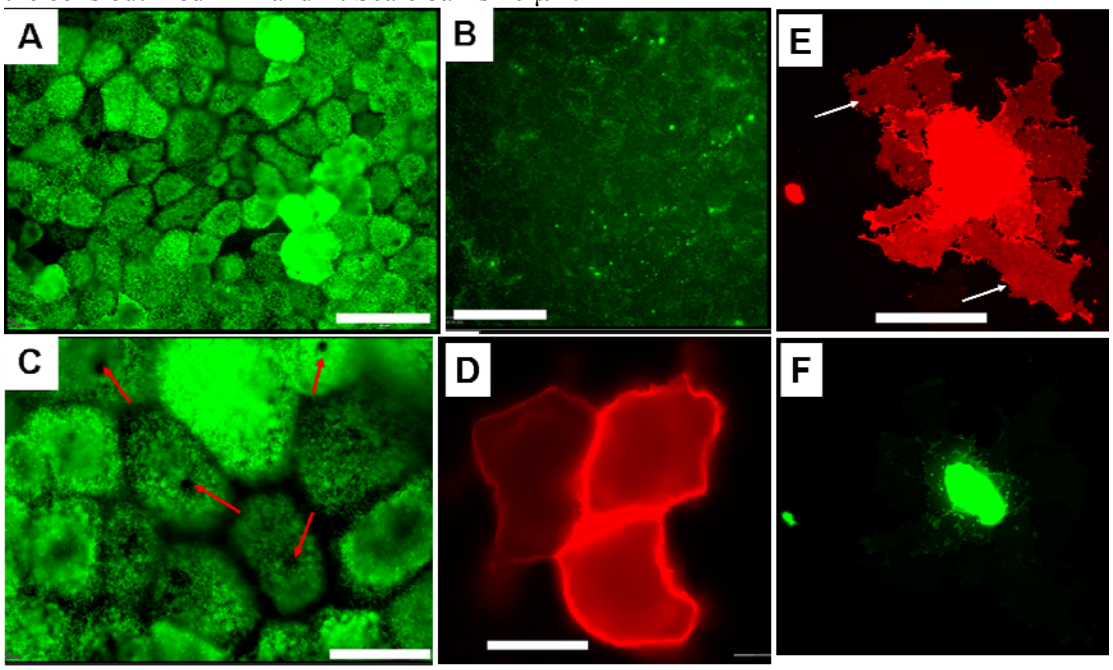

Figure 4.1: confluent MDCK II cells labeled with fluorescence markers. A: Staining with a monoclonal antibody (3F2) against an apical membrane marker: transmembrane glycoprotein (gp135). The secondary antibody (anti mouse IgG) is conjugated to FITC. B: confluent cells stained only with a secondary antibody (negative control 1). Scale bar is 50 µm. C: Magnified area from A. The red arrows point at exclusion areas in the apical membrane which are related to the growing site of the primary cilium. Scale bar is 20 µm. D: Lipid labeling with DiI. Scale bar is 25 µm. Basolateral membrane fragments, indicated by the arrows (E), were doubled labeled with anti gp135 (F) a

The red arrows (C) point at non stained areas, about 1-2 µm in diameter, referring to the outgrowth location of the primary cilium (Meder et al. 2005). Basolateral membrane fragments, prepared by squirting lysing (Lorenz et al. 2009) from confluent cells on a petri dish, were also labeled with the same antibodies as a negative control and visualized by lipid labeling with DiI (E). No fluorescence was recorded from gp135 labeled basolateral membranes (F), indicating that this protein is not expressed in basolateral membranes as would be expected from fully differentiated polarized cells.

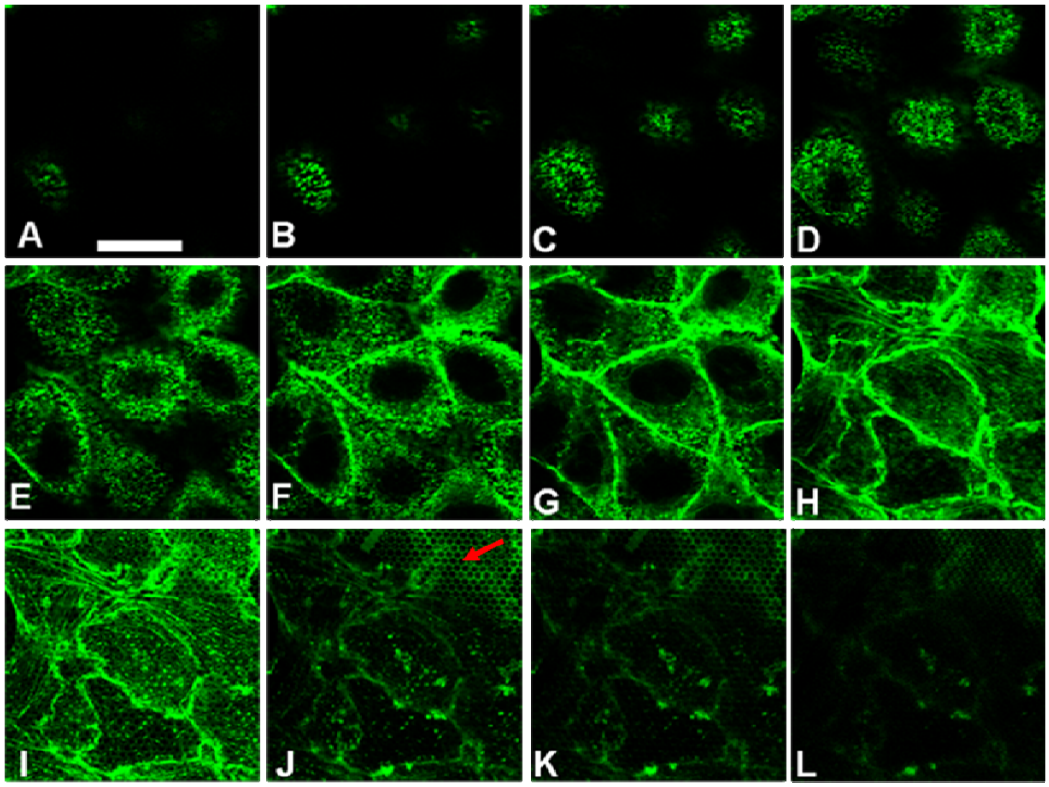

Figure 4.2.: A-L: CLSM z sections of F-Actin labeled MDCK II cells cultivated on porous substrate. The red arrow marks the pores under cells (J). Scale bar is 20 µm.

To estimate the cells' height on a porous substrate, z optical sections from the upper apical membrane (A-D) to the underlying porous substrate (I-E) were recorded with CLSM (figure 4.2).

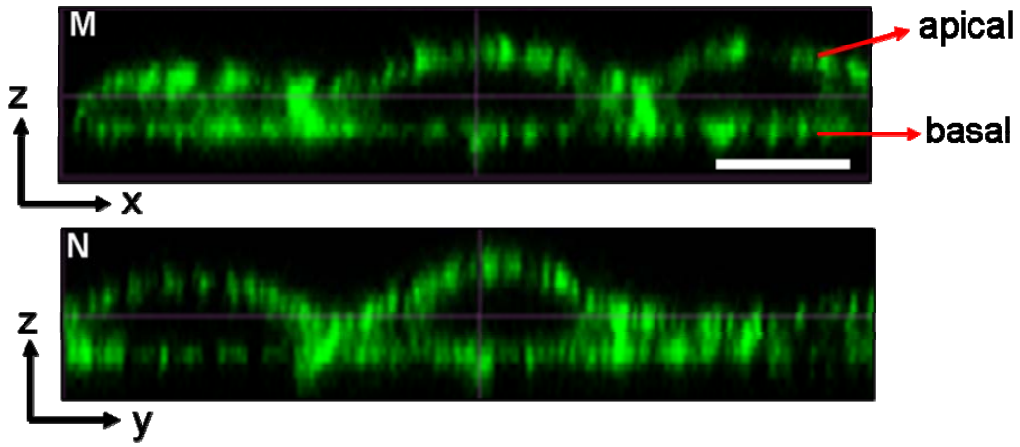

Side view sections: z/x (M) and z/y (N), revealing the apical and basolateral poles of the cells. Scale bar is 10 µm.

F-actin labeling was used as a fluorescence marker because actin filaments localize close to the apical membrane, composing the core of the microvilli, and the basolateral membrane as stress fibers. Side views of confluent cells (M-N) reveal a maximal height of 8.5 µm in good accordance with that recorded from MDCK II cells on a petri dish (Steltenkamp et al. 2006) and a glass slide (Hoh and Schoenenberger 1994).

Chemical fixation of cells with glutardialdehyde increases the stiffness of the sample due to protein cross linking (Butt et al. 1991). In comparison to fixated cells (figure 4.3C), living cells (A) are soft and highly deformable (Hoh and Schoenenberger, A-Hassen et al. 1998).

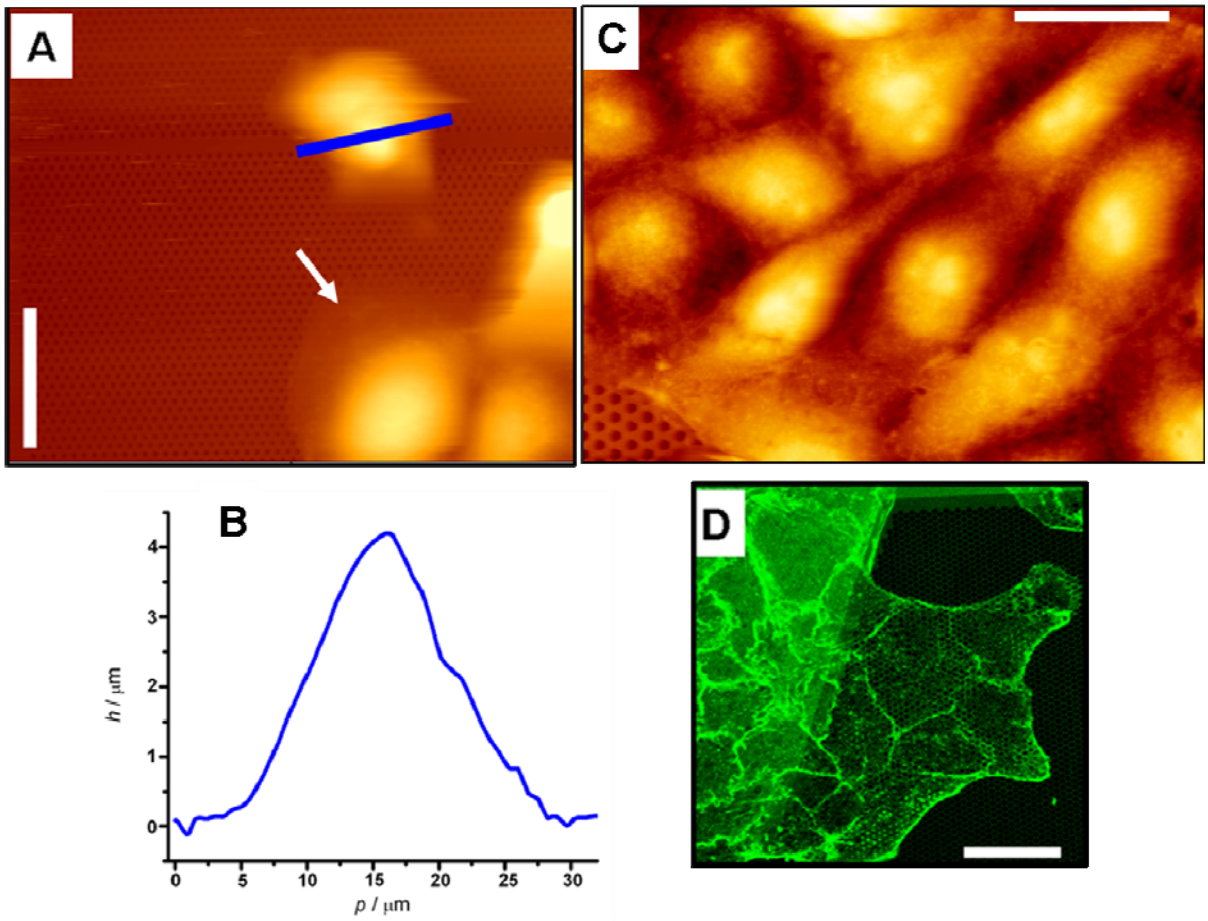

Figure 4.3: Height images of preconfluent living on 1.2 µm size pores (A) and GDA fixated cells on 2 µm size pores (C).B: Height profile, recorded from a living cell, refers to the cross line shown in A. D: CLSM of preconfluent fixated cells labeled with *Phalloidin*-alexa488. A and C: Scale bar is 25 µm. D: Scale bar is 20 µm.

In the height image (figure 4.3A) light areas are higher than dark areas. Maximal height of 4.2 µm was recorded from a living cell relative to the pores' rim (figure 4.3B), indicating significant cell indentation under the pressure of the AFM tip. Cell deformation leads to reduction of the cell height, termed "height anomaly" (Weisenhorn et al. 1993), and underestimation of the sample's thickness when recorded with an AFM height profile (Müller et al. 1999). Sequential height images of the same cells (figure 4.4) at high (A) and low (B) scanning forces show that cell deformation is reversible and it depends on the applied imaging force. At high force scanning, the pores under the cell periphery are

revealed (figure 4.4A), whereas at low force imaging there are not visible (4.4B), suggesting cell deformation in z direction into the pores when a high force is applied.

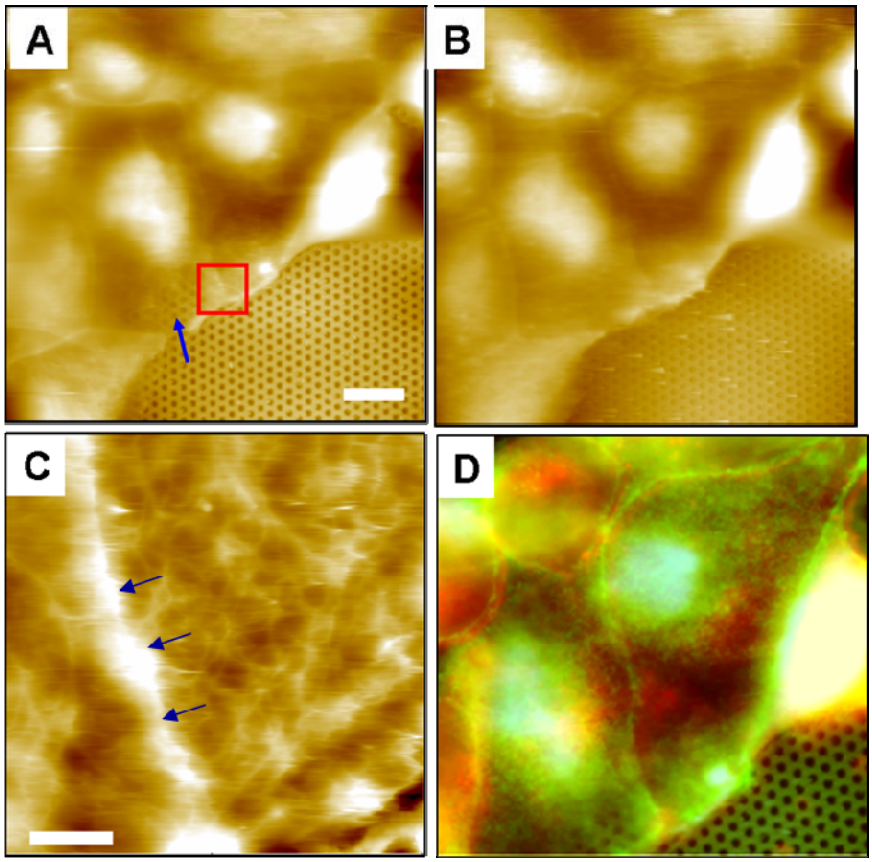

Figure 4.4.: Height and fluorescence images of preconfluent living cells on porous substrate. The same cells were imaged with high (A) and low (B) forces. Scale bar is 10 µm. The blue arrow (A) points at the pores revealed under the cell. C: Height image of the area outlined in A exposing a dense network of cytoskeleton at the cell edge. The stiff border between adjacent cells is marked bt the red arrows. Scale bar is 2 µm. D: Height superimposed with fluorescence images. The cells were doubled labeled with DiI (red) for lipid staining and *Phalloidin* Alexa488 (green) for F-actin staining.

Lateral deformation, indicated by comparing trace (scan direction: left to right) and retrace (scan direction: right to left) images was not observed. The most prominent features in an AFM height image of living cells are the nucleus and the cell borders. Cell-cell contacts, marked by the red arrows (4.4C), are stiff due to high concentration of F-actin (4.4D) composing the tight junctions, whereas the nuclear region and the cell periphery close to the nucleus are softer (A-Hassen et al. 1998). Inner cyoskeleton fibers (4.4.C) underlying the cell surface are exposed due to apical membrane deformation (Rotsch and Radmacher 2000). The cell mobile edge, termed lamellipodium, is clearly visible in the height image of preconfluent cells (figure 4.3A) marked by the white arrow. It is a large, broad, protrusive, and thin (< 1 µm) area of the leading edge of an advancing cell (Mahaffy et al. 2004) with an extension rate: 15-30 nm/s (Mallavarapu and Mitchison 1999).

To demonstrate the effect of chemical fixation on the image resolution, height images of the same cells, cultivated on porous substrate (figure 4.5B), were recorded before (D) and after (E) fixation with 2% glutardialdehyde for 10 min. Stiffness can be defined as: $S = \frac{\partial F}{\partial z}$ (Pethica and Oliver 1987).

Cell fixation is a rapid chemical process of protein cross linking which reduces cell deformation, z, under load F, giving rise to an increase of the sample stiffness (S). Previous studies have shown (Hoh and Schoenenberger 1994) that cell fixation with 2% glutardialdehyde is completed in less than 80s demonstrated by a decreasing indentation depth recorded by force indentation curves. On a hard stiff surface the contact area between the tip and the sample is reduced, enabling to resolve smaller objects (Shao 1996, Weihs et al. 1991).

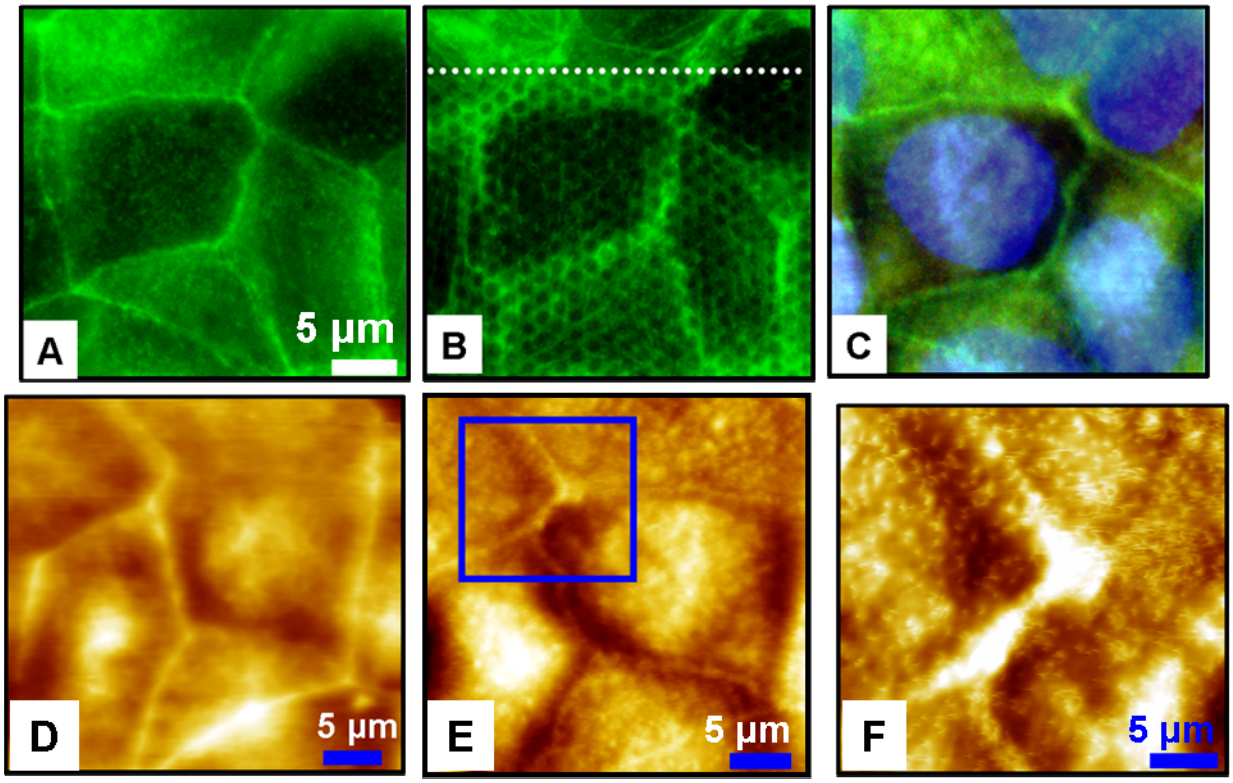

Figure 4.5: Height images of highly confluent MDCK II cells before (D) and after (E-G) fixation with glutardialdehyde. A-C: Top and bottom view of the same cell position labeled with *Phalloidin*-alexa488 for F-actin staining. C: Merge of fluorescence (DAPI +*Phalloidin*-alexa488) and height.

The reported height profile following fixation (H) reveals a highly corrugated surface due to the presence of microvilli (G), which are permanent apical membrane folds (Lange and Gartzke 2001, McMahon and Gallop 2005). However, mechanical interactions between the tip and the microvilli make it impossible to fully resolve their dimension from living cells (Baret et al. 1988, Gorelik et al. 2003) by contact mode imaging.

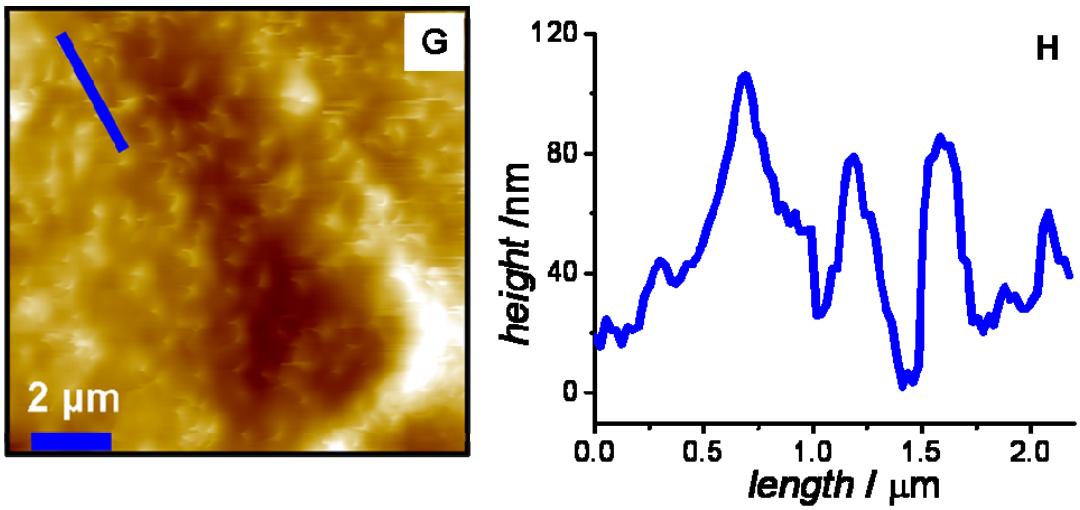

G: Zoom in to the area marked in E. H: Height profile, relating to the cross line shown in G, indicates a corrugated apical membrane surface due to the mechanical stabilization of microvilli.

F-actin labeling of cells with *Phalloidin*-alexa488 at the interface of porous and non porous substrate reveals uneven distribution (figure 4.6) of actin stress fibers between cells cultivated on pores and rim.

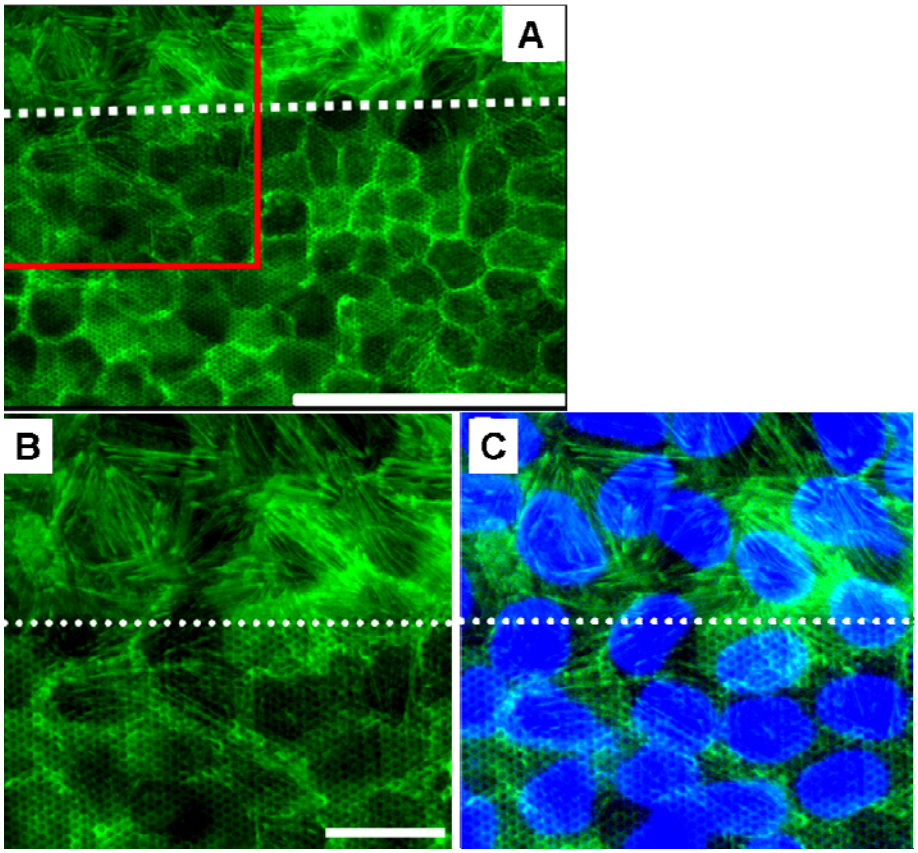

Figure 4.6: A: Cells were labeled with *Phalloidin* Alexa488 for F-actin staining. The dash line indicates the border between the porous area and the rim, indicating uneven distribution of actin stress fibers in cells on the porous and the non-porous areas. Scale bar is 100 µm. B and C zoom in to the marked area in A. Scale bar is 25 µm. C: double labeling with DAPI reveals the cells' nuclei.

Cells cultivated on the rim exhibit denser distribution of actin filaments. Since F-actin plays a key role in determining the mechanical properties of cells (Rotsch and Radmacher 2000), the goal of the following section was to investigate weather cultivation of cells on a porous substrate leads to cytoskeletal rearrangements, which can be detected by elasticity measurement with an AFM.

4.3 Force indentation of cells on porous substrate

Figure 4.7 displays top (A) and bottom (B) views of confluent cells cultivated on porous substrate.

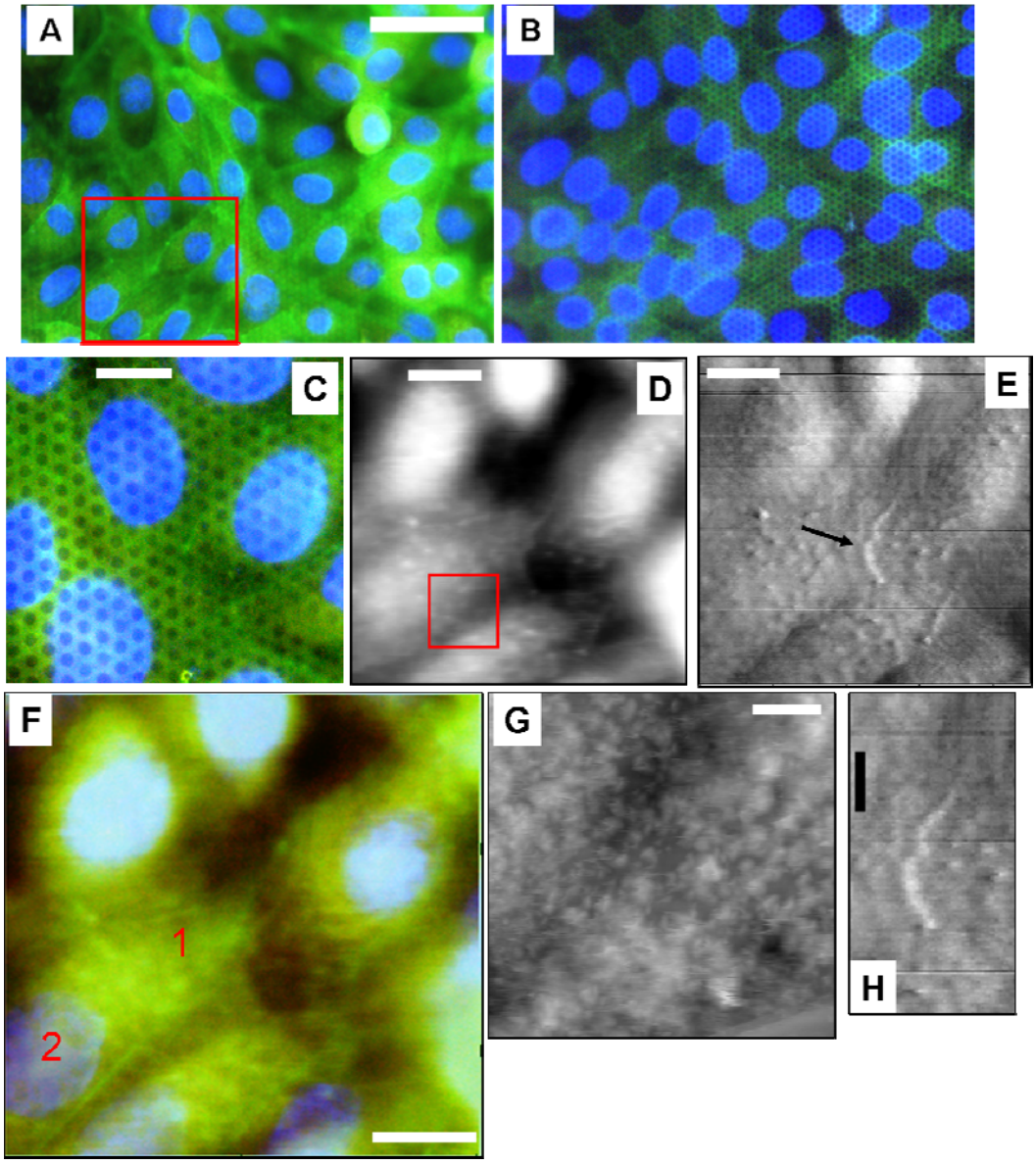

Figure 4.7: Top (A) and bottom (B) view of confluent MDCK II cells cultivated on porous substrate with 1.2 µm sized pores. The cells were doubled labeled with DAPI (nucleic acid staining) and *Phalloidin*-Alexa488 (F-actin). Scale bar is 50 µm. C is a magnified area of the marked cells in A revealing the pores beneath the cells. Scale bar is 10 µm. D & E: are the matching height and lateral deflection images, respectively, of living cells. The black arrow (E) points at a long protrusion related to the primary cilium. Scale bar is 10 µm. F: Merge of fluorescence and height images. Numbers 1 and 2 relate to the cell periphery and the nuclear region, respectively. G: Height image following fixation with 2% GDA for 10 min revealing apical membrane microvilli. Scale bar is 3 µm. H: Magnified area from E. Scale bar is 5 µm.

The height image of living cells (D) refers to the marked area in A. The lateral deflection image (E), which is generated out of the non-feedback signals and its contrast is based on the friction between the tip and sample, reveals a long protrusion- about 12 µm in length. This structure is possibly related to the primary cilium (Evangelides et al. 2008, 2009), a hair like immotile structure projecting from the apical membrane of kidney epithelial cells.

The viscoelastic response of living cells to an external load with an AFM tip is non linear (A-Hassan et al. 2008, Mahaffy et al. 2004, Pelling et al. 2007). In order to extract the Young's modulus of the cells, force indentation curves were taken from two distinct regions of the cell: 1) periphery relating the area close to the nucleus. 2) Nucleus region as the highest area in the cells' topography (D). These regions are designated 1 and 2, respectively, in the height-fluorescence merge display (F).

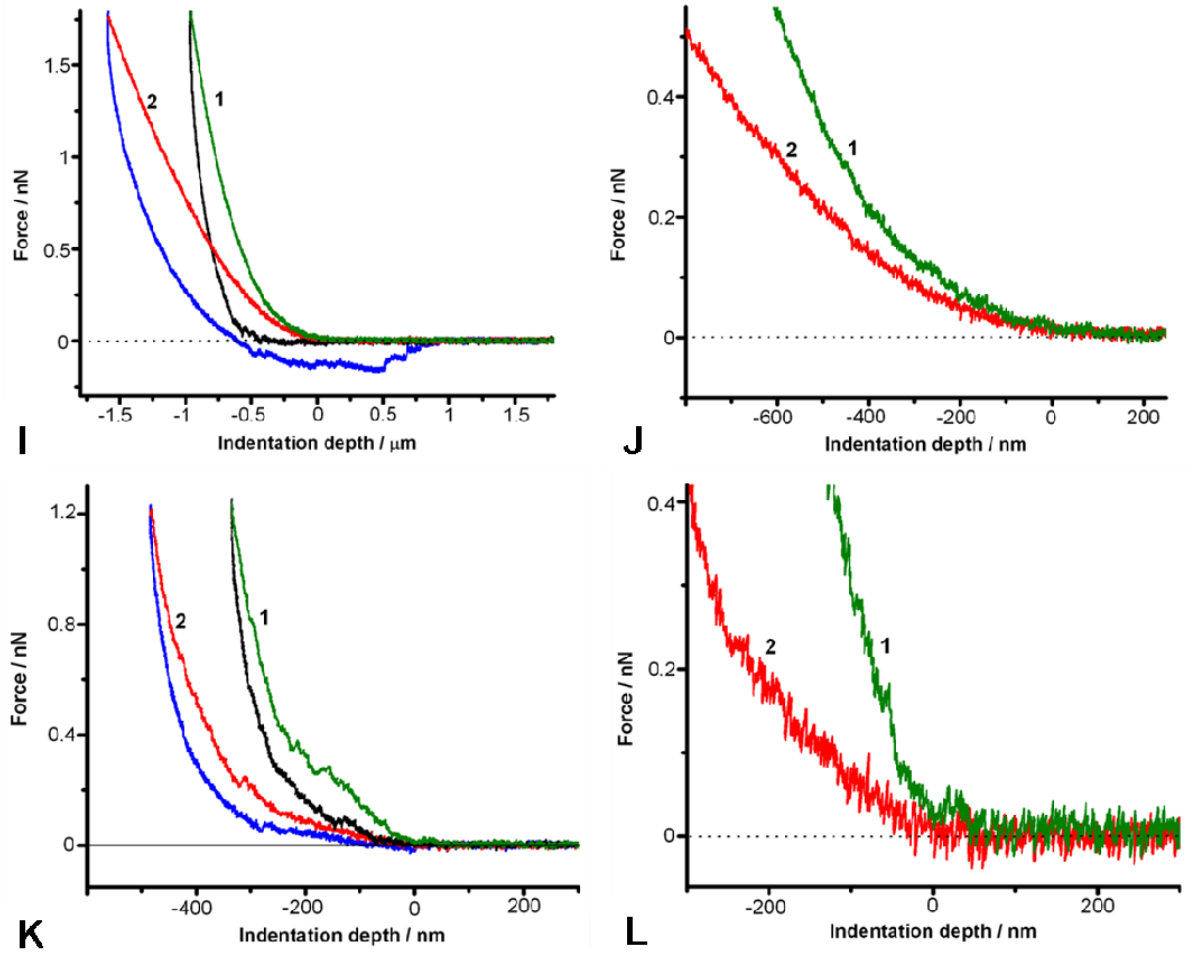

Force indentation curves were recorded from the cell edge (1) and the nuclear region of a living cell (2) before (I) and after (K) fixation with 2% GDA for 10 min. The red and green curves are the approaching curves from the nuclear region and the cell edge, respectively. The blue and black curves are the retracting curves from the nuclear region and the cell edge, respectively. J: Zoom in to the first 800 nm of indentation from I. L: Zoom in to the first 300 nm of indentation from K.

M

Living cells	Young's modulus/ *kPa*	Normalized hysteresis
nucleus	2.2 ± 1.1	0.57 ± 0.04
periphery	3.4 ± 1.8	0.54 ± 0.001

M: Young's modulus and normalized hysteresis calculated from the nuclear region and the periphery of living cells.

Force indentation recorded before (I) and after fixation with 2% glutardialdehyde for 10 min (K) exhibit a viscoelastic response, indicated by hysteresis between the approaching and the retracting curves at the contact regime (Mathur et al. 2001). The cells' viscoelasticity stems from two main factors (Trickey et al. 2004, Kamm and Mofrad 2006): (1) flow-dependent mechanisms, such as fluid-solid interactions and fluid viscosity. (2) Flow-independent mechanisms, such as the intrinsic viscoelasticity of the cytoskeleton.

The normalized hysteresis represents the ratio between the hysteresis and the area under the approaching curve in the contact regime (Butt et al. 2005). These values (M), calculated from force indentation curves in the nucleus region and the periphery close to the nucleus, show no difference, indicating the same viscoelastic property of the indented material in these cellular parts.

The Young's modulus, *E,* was extracted by fitting the first 200 nm of indentation, *z*, from the approaching curve with the following equation matching to a cone shaped cantilever tip (Sneddon 1965): $F(z) = \frac{2E}{\pi\left(1-\nu^2\right)\tan\alpha} z^2$.

Force indentation curves were fitted with a constant Poisson ratio, *v*, of 0.5 in good agreement with a previous report (Mahaffy et al. 2004). The half-opening angle, *α,* of a cone shaped tip (MSCT-C lever) is 35°. The nucleus region of the cells cultivated on a porous substrate reported a Young's modulus: $(2.2 \pm 1.1)\,kPa$, which is 4 fold lower than that reported from the same cell line cultivated on a non porous substrate with the same tip geometry (Steltenkamp 2006). The area close to the nucleus, named periphery, reported a Young's modulus: $(3.4 \pm 1.8)\,kPa$, which is about the same of that reported previously from non porous substrate under isotonic buffer conditions (Steltenkamp 2006). These results suggest that lower distribution of F-actin in MDCK II cells cultivated on porous substrate, indicated by fluorescence labeling with *Phalloidin*-alexa488, leads to a softer mechanical response, meaning lower resistance to an external load. In addition, it shows that there is no significant difference in the cell's elasticity between the nucleus region and the periphery at small forces. The difference in indentation depth at high forces is related to the contribution of the underlying substrate (Kidoaki et al. 2006, Domke and Radmacher 1998, Mahaffy et al. 2004). The cell's periphery is

thinner in height (figure 4.7D) than the nucleus region (Hoh and Schoenenberger 1994). Therefore, at high forces, the cantilever tip senses the underlying substrate which results in higher resistance to to the applied force.

It was recently reported (Byfield et al. 2009) that endothelial cells cultivated in a stiff gel substrate show dense distribution of actin stress fibers and exhibit higher stiffness than those cultivated in a compliant gel substrate. According to the tensegrity model (Stamenović et al. 2006) cellular forces, generated by actin filaments, are transferred into the the cells' substrate and then feed back into the cells, which maintain a level of prestress. Any disturbance of this force balance can lead to cytoskeleton rearrangments. Therefore, it is suggested that a porous substrate with 1.2 μm sized pores provides smaller resistance to the adherent cells than that provided by a flat, stiff, non porous substrate. This may lead to structural rearrangement withing the cytoskeleton, indicated by lower expression of actin fibers resulting in a decrease of the cells' stiffness.

Following cell fixation with 2% glutardialdehyde, a linear regime was recorded over the first 200 nm of indentation (figure 4.7K). Therefore, linear regression (R^2 = 0.97) over this indentation depth was calculated as an indication to the cell stiffness after fixation. 1.6 mN/m and 0.4 mN/m, were found for the periphery and the nucleus region, respectively (L). It was previously reported that cell fixation with 2% glutardialdehyde results in cell thinning (Hoh and Schoenenberger 1994). Therefore, a reasonable explaination to the significant difference in the mechanical response between the cell's periphery and the nucleus region is attributed to the increasing effect of the underlying substrate under the cell's periphery due to the cells' schrinkage.

4.4 Force indentation of cell edge

Force indentation curves taken from thin films (< 1μm), such as the cell edge, show a strong substrate effect on the sample's elastic response (Mahaffy et al. 2004), leading to overestimation of the cell's elasticity. Figure 4.8 displays height images (A-B) of the cell edge fixated with 2% glutardialdehyde.

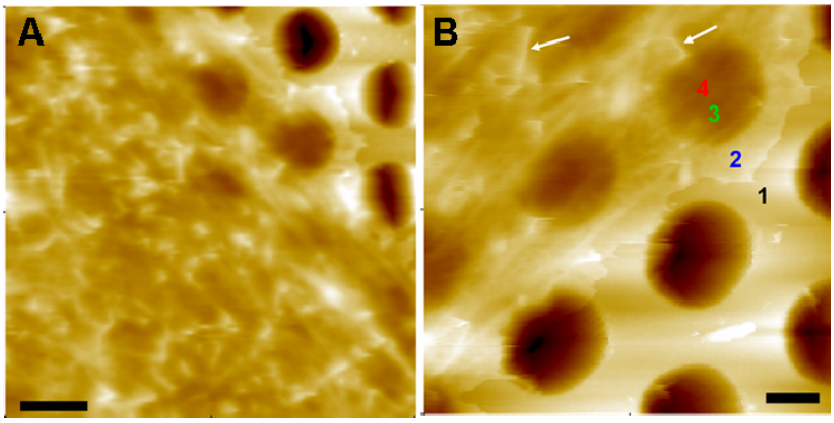

Figure 4.8: Height images of the cell edge fixated with GDA. Pore size: 2 μm. A: scale bar is 2 μm. B: scale bar is 1 μm. C: Force indentation curves were recorded from an empty rim (1), cell edge covering the rim (2), and the pore (3-4) marked in B. The white arrows point at microvilli.

In order to estimate the effect of the substrate on the sample stiffness recorded from the cell edge, force indentation curves (4.8C) were taken from a non covered rim (1) and the cell edge covering a rim (2) and a pore (3-4). The force *F* is plotted against the vertical piezo movement *z*. To calculate the indentation depth, the deformation reported from a covered rim and a covered pore must be substructed from that of an empty rim (Domke and Radmacher 1988). At 0.5 nN, indentation depths of 60 nm, 200 nm and 240 nm are reported from a covered rim (2) and a covered pore (3-4), respectively, demonstrating lower resistance to deformation into a covered pore.

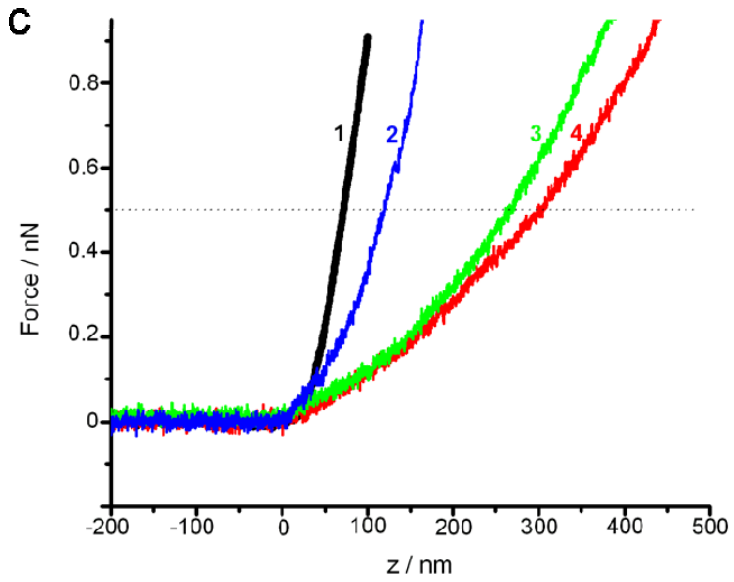

C: Force indentation curves recorded from the point marked in B. 1: empty rim (black), 2: cell edge covering the rim (blue), 3-4: cell edge covering a 2 µm size pore (green and red). z/ nm relates to the vertical piezo movement.

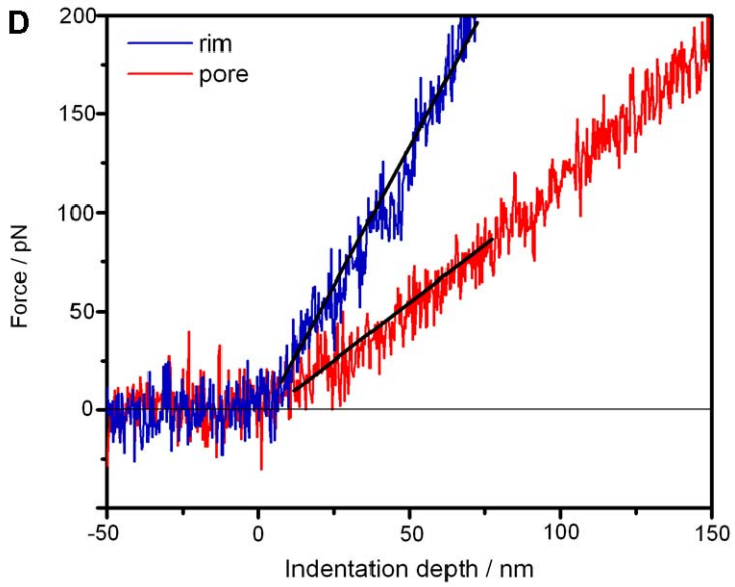

D: zoom in to the linear region of cell edge deformation. The linear slopes were calculated over the first 100 nm of indentation reporting a difference of 3 fold in the stiffness between a covered rim and a covered pore.

A linear regime of force versus indentation was found over the first 150 nm of indentation (D). The slope of the curve calculated from a covered pore (1 *mN/m*) is 3 fold smaller than that from a covered rim (3 *mN/m*), indicating the contribution of the stiff rim on the reported elastic response. The significant advantage of using a porous substrate over a non porous flat support to exclude the substrate effect motivated us to prepare free standing apical membranes (chapter 5) as an optimal setup to map the elastic response of apical membranes.

4.5 Microvilli organization

The topographical organization of kidney epithelial apical membranes (figure 4.9A) is characterized by microvillar domains and planar sub-domains (McAteer et al. 1986, Poole et al. 2004). Time-laps images of microvilli from living kidney epithelial cells with Scanning Ion Conductance Microscope (SICM) revealed a dynamic growth cycle with an average duration of 12 min (Gorelik et al. 2003). It consists of three phases: 1) microvilli formation exhibiting a nonlinearly growth rate of 5 nm/s. 2) steady state. 3) Retraction rate of 1.2 nm/s. The goal of this section was to quantify morphological changes of apical membrane microvilli from an early and late polarization states. MDCK II (10^6 cells/ml) were seeded on porous substrates and cultivated for 48h (confluent) and 72h (highly confluent). Apicl membrane microvilli are clearly visible from the recorded height images after fixation with 2% glutardialdehyde (figure 4.9). However, surface deformation and mechanical interactions that still exist between the microvilli and the tip (Poole et al. 2004, Braet et al. 1998) can lead to underestimation of their heigh.

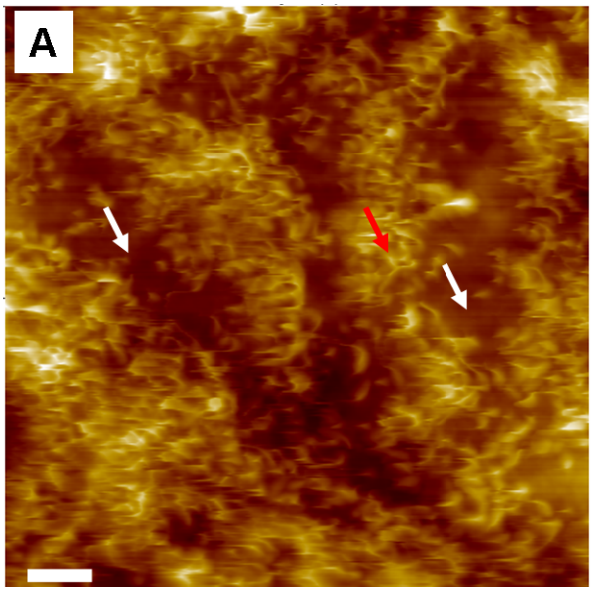

Figure 4.9: Height images of MDCK II cells fixated with GDA. A: fixation with 2% GDA for 20 min reveals planar and microvilli membrane domains indicated by the red and white arrows, respectively. Scale bar is 1 µm.

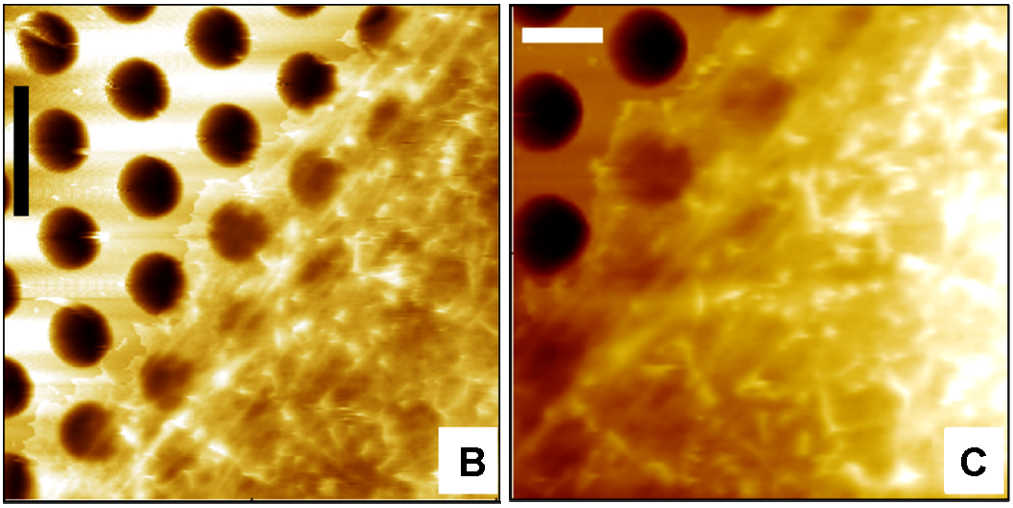

Figure 4.9: B & C: cell edge. Fixation with 1% GDA for 12 h. B: Scale bar is 4 µm. C: Scale bar is 2 µm.

In order to trap one state in the microvilli growth cycle and to increase the sample's stiffness, the cells were fixated with glutardialdehyde followed by dehydration with a series of ethanol solutions (Kirby et al. 1998) and then immersed in PBS for AFM scanning.

Height images from cells cultivated for 48h (figure 4.1.0) and 72h (figure 4.1.1) were analysed to quantify topographic information about microvilli density, length and diameter. The data is displayed in histograms and summarized in Table 1. Single microvilli can be clearly resolved from cells after 48h of cultivation, whereas after 72h the apical surface becomes highly villiated. Variable distribution in length recorded from the same cell monolayer after 48h (figure 4.1.0 A-C) is related to the dynamic cycles of microvilli growth and retraction which can vary between cells (Gorelik et al. 2003). Microvilli elongation from $(377 \pm 112.1)\,nm$ after 48h to $(549.2 \pm 91.6)\,nm$ after 72h is related to the growth cycle of the cells from an early to late polarization state (Lange and Gartzke 2001, Knutton et al. 1975). Previous measurements of microvilli length, carried out with SEM from mastocytoma cells (Knutton et al. 1975) and with scanning ion conductance microscope (Gorelik et al. 2003) from *Xenopus* kidney epithelial cells, reported an average length of 0.4 µm. SEM images, acquired from preconfluent MDCK II sells (figure 4.1.2), reveal about the same microvilli length. The average microvilli diameter values after 48h and 72h, $(55.4 \pm 15.8)\,nm$ and $(63.2 \pm 17.7)\,nm$, respectively, are in good agreement with that reported (Lange and Gartzke 2001) about hepatocytes (60 *nm*).

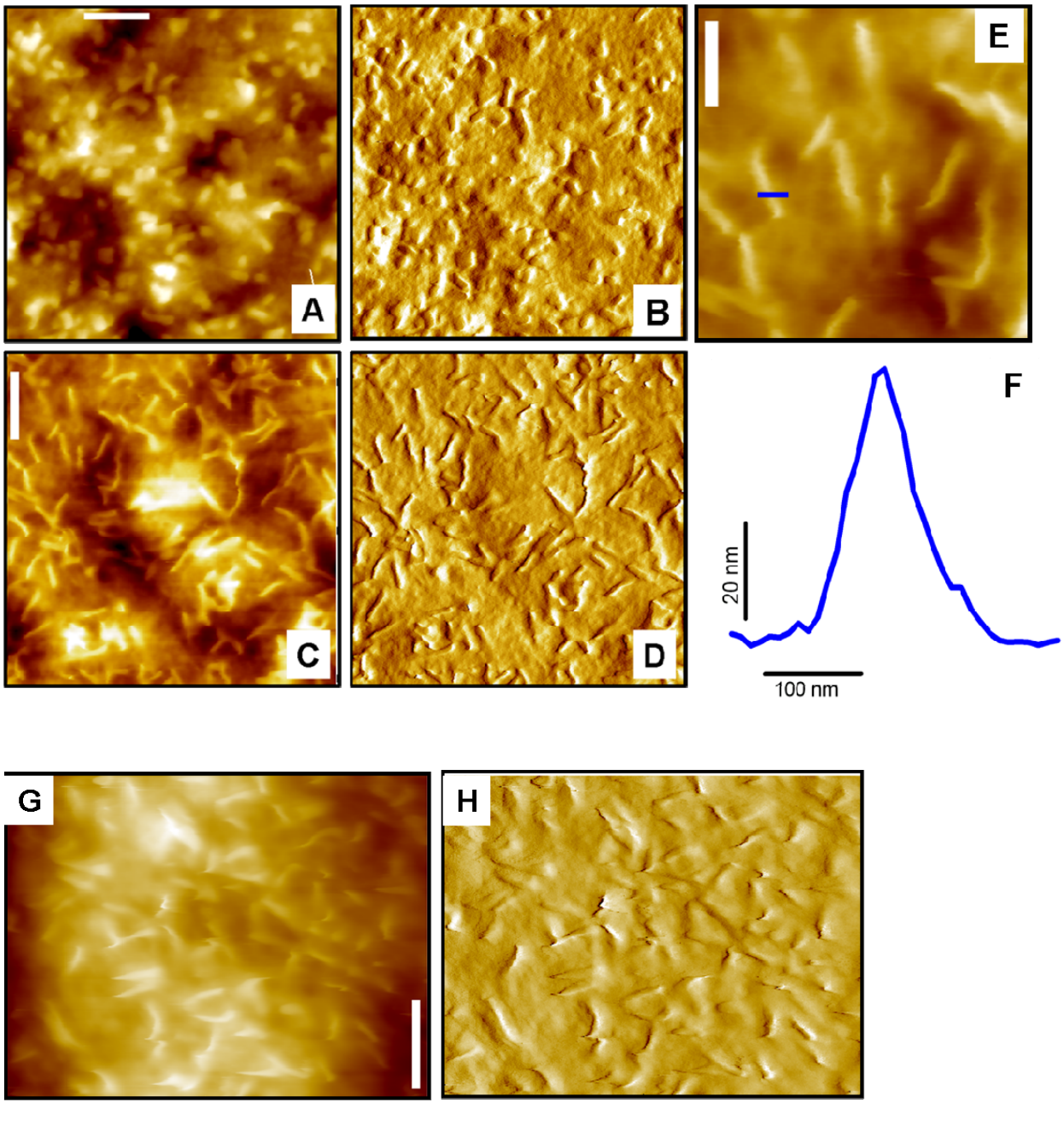

Figure 4.1.0: Collection of height (A, C, G) and the corresponding deflection (B, D, H) images of microvilli from confluent cells cultivated for 48 h on porous substrate. Scale bar is 1 µm. The cells were fixated with GDA followed by immersion in increasing concentration of ethanol solutions, air dried, and then storage and measurement in PBS. Microvilli can be clearly distinguished from planar sub domains. E: magnified area from C. Scale bar is 0.5 µm. F: Height profile refers to the blue cross line in E.

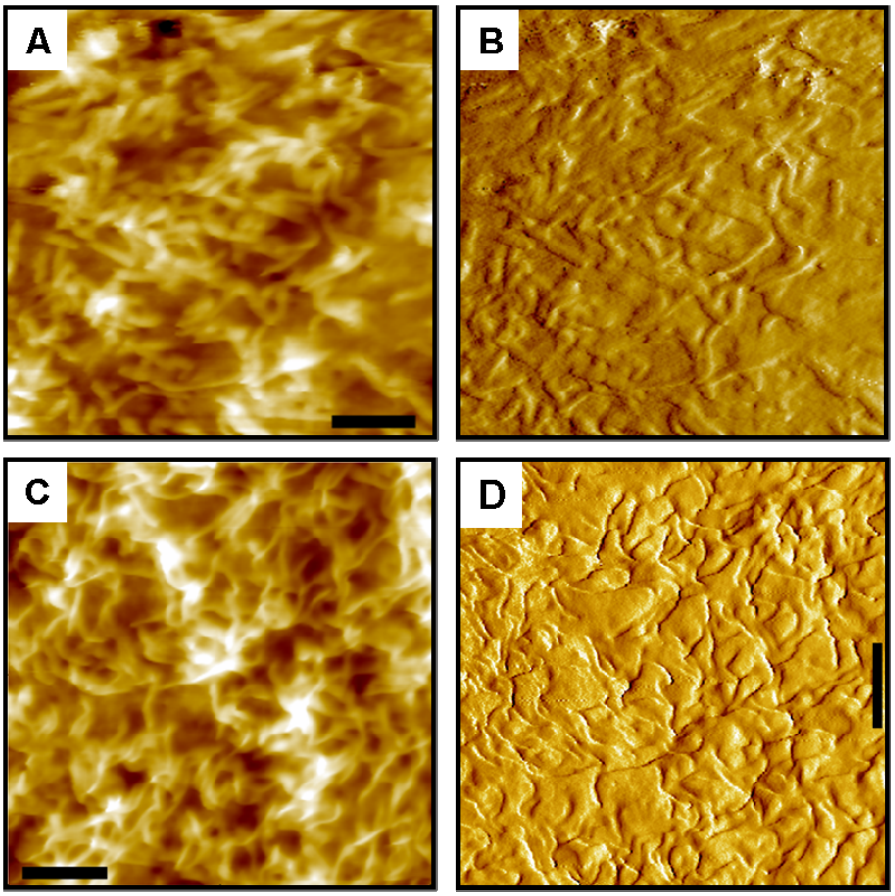

Figure 4.1.1: Height (A and C) and the corresponding deflection (B and D) images of apical membrane microvilli from highly confluent MDCK II cells cultivated for 72 h on porous substrate. Scale bar is 1 µm. Sample handling was as described in figure 4.8.

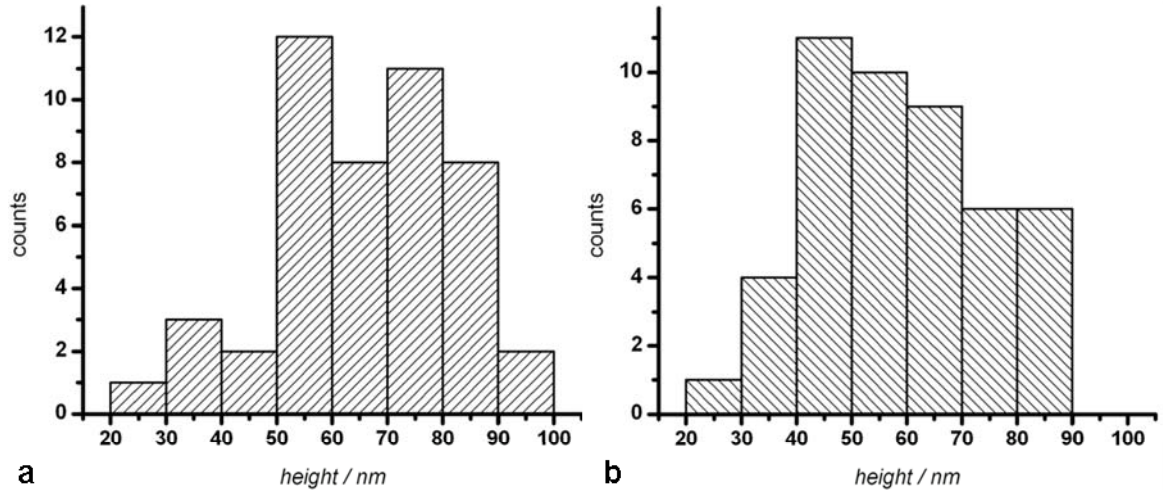

Figure 4.1.2: Histogram display of distributions of the microvilli height after 48 h (a) and 72 h (b) of cell cultivation.

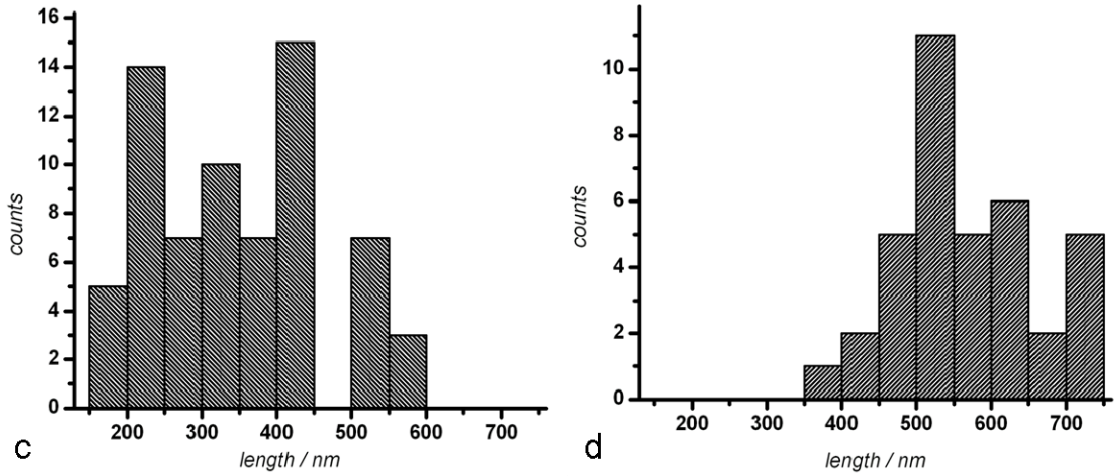

Microvilli length measured after 48 h (c) and 72 h (e) of cell cultivation.

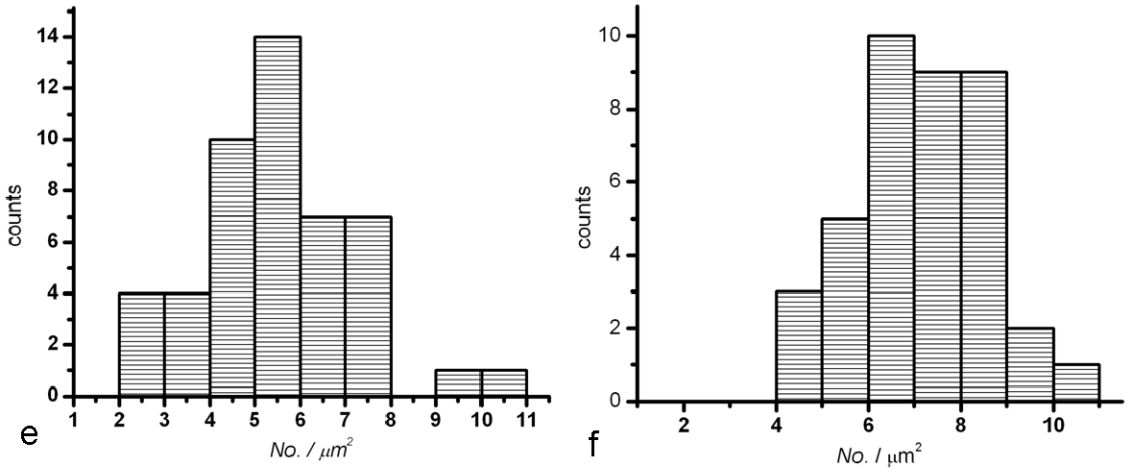

Microvilli length measured after 48 h (c) and 72 h (e) of cell cultivation.

Image number	**Cell confluency**	**Density** *No./μm²*	**Length** / *nm*	**Height** / *nm*
4.8A	+	5.1±1.9	245.9±67.7	71.0±15.4
4.8B	+	5.2±1.9	425.0±71.4	55.6±16.6
4.9A	++	6.6±1.7	559.3±87.2	45.8±11.3
4.9C	++	6.7±1.3	542.3±95.9	65.0±13.8

Table 1: microvilli's topographic data: density, length and diameter. Height images shown from figures 4.8 and 4.9 were analyzed by cross section measurements. + relates to 48 h and ++ relates to 72 h cell cultivation time on porous substrate. The density was determined by counting the number of microvilli in a 1 μm^2 size area.

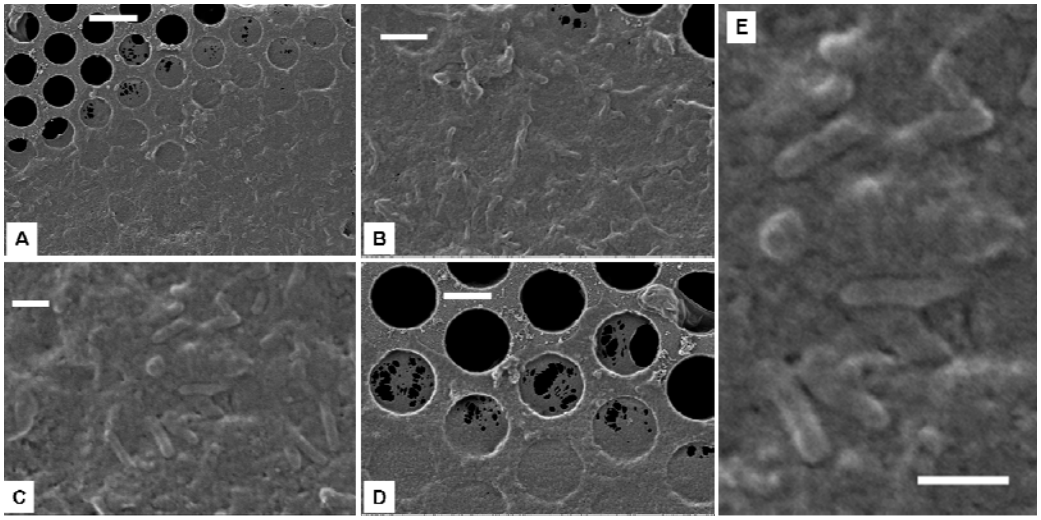

Figure 4.1.3: SEM images of apical membrane microvilli and the cell edge acquired from preconfluent cells. A: Scale bar is 2 µm. B and D: Scale bar is 1µm. C: Scale bar is 0.4 µm. E: a magnified region from C. Scale bar is 0.4 µm.

Cells under hyposmotic stress use the membrane area covering the microvilli to swell (Sukhorukov et al. 1993). Exposure of epithelial cells to hypotonic medium (relative to the osmolarity of the cytoplasm) leads to cell swelling (Steltenkamp et al. 2006). Microvilli elongation is an ATP dependent process (Lange and Gartzke 2001) resulting in the uptake of salt and water from the cytoplasm, thus reduction in cell volume (figure 4.1.4).

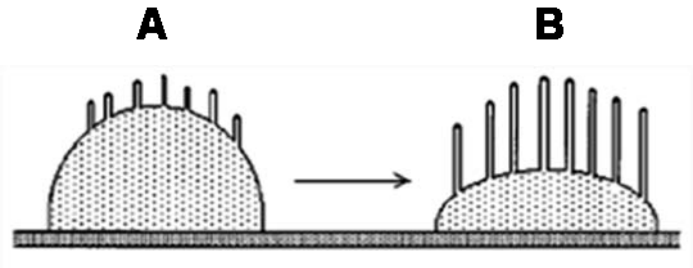

Figure 4.1.4: microvilli elongation (A) results in reduction (B) of cell volume (Lange and Gartzke 2001).

In order to investigate the effect of cell swelling on microvilli morphology, confluent cells were incubated with distilled water for 3 min and then were processed for AFM scanning. Figure 4.1.5 displays height images of cells that were fixated following swelling (A) and cells (B) that were fixated after incubation in PBS as a control. Microvilli are still visible from the height image of cells after swelling, although a clear difference in surface organization is seen between swollen and control cells. The fact that microvilli can still be resolved after swelling is related to the dehydration step during sample preparation. This step involves water extraction from the cells and volume reduction, thus exposing the microvilli on the cell surface. Microvilli are composed of parallel actin filaments with uniform polarity cross linked by actin binding proteins (Loomis et al. 2003). Therefore, *Phalloidin*-Alexa488 was used to label microvilli from confluent cells (figure 4.1.6).

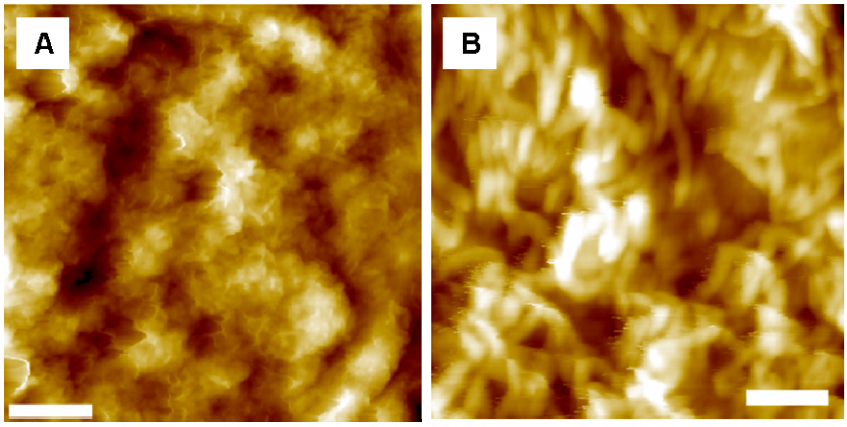

Figure 4.1.5: height image of microvilli following cell swelling. Scale bar is 2 µm. B: microvilli from a confluent cell monolayer without cell swelling. Scale bar is 1 µm.

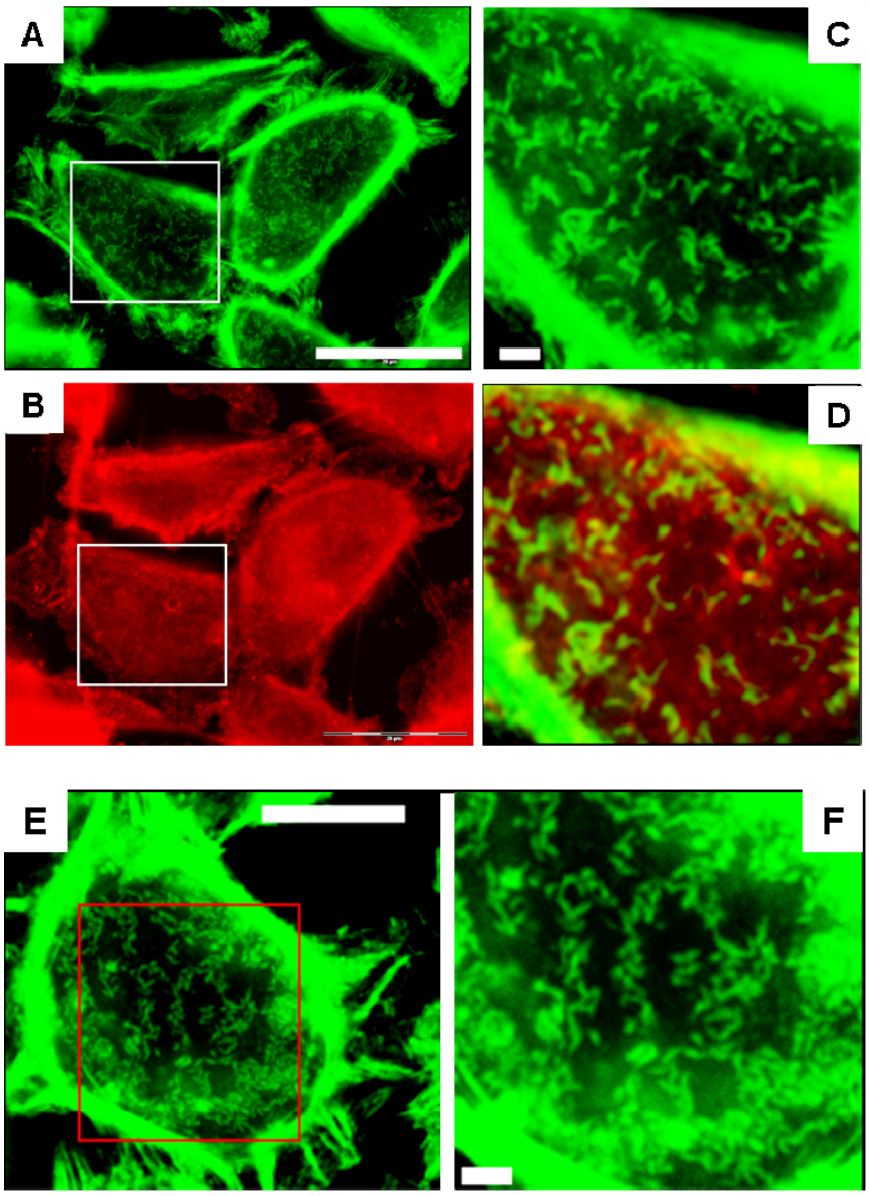

Figure 4.1.6: Fluorescence images of microvilli labeled with *Phalloidin*-Alexa488. A: Scale bar is 25 µm. B: The same cells from A were doubled labeled with DiI (lipid staining). C and D zoom in to the same area marked in A and B. Scale bar is 2 µm. E: Scale bar is 10 µm. F and

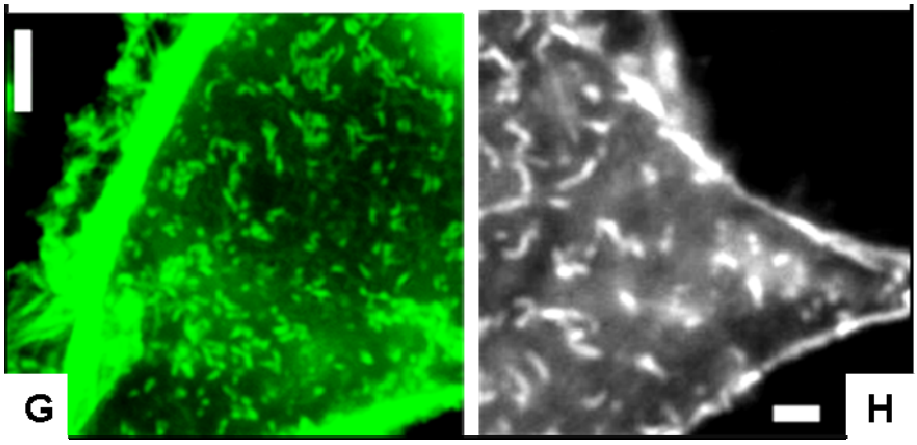

H: Scale bar is 2 µm. G: Scale bar is 4 µm.

The average microvilli length, $(377 \pm 112.1)\,nm$, is in the microscope's resolution range. However their thickness, about 60 nm, cannot be resolved. Therefore, it is suggested that the fluorescent apical membrane projections, that are clearly visible in the merge image (D) of DiI and F-actin labeling, reflect microvilli clusters. These projections are not related to the cells' primary cilia (figure 4.1.7A) out of two reasons: 1) each cell consists of only one primary cilium which is a few µm in length (Anderson et al. 2008). 2)

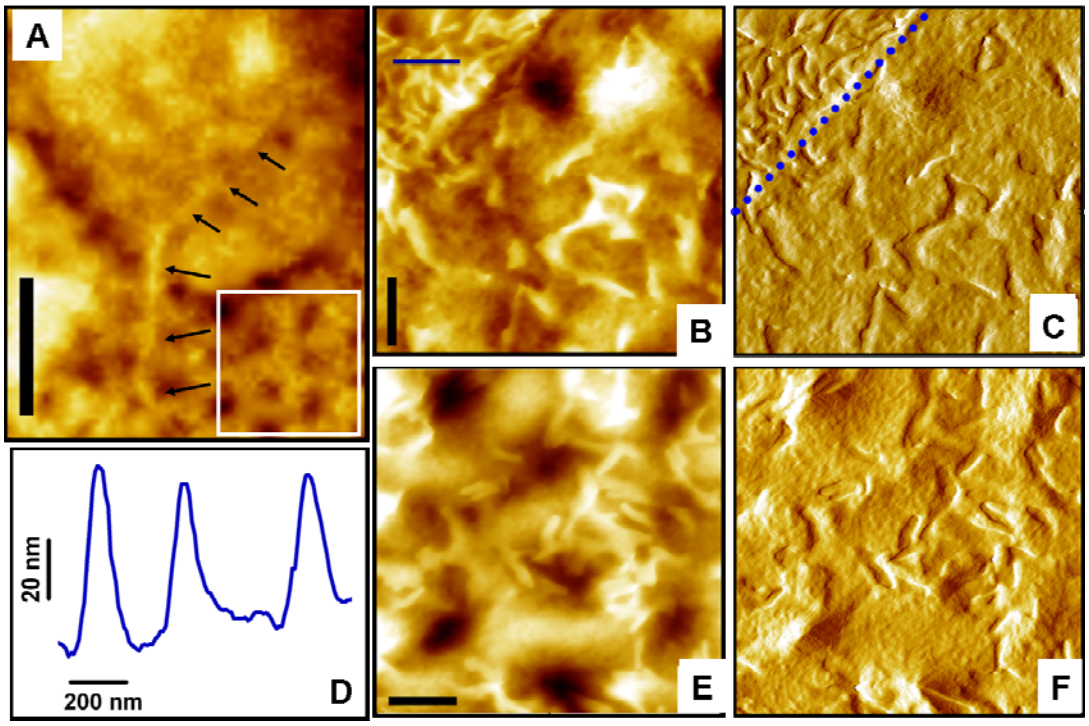

Figure 4.1.7: A: Height images of apical membrane microvilli at the border between the cell body and the cell edge. A: The black arrows point at a long protrusion, about 12 µm in length, which may be related to the primary cilium flattened on the apical cell surface. Scale bar is 5 µm. B and C are height and deflection images, respectively, showing the border between the cell body and the cell edge. Scale bar is 1 µm. D: Microvilli height profile refers to the blue cross line in B. E and F are height and deflection images, respectively, referring to the marked area in A.

The primary cilium consists of microtubules, thus it cannot be detected by *Phalloidin* labeling. Interestingly, microvilli were detected with epifluorescence microscope only from cells grown on the substrate's rim, although height images (figure 4.1.7) clealy reveal their expression from cells on the porous area.

4.6 Pulse force modulation

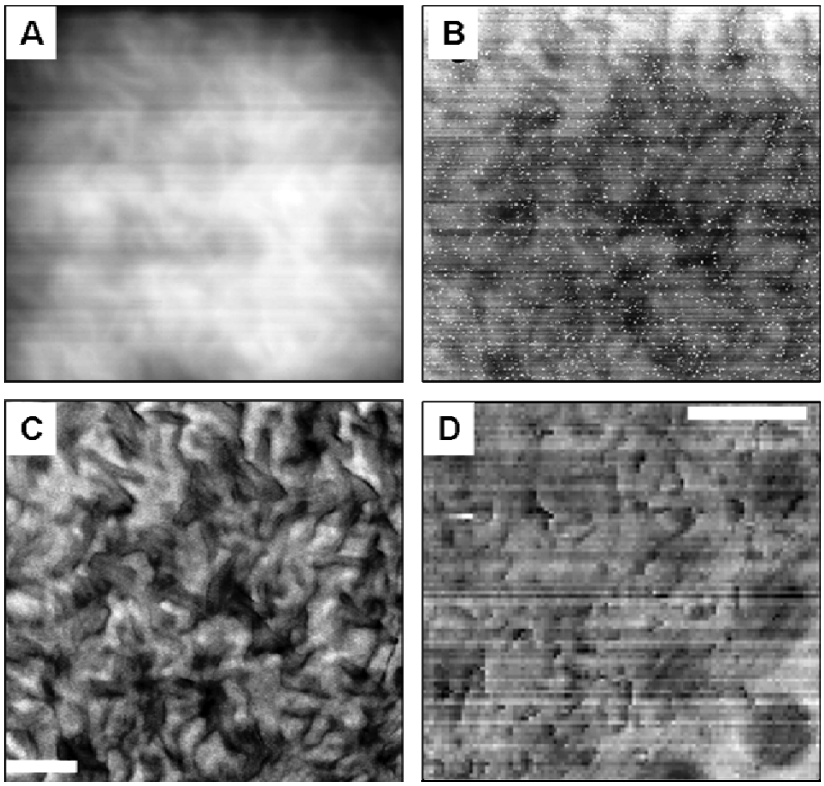

Figure 4.1.8: Height (A), adhesion (B) and stiffness (C) PFM maps of microvilli recorded from highly confluent cells. Scale bar is 1 μm. D: Adhesion map of the cell edge recorded from preconfluent cells. Pore diameter and scale bar are 3 μm.

In the pulsed force mode (PFM) imaging technique the cantilever is oscillated at a frequency smaller than its resonant frequency over the sample surface. Since the cantilever does not tough the surface constantly, such as in contact mode, lateral forces are reduced. The recorded images are based on pulse force mode curves generating height, adhesion and stiffness maps. Figure 4.1.7 displays images from the cell edge of fixated confluent (A-C) and preconfluent (D) cells. The stiffness and the adhesion based images reveal a dense meshwork of microvilli.

4.7 Conclusions

The advantages of using Si/SiO_2 porous substrates over flat non porous substrates for cell cultivation are: 1) biocompatibility 2) small size and defined geometry allowing better handling and the possibility to localize cells of interest both for fluorescence and AFM measurements. 3) Both the apical and the basolateral membranes are exposed to the same nutrient concentrations. 4) Porous substrates are cost effective since they can be sterilized and reused. 5) Cell cultivation and

manipulations, such as fluorescene labeling with expensive markers, are carried out in small liquid volume. 6) 1.2 µm and 2 µm diameter sized pores allow free indentation of thin cellular parts (< 1 µm), such as the cell edge by eliminating the effect of the underlying stiff substrate on the recorded elasticity. An estimated cell height of 8.5 µm was detected from a cell monolayer cultivated on pores by CLSM z sections. Height images superimposed with fluorescence images of the identical cells labeled with $DiIC_{18}$ (lipid), Phalloidin-Alexa488 (F-actin) and DAPI (nucleic acid labeling) enables to relate structure with mechanics. Microvilli and planar membrane domains were clearly resolved with AFM SEM and fluorescence images.

Microvilli elongation from: $(377 \pm 112.1)\,nm$ to $(549.2 \pm 91.6)\,nm$, recorded after 48h and 72h of cell cultivation, indicates complete cell polarization. Cells cultivated on the pores reveal lower distribution of actin stress fibers than those cultivated on the rim indicated by F-actin labeling with *Phalloidin*-alexa488. Force indentation curves, recorded from the nucleus region of cells on porous substrate at low forces, reveal a soft viscoelastic response with a Young's modulus of $(2.2 \pm 1.1)\,kPa$. The elasticity reported from the periphery close to the nucleus did not differ significantly.

5. LOCAL FORCE MAPPING OF APICAL MEMBRANES

5.1 Introduction

The elastic response of cell membranes is controlled by an elaborate interplay of the following factors: (1): mechanical properties of the lipid bilayer, represented by the lateral tension (σ), bending rigidity (κ), and area compressibiliyt (K_A). (2): membrane proteins and steroids. (3): the underlying F-actin meshwork (Evans and Yeung 1989, Oster 1989, Kidoaki et al. 1996). Since membrane deformation depends strongly on the underlying cytoskeleton (Rotsch and Radmacher, 2000, Zhang et al., 2002, Pourati et al., 1998, Wu et al., 1998), the motivation was to investigate this dependency without the interference from the cell body with its internal organelles, the osmotic pressure of the cell and the underlying substrate.

Free standing epithelial apical membranes, detached from a cell monolayer, were probed with an AFM in order to obtain physical properties as well as elasticity maps at nanometer length scales. Biocompatible porous substrate are mostly suitable to characterize the membrane mechanical properties by means of force indentation with an AFM (Gonçalves et al. 2006, Lorenz et al. 2009), since it allows free membrane indentation into the pores, excluding the interference of the underlying substrate. The first goal of the present investigation was to optimize a protocol that enables to transfer intact apical membrane fragments from a cell monolayer to a gold coated porous substrate. In the second part, apical membrane fragments were characterized both with fluorescence microscopy, SEM and AFM imaging technique in order to prove functionality and to resolve surface structures. In the third part, force indentation measurements with native chemically modifies membranes were performed in order to elucidate for the first time the elastic response from isolated MDCK II epithelial apical membranes.

5.2 Preparation of apical membranes on porous substrate and rim

The goal of the preparation step was to transfer intact apical membrane sheets from confluent MDCK II cells to a porous substrate. In order to detach the membranes from the cells, Si/SiO_2 chips with 1.2 μm and 2 μm size pores were coated with 60 nm of thermally evaporated gold (Steltenkamp et al. 2006). In order to enhance electrostatic contact between the pores' rim and the membranes, the chips were coated with 1 mg/ml poly-D-lysine for 10 min and then were placed on the top of swollen cells (Danelon et al. 2006). Cell swelling was achieved by incubating the cell monolayer with distilled water for 3 min (Perez et al. 2006). The chips with the attached apical membrane sheets were gently removed off the cell monolayer after 20 min of incubation. As directly transferred from the cells, the membrane sheets consist of the endogenous lipid and protein composition. To demonstrate the membrane integrity (figure 5.0), F-actin (C) and lipid fluorescent markers (A-B) were used. Defined membrane borders were clearly detected by F-actin labeling with *Phalloidin*-Alexa546, indicating that actin microfilaments are still connected to the cytoplasmic side of the membranes. In general, these membrane borders enclosed membrane covered pores that exhibited low intensity of fluorescence emission. Localization, required to identify the identical membrane fragments for AFM

measurements, was possible due to the well defined geometry of the chip. F-actin labeling with *Phalloidin*-Alexa488 was found to be more reliable than DiI (lipid staining) to localize membrane fragments due to the poor solubility of DiI in PBS, leading to aggregate formation. Large cellular parts were identified by their relative high fluorescence intensity detected from different focus planes, whereas membrane fragments exhibited low fluorescence intensity and no fluorescence was reported out of the focus plane. In order to remove large cellular parts from membrane fragments, shear stress was applied with PBS buffer jets injected from a syringe (Ziegler et al 1998). This step was controlled with a phase contrast optical microscope. As the fluorescence intensity of membrane fragments was quickly reduced over time, low lamp intensity and fast acquisition time were used to capture an image display with an intesified CCD camera (Olympus).

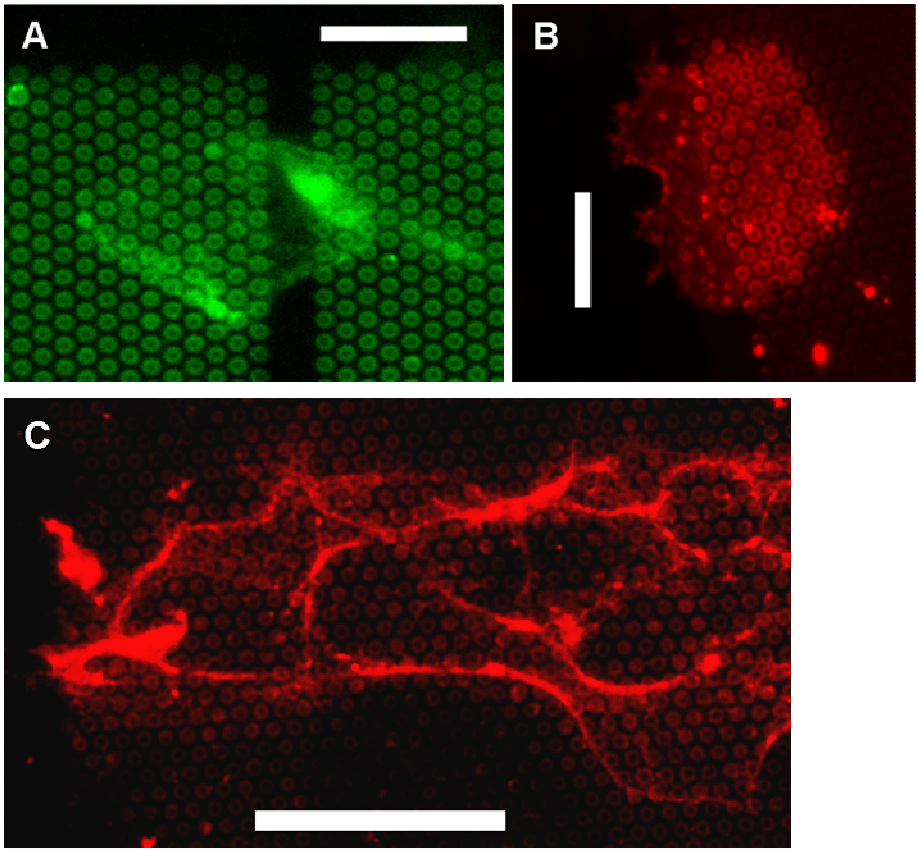

Figure 5.0.: Fluorescence images of free standing apical membranes detected with epifluorescence microscope. A: Lipid labeling with PKH2. Scale bar is 10µm. B: Lipid labeling with DiI. Scale bar is 10 µm. C: F-actin was labeled with *Phalloidin*-Alexa546. Scale bar is 25 µm.

Sharp fluorescence images of a DiI labeled apical membranes were acquired (Figure 5.3) with CLSM due to the high signal to noise ratio. The origin of the small intensified fluorescence spots is related to the hydrophobic sites of the dye molecules which tend to form small crystals in hydrophilic solutions (Colarusso and Kenneth 2001).

In general, the preparation of apical membranes on a non porous substrate, such as a flat Si/SiO_2, (figure 5.1) resulted in higher density of membrane sheets owing to the higher coverage of poly D lysine coating the substrate used to detach the membranes.

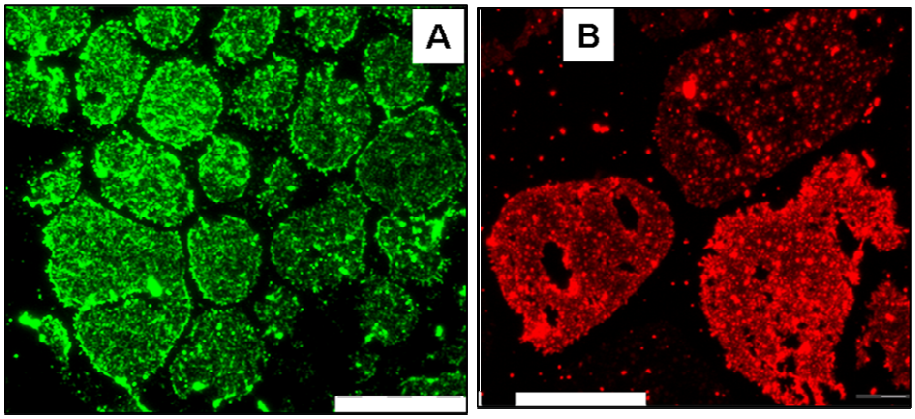

Figure 5.1.: Apical membrane fragments supported on flat gold coated Si/SiO_2 substrate. A: F-actin labeling with *Phaloidin*-Alexa488. B & D: Lipid labeling with $DiI(C_{18})$. Scale bar is 20 µm.

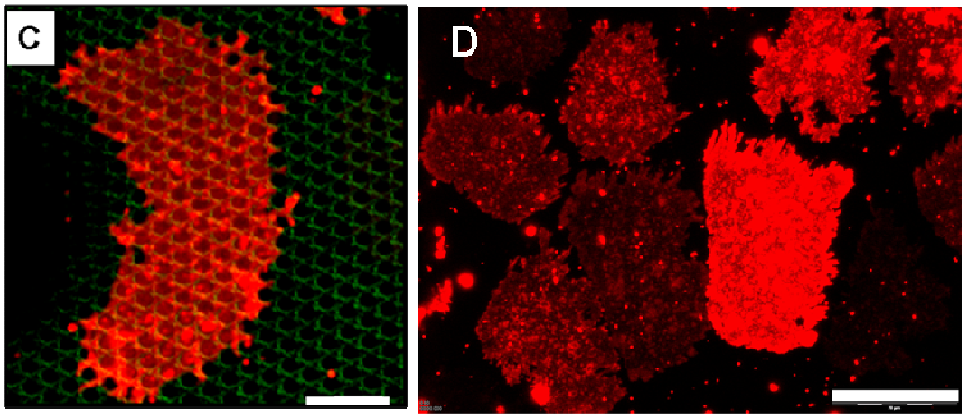

C: Fluorescence image recorded with CLSM of lipid labeled ($DiIC_{18}$) apical membrane on porous substrate. Scale bar is 5 µm.

5.3 Apical membrane topography with AFM

A successful preparation of apical membrane fragments imaged both with an AFM and an epifluorescence microscope is shown in figure5.2. F-actin labeling with *Phalloidin*-Alexa488 (A) was used to localize free standing membrane (pore size: 2µm) for AFM imaging (C). Height images were scanned at minimal forces (contact mode: < 300 pN) in order to reduce membrane compression, resulting in underestimation of the membrane height (Weisenhorn et al. 1993, Müller et al. 1998, Lorenz et al. 2009). Height images of the identical membrane fragment, scanned at low (I) and high (J) forces, indicate that at high force imaging the membrane is pushed into the pores. Superposition (B) of height image with the matching fluorescence image displays an increased topography as well as a higher fluorescence intensity of F-actin at the membrane borders. To insure that the pores are membrane covered, height profiles were routinely taken on the recorded height image (C). The marked cross line refers to the height profile shown in D. It reveals a clear difference in indentation depth between empty (1: 700 nm) and covered pores (2-3: 200 nm) at the same scanning force. The thickness of the membrane was estimated with height profile recorded in empty and covered rims. In general, the prepared apical membrane fragments do not contain residual cytoplasmic content such as

cell nuclei. The height of the membranes was deermined to be around 50 nm in good accord with that reported for MDCK II basolateral membranes (Lorenz et al. 2009, Ziegler et al. 1998).

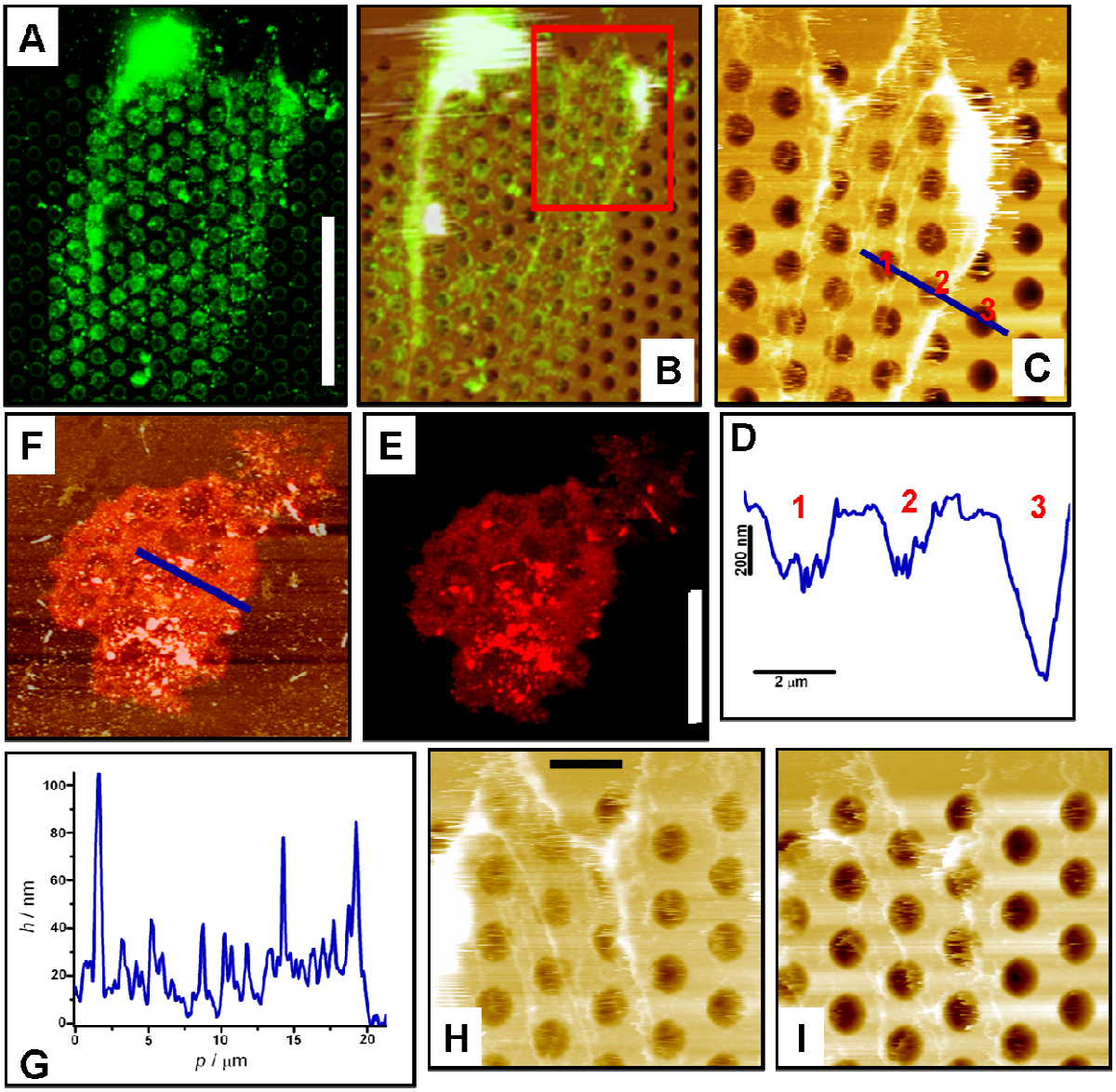

Figure 5.2.: Successful preparation of apical membrane fragments imaged with AFM and epifluorescence microscope. A: F-actin labeling of free standing apical membrane, suspended across 2 µm diameter size pores, with *Phalloidin*-Alexa488. Scale bar is 20 µm. B: corresponding height image superimposed with A. The marked area refers to the height image shown in C. D: height profile refers to the cross line in C. E: apical membrane fragment supported on a rim and labeled with DiI. Scale bar is 20 µm. F: Merge of fluorescence and height. The cross line relates to the height profile shown in G. Sequential height images of the membrane fragment shown in C scanned at minimal (H) and high (I) forces. Scale bar is 3 µm.

Apical membrane thickness of 7 nm was previously reported by using the same preparation technique (Frank et al. 2006) on glass. Figure 5.2E shows an apical membrane fragment that was prepared on flat Si/SiO_2 support and labeled with DiI. AFM Height superimposed with the fluorescence image (G) reveals an average height of 30 nm (H), indicating the impact of the used substrate (flat/porous) on the membrane preparation.

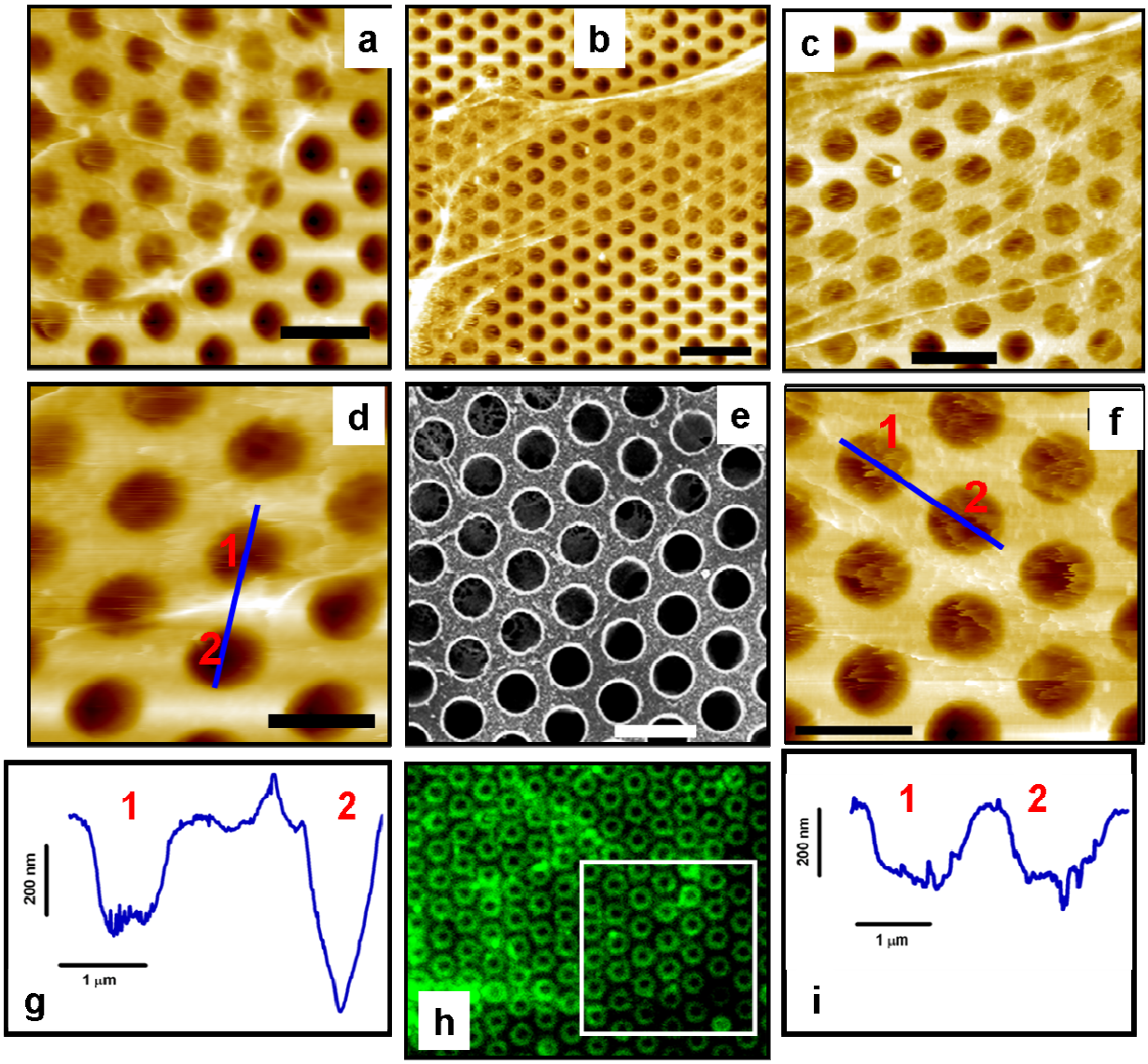

Figure 5.3: AFM height images and SEM of apical membranes fixated with glutardialdehyde. a: scale bar is 2 µm. b: scale bar is 5 µm. c: scale bar is 3 µm. d-f: scale bar is 2 µm. g-i: height profiles refer to the cross lines marked in d and f, respectively. h: the same apical membrane fragment seen in a and e was labeled with *Phalloidin*-Alexa488.

In general, imaging of native membranes in PBS revealed no membrane structures due to a high degree of softness and deformability contributing to low resolution (Hoh and Schoenberg 1994, Weisenhorn et al. 1993, Butt et al.1990). In order to resolve membrane structures, native apical membrane fragments were fixated with glutardialdehyde and imaged at different length scales (figure 5.3). During chemical fixation aldehyde functional groups bind to lysine groups, which leads to the formation of protein cross links, increasing both the membrane stiffness and the Young's modulus (Butt et al. 2005). AFM height images following fixation (a-d, f) reveal microfilaments attached to the membrane. The SEM image (e) displays the same membrane fragment shown in a, revealing membrane rupture across the pores. This is related to the SEM measurement conditions, including vacuum and an electron beam damaging the membrane (Braet et al. 1998). Height profiles across the

pores (g and h) refer to the membrane fragments shown in d and f, respectively. In comparison to pore-spanning basolateral fragments prepared by the squirting lysing protocol (Lorenz et al. 2009, Ziegler et al. 1998), only a limited number of microfilaments still attached to the pore covering apical membranes were visualized.

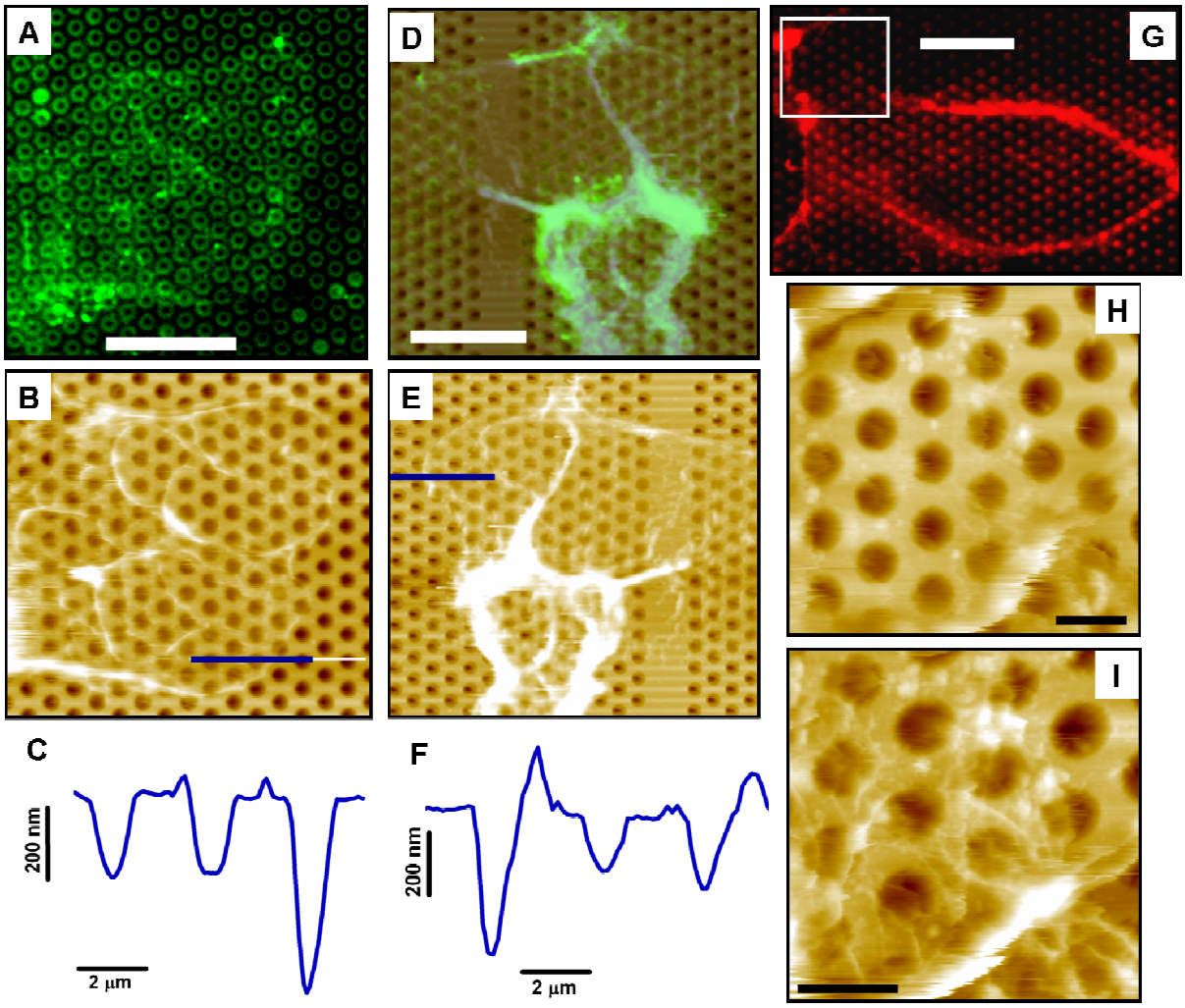

Figure 5.4: Native and glutardialdehyde fixated apical membrane sheets. A: fixated apical membrane labeled with *Phalloidin*-alexa488. Scale bar is 10 µm. B: the matching height image. The cross line refers to the height profile in C. D: Merge of fluorescence (*Phalloidin*-alexa488) and height of native membrane. Scale bar is 10 µm. The cross line in the height image (E) relates to the height profile in F. G: apical membrane labeled with *Phalloidin*-alexa546. Scale bar is 10 µm. The marked area was scanned with AFM before (H) and after (I) fixation with 2% glutardialdehyde for 15 min. Scale bar is 2 µm.

To investigate the effect of protein cross linking on the membrane topography, Figure 5.4 shows height images of fixated (B) and native (E) apical membrane sheets with the corresponding fluorescence images, A and D, respectively. An Overlay (D) of height and fluorescence images after Labeling with *Phalloidin*-Alexa488 shows heterogenous distribution of F-actin attached to the cytoplasmic side of the membrane. Height images of the identical membrane fragment before (H) and after fixation with 1% glutardialdehyde (I) reveal microfilamets which could not be resolevd in the native membrane fragment. In general, elasticity measurements with AFM were carried out in

membrane areas where low intensity of F-actin was detected. However, it was not possible to obtain with this preparation technique membrane fragments that are totally devoid of microfilaments.

SEM images of apical membrane fragments (figure 5.5) did not reveal dense distribution of microvilli attached to the membrane which is explained by cell swelling during the preparation (Sukhorukov et al. 1993).

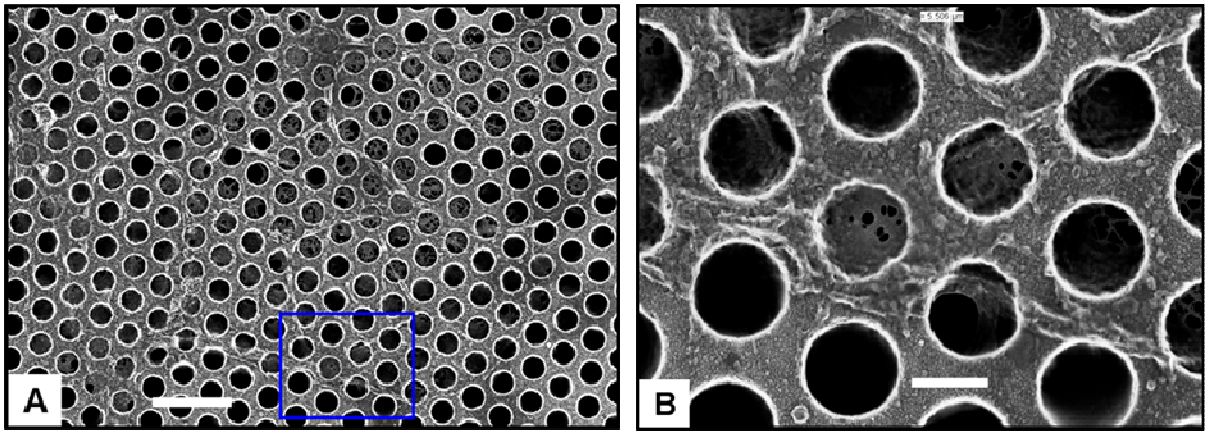

Figure 5.5.: SEM images of apical membrane fragments. Pore diameter: 1.2 µm. A: Scale bar is 4 µm. B refers to the blue marked area in A. Scale bar is 1 µm.

5.4 Force imaging effect

To demonstrate the membrane elastic response, three sequential height images of the same apical membrane fragment (figure 5.6) were obtained at maximal loading forces of 0.8 nN (B), 2.4 nN (C), and 0.8 nN (D). The height profiles (E) refer to the black lines marked on the height images. Maximal indentation depths of 100 nm and 200 nm were recorded from pore numbers 1 and 2, respectively, at loading force of 0.8 nN. As the force was increased by a factor of three to 2.4 nN, the indentation depth was doubled, accordingly, to 200 nm and 400 nm. The height profile, recorded by imaging the same membrane area again with 0.8 nN, indicates that the membrane readjusted its shape in the time course of imaging due to its elastic properties. Importantly, no membrane rupture events were observed. In addition, the difference in indentation depth between pore 1 and pore 2 demonstrates the membrane heterogeneity as different membrane domains exhibit different elasticity response. Area dilatation (stretching) of lipid bilayers does not permit relative area changes ($\Delta A/A_0$) larger than 5% (Boal 2002). In order to explain large membrane area changes without membrane rupture, it is inferred that the membrane is not bound tightly to the poly-D-lysine coated rim and therefore there is no edge restriction. Membranes behave as two dimensional liquid (Evans 1974) as they develop no resistance to in-plane shear. This allows a free flow of material from the adjacent rims, serving as reservoir, into the pores when more force is applied. It also indicates that the lateral tension, $\sigma = K_A\left(\Delta A / A_0\right)$, applied on the membrane during indentation is kept constant. This observation is

in good agreement with large surface extension reported with MDCK II basolateral membranes supported on porous substrate without poly-D-lysine coating (Lorenz et al. 2009).

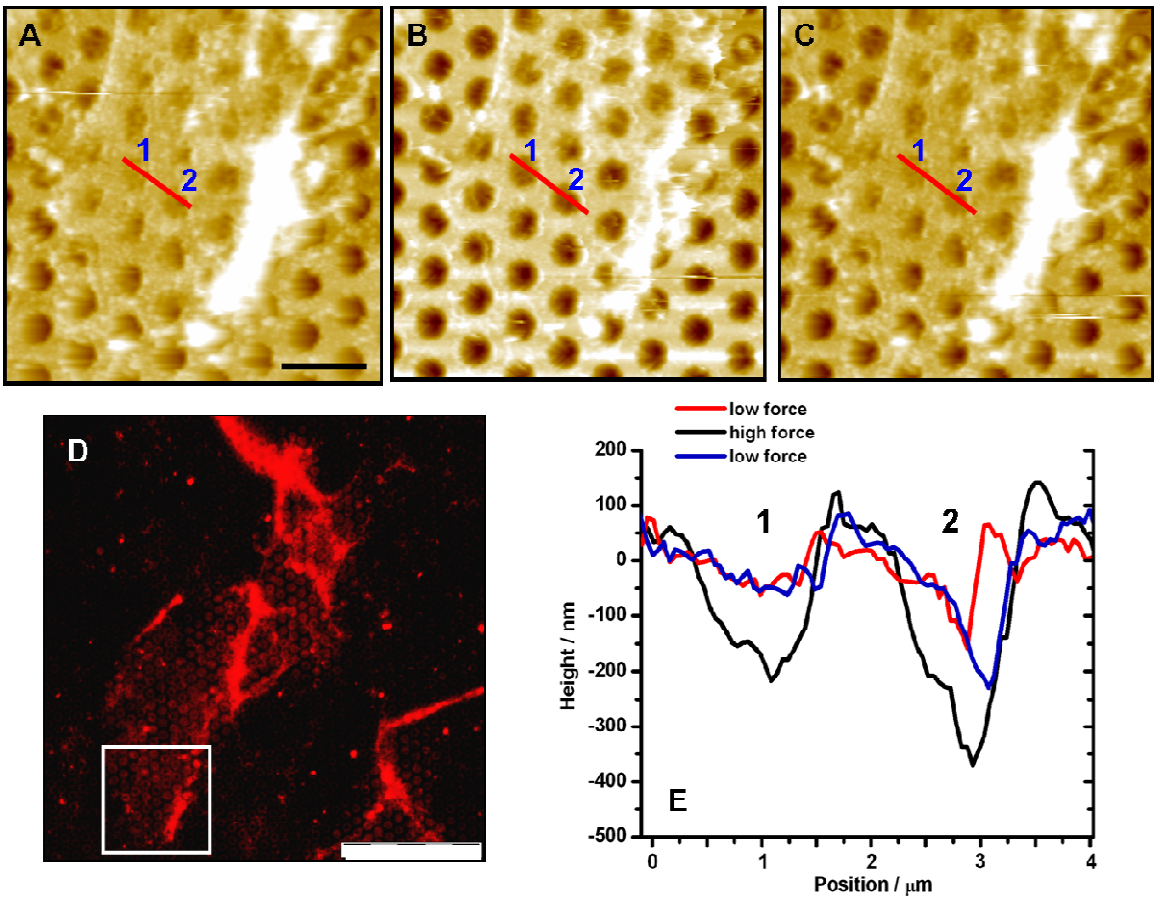

Figure 5.6.: Sequential height images of apical membrane fragment imaged at 0.8 nN (A), 2.4 nN (B) and 0.8 nN (C). Scale bar is 4 µm. D: Matching fluorescence image as F-actin was labeled with *Phalloidin*-Alexa546. Scale bar is 20 µm. E: Height profiles from the same position marked in A-C.

5.5 Force indentation curves of isolated apical membranes

The approaching curve of a force indentation curve, recorded on free standing cell membranes, contains the information about the membrane mechanical properties (Gonçalves et al. 2006 , Lorenz et al. 2009). Figure 5.7A illustrates an axis symmetric indentation at the centre of a membrane covered pore with a cone shaped tip. Since the ratio R_{pore} / R_{tip} is very small, a point contact indentation is assumed leading to a cone membrane shape across the pore. H represents the indentation depth and F is the force applied by the tip. As the cantilever approaches the membrane surface, it is deflected due to the surface interaction forces. A typical force indentation curve reported from membrane covered pore (red) and membrane covered rim (blue) is shown in B. This curve can be divided into three parts demonstrated by the cantilever position relative to the membrane. (1): non-contact regime. (2): contact regime starting with the "snap on". (3): cantilever retraction leading to a "snap off". The force curve recorded from a covered pore shows low resistance to indentation in

comparison to that from the rim, reporting a maximal indentation depth of 500 nm at a maximal loading force of 0.8 nN. The elastic response of a membrane covered pore reveals a non linear curve shape. However, a linear elastic regime was found close to the zero contact point up to 100 nm of indentation depth in average. In the linear regime the ratio between the applied loading force and the indentation depth is linear. Non linear elastic response is related to indentation depth greater than 100 nm and accordingly higher forces. The blue line (C) indicates a linear regime observed over the first 100 nm of indentation from the tip-membrane contact point. According to this linearity, an apparent membrane spring constant was defined $k_{app} = -(dF/dh)_{p=0}$ at the centre of the pore (Lorenz et al. 2009, Seltenkamp et al. 2006) as the slope of a linear fit (C). In this example, a linear regime over 200 nm of indentation was observed, reporting a correlation coefficient of $R^2 = 0.95$. The membrane spring constant (k_{app}) calculated from the first 100 nm of indentation is 0.5 *mN/ m*.

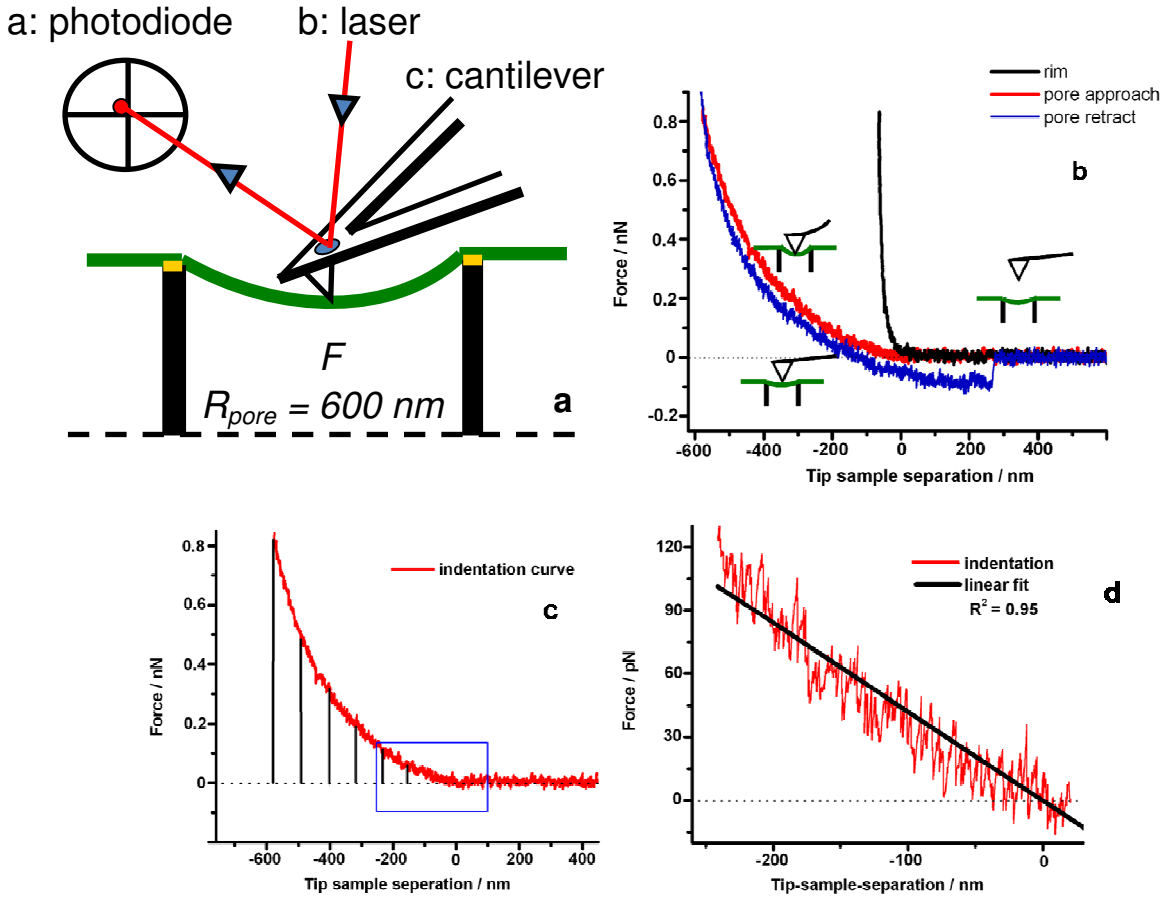

Figure 5.7: A: Schematic of free standing apical membrane (green line) indented at the center of a pore with an axis symmetric geometry. The membrane is suspended across 1.2µm size pores, F represents the applied force and h is the indentation depth. The gold stripe on the pore rim illustrates the gold coating on the Si/SiO_2 substrate. Since the ratio R_{pore}/R_{tip} is small (600nm/20nm), it is justified to assume a point force load indentation. C: Typical force indentation curves of free standing native apical membrane in PBS. B: The integrated area under the approaching curve bordered by the base line (F = 0) refers to the work ($1.4 \cdot 10^{-16}$J) done by the cantilever on the membrane during indentation. The blue line indicates the linear regime over the first 200 nm of indentation used for linear regression (D). The correlation coefficient obtained was $R^2 = 0.95$.

During force indentation work is done on the membrane by the cantilever tip. The integrated area under the approaching (loading) curve (C), representing this work, indicates the maximal energy stored in the membrane during indentation (Butt et al. 2005). This energy, calculated as $1.4 \cdot 10^{-16}$J, is transferred into elastic strains within the membrane, whereas part of it is released as heat. The area under the retracting (unloading) curve, bordered by the baseline F = 0, represents the work done by the membrane ($1.1 \cdot 10^{-16}$J) as it recovers to its initial shape in an elastic manner. The gap between the approaching and the retracting curves ($0.3 \cdot 10^{-16}$J) is the dissipated energy loss due to the lag phase between the cantilever deflection and the vertical movement of the piezo scanner (A-Hassen et al., 1998, Hoh and Engel 1993). Energy loss during indentation (hysteresis) is an indication of a viscoelastic response, originating from the following friction forces: 1) membrane-cantilever contact. 2) Membrane- rim contacts. It depends on the cantilever speed and the membrane viscosity (Alcaraz et al., 2002, Mathur et al., 2001, Zelenskaya et al. 2005).

In order to estimate the change in hysteresis following different treatments, the calculated hysteresis was normalized (Mathur et al., 2001, Zelenskaya et al. 2005, Xu and Shau 2008) to the work done during indentation (the area under the approaching curve). The normalized hysteresis calculated for native membranes out of five representing force curves was 0.49 ± 0.05 (figure 5.8A), which is smaller (0.57 ± 0.04) than that caculated from the nucleus region of living MDCK II cells.

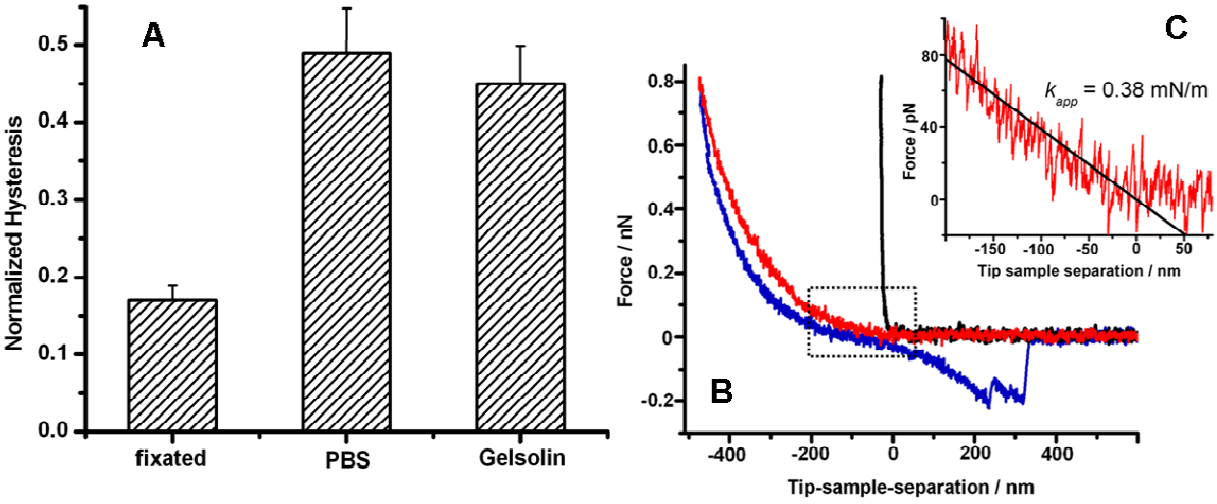

Figure 5.8: A: Normalized hysteresis values were calculated for different chemical treatments. The normalized hysteresis was calculated as the ratio of the integrated area (J) enclosed between the approaching and the retracting curves at the contact regime to the integrated area under the approaching curve bordered by the baseline (F = 0). Each column represents the average value from 5 different force curves. B: Typical force indentation curve recorded from native apical membrane suspended across 1.2 µm pores, reporting a normalized hysteresis of 42.7%. C: The membrane stiffness: 0.38 mN/m was calculated over the first 150 nm of indentation.

To investigate the effect of the maximal loading force on the membrane elastic response, force indentation curve were recorded at increasing forces. Membrane deformation at maximal force of 1.6

nN (A-B), 8 nN (C-D) and 16 nN (E-F) were recorded from the same membrane covered pore (Figure 5.9) by changing the deflection trigger point values.

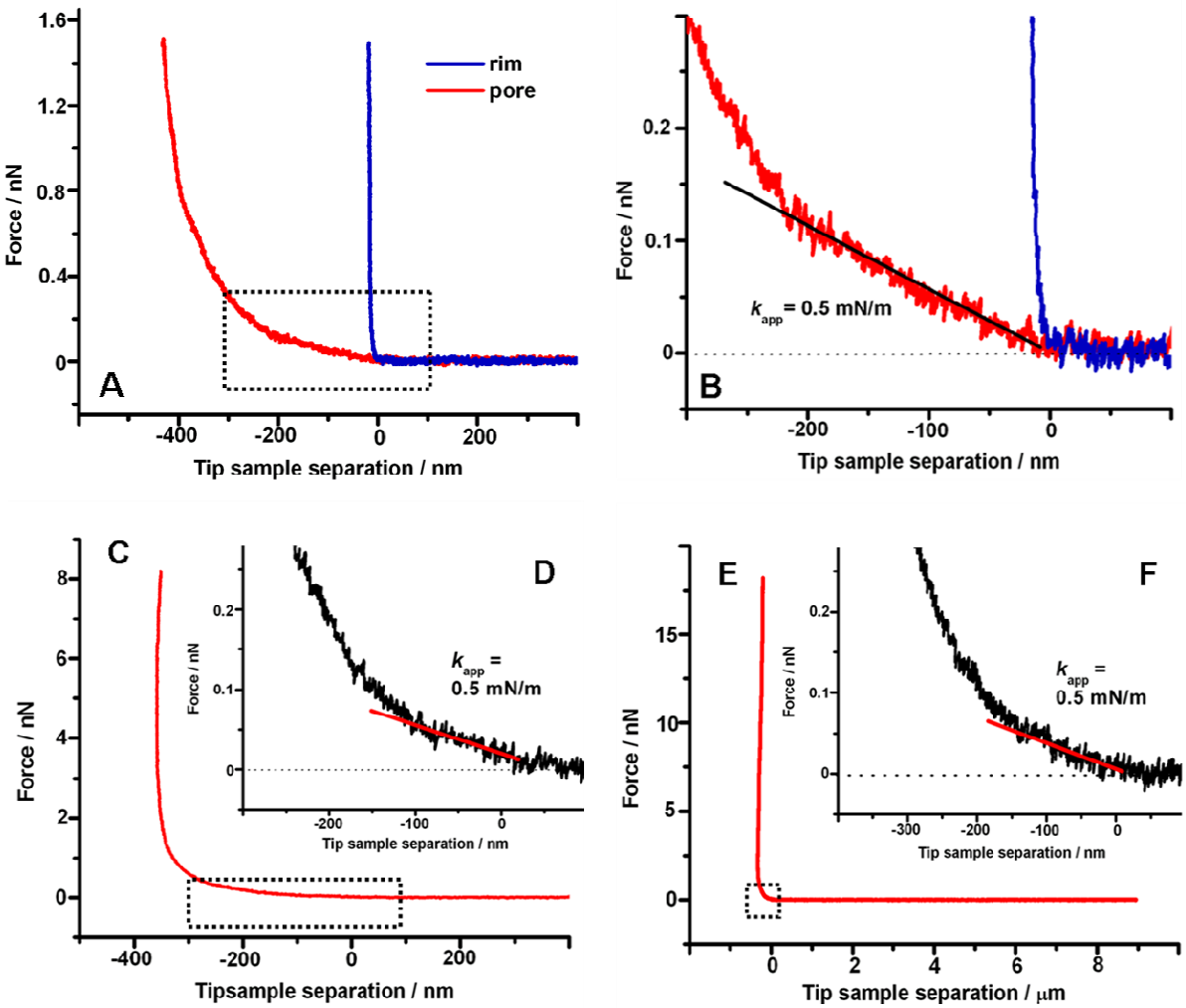

Figure 5.9: Force indentation curves recorded from the same pore at different maximal forces. A: 1.6 nN. C: 8 nN. E: 16 nN. The dotted squares refer to the matching linear regimes used to calculate the stiffness slope (k_{app}) over the first 100 nm of indentation by a linear fit (B, D, F).

The shape of the approaching curve at a maximal force of 1.6 nN (A) reveals soft deformation response with low resistance to force indentation. Figure 5.9B reveals a linear regime over the first 200 nm of indentation. A stiffness slope of 0.5 *mN/m* was calculated over the first 100 nm of indentation. Membrane deformation at higher forces reveals the same elastic response with the same stiffness value. Amazingly, no membrane rupture was reported at high forces, suggesting a complete elastic response without irreversible membrane deformation. This finding confirms the existence of membrane reservoir which is used to buffer variations in membrane tension. In addition, it indicates, the contribution of underlying F-actin to the restoring forces. Actin filaments are considered as semiflexible bendable rods with a persistence length ranging from 2µm to18µm (Satcher and Dewey 1986, Janmey 1996). Dpending if membrane material is supplied from the rim (material reservoir), these properties allow F-actin to resist high level of stress

Figure 5.1.0 shows a fluorescence image of F-actin labeled membrane (A) wit hthematching height image (B). Force indentation curves were taken from intact (C) and ruptured membrane covered pores (E-F) refering to the same membrane fragment (B). The indentation curve, reported from an intact covered pore (C), shows a continuous elastic response over the whole indentation depth with a membrane spring constant of 0.2 *mN/m* (D). Discontinuity with membrane indentation is related to membrane rupture (Mey et al. 2009), so called: "breakthrough event". Following a rupture event, indicated by the black arrows (E), the tip hits a stiff part of the pore edge, thus a hard repulsion is reported. A sequential indentation curve (F), recorded from the same pore, reveals that the elastic response is retained for the first 200 nm of indentation followed by two rupture events. This indicates that the first rupture event, shown in E, is partial as part of the membrane is still intact.

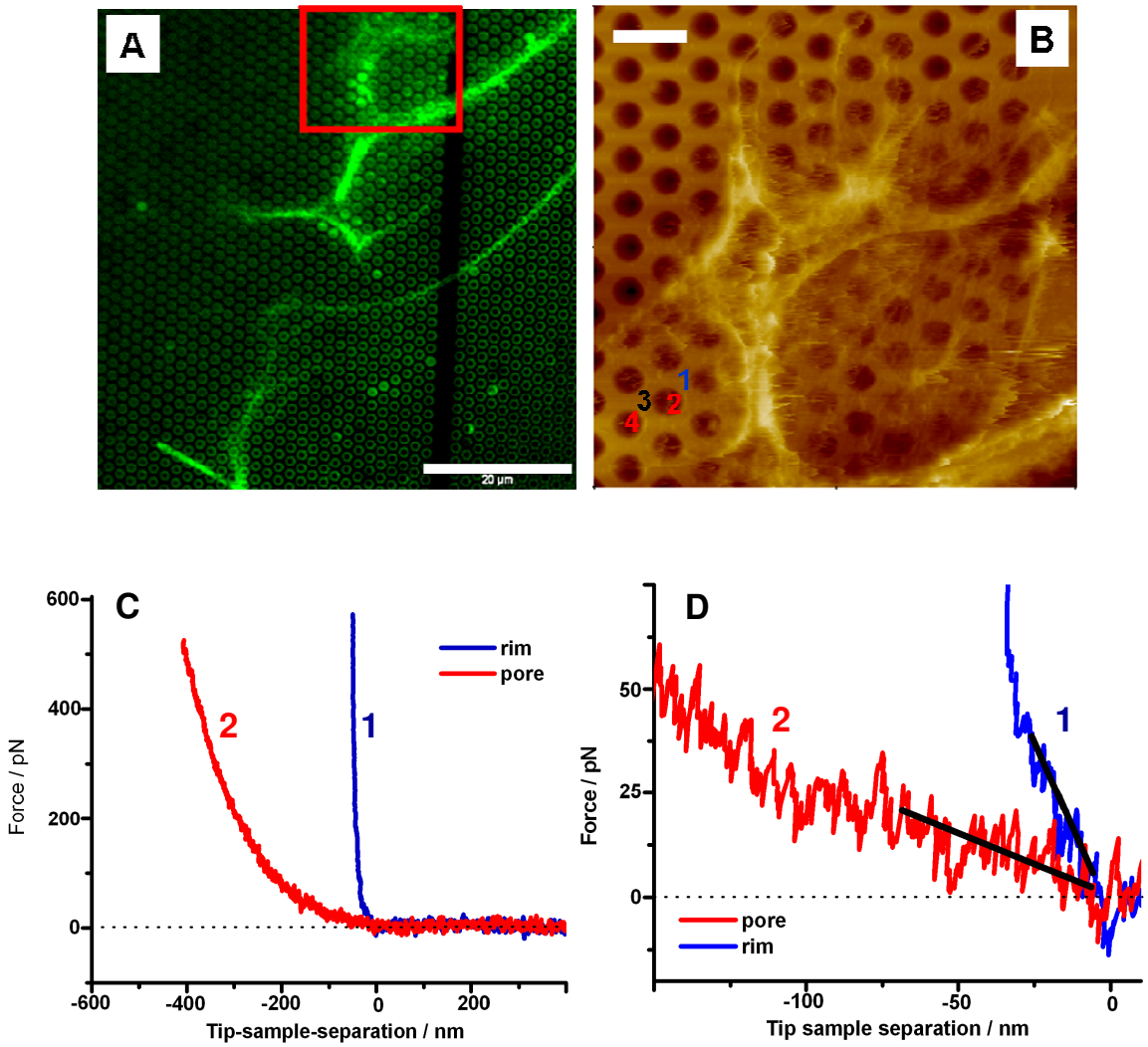

Figure 5.1.0: Force indentation curves taken from free standing apical membrane marked in the fluorescence image (A) and the corresponding height (B). Scale bars are 20 µm and 3 µm, respectively. The numbers in the height image (B) refer to the force indentation curves (C, E, F) from pores and adjacent rims. D: Zoom in to the linear regime of curve C showing the difference in the elastic response between a rim and a pore covered membrane.

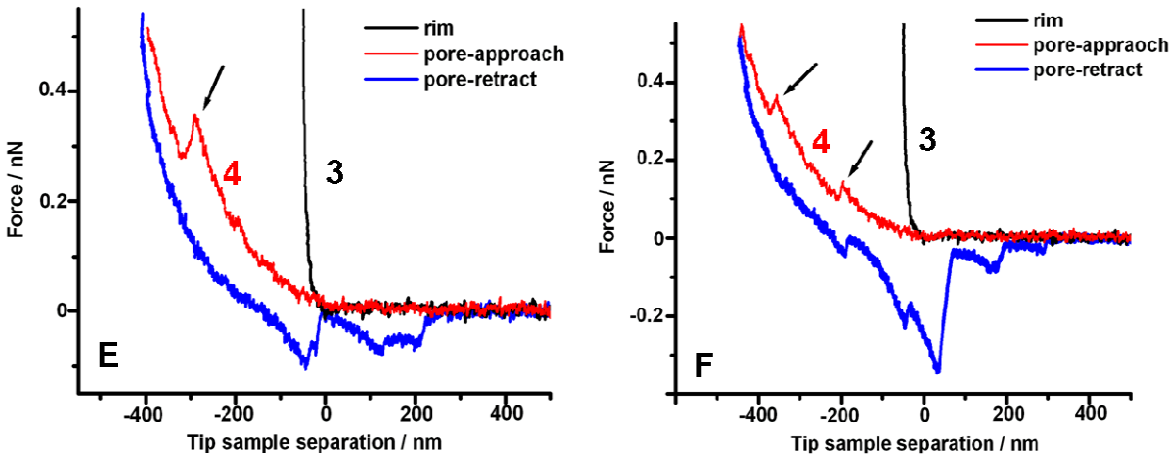

Partial membrane ruptures (breakthrough events) shown in E and F refer to sequential force indentation curves recorded from the same pore.

Figure 5.1.1 shows force indentation curves recorded from the height image (A) following protein crosslinking with 2% glutardialdehyde. Average membrane spring constant values: (0.56 ± 0.3) *mN/m* and (1.97 ± 0.8) *mN/m* (table 1) were calculated from native and GDA fixated membranes, respectively, indicating a clear shift in the membrane stiffness (figure 5.1.2).

In addition, the gap phase between the piezo movement and the cantilever deflection is reduced, reflected by a significantly decreased hysteresis between the approaching and the retracting curves.

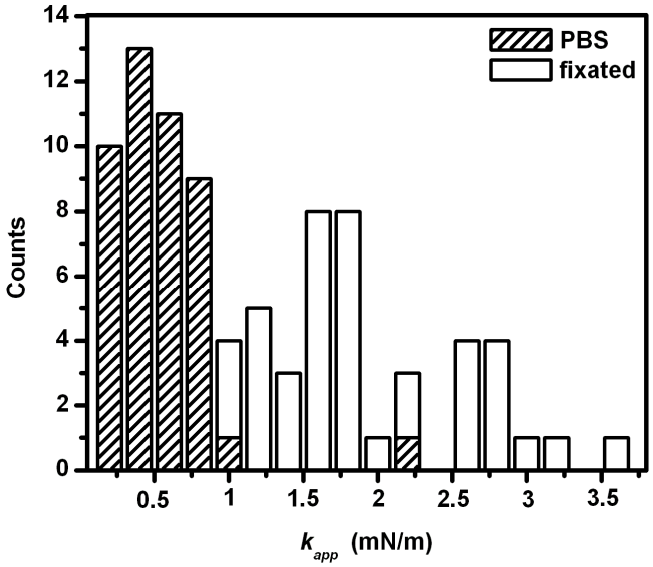

Figure 5.1.2: Histogram of the membrane apparent spring constant (k_{app}) of native apical membrane before (gray column) and after fixation with glutardialdehyde (white column).

In living cells, viscoelasticity is mainly contributed by F-actin (Satcher and Dewey 1986, Janmey 1996). Apical membrane fixation with GDA reported a reduction of 66% of the observed hysteresis in comparison to that recorded from native membranes (figure 5.8).

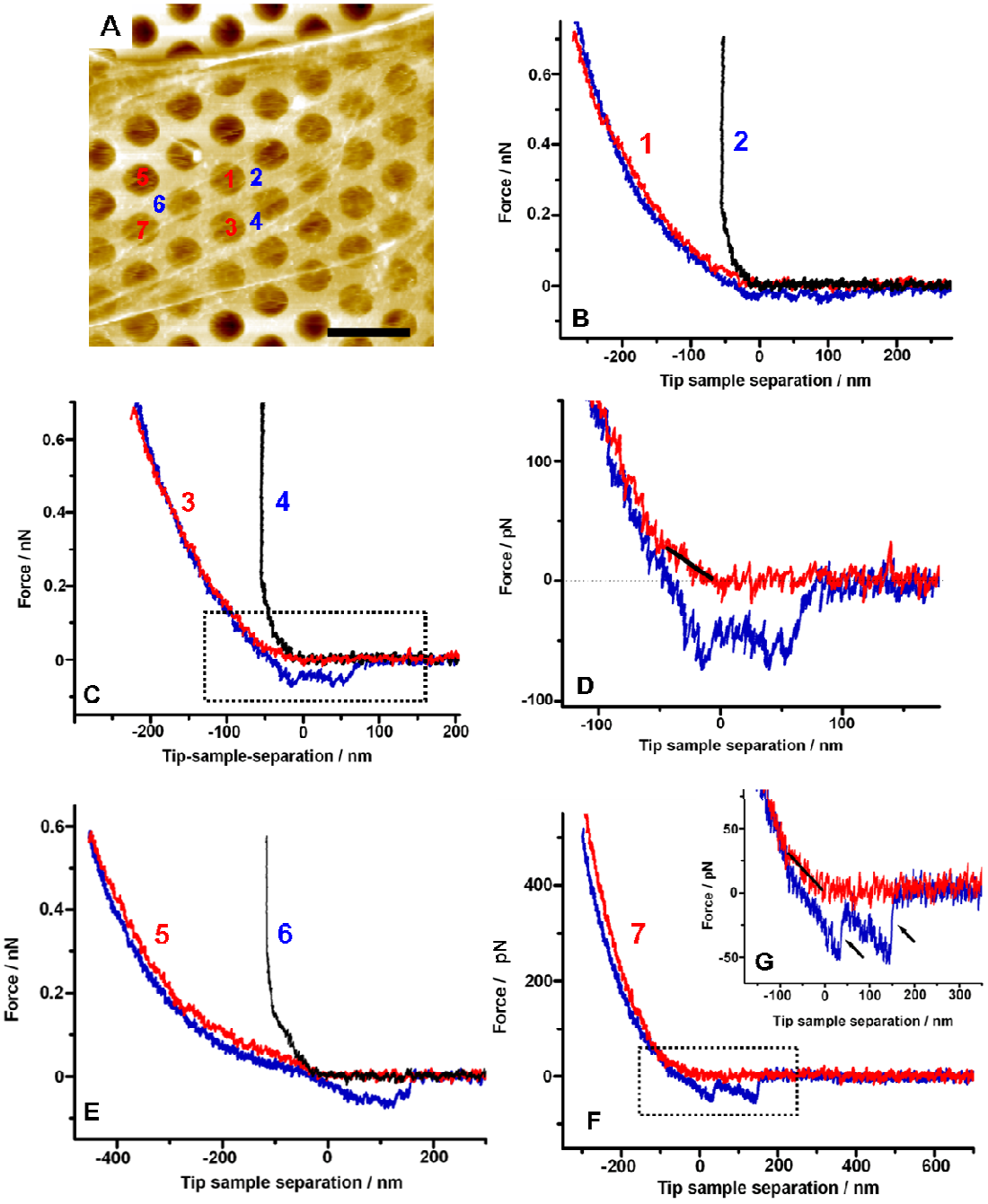

Figure 5.1.1: A: AFM height image of apical membrane fragment following fixation with glutardialdehyde. Scale bar is 3 µm. Collection of force indentation curves (B-G) reported from pores and rims (red is the approaching curve and blue is the retracting curve from a pore and black is the approaching from a rim). The numbers of the curves refer to the point marked on the height image. D and G relate to the linear regime of membrane indentation in C and F, respectively. The arrows in F indicate unbinding of membrane tethers during retraction.

5.6 F-actin depolymerization

F-actin exhibits gel-sol transformation due to the presence of F-actin cross linkers, such as ABP (Actin Binding Protein) and filamin (Yin and Stossel 1979). To investigate the effect of F-actin depolymerization on the stiffness recorded from apical fragments, two types of actin disrupters were used: Gelsolin and DNAse I. Gelsolin is a calcium dependent capping protein and its interaction with

F-actin leads to the formation of cuts in the polymer cross linking points. This results in an increase of the number of filaments which effectively lower the ratio cross-link/ polymer, thus causing dissolution of F-actin. This mechanism is in good agreement with the theory of polymer gels, claiming that small changes in the cross-linker/ polymer ratio close to a critical point lead to gel-sol transformation. DNAse I treatment leads to F-actin depolymerization due to its strong binding constant ($K_D = 1.9 \cdot 10^{-9}$) to the pointed end of F-actin (Podolski and Steck 1988), thus inducing a structural change (Hitchcock 1976). Figure 5.1.3 shows typical force indentation curves recorded following treatment with 20 µg/ml plasma gelsolin. Both curves: A and B exhibit low resistance to membrane indentation reporting k_{app} values of 0.1 *mN/m* and 0.5 *mN/m*, respectively. The k_{app} histogram, referring to force indentation curves measured after gelsolin treatment (figure 5.1.4), reveals a wide distribution from 0.1-0.95 mN/m. The average k_{app} (0.39±0.2) *mN/m* (table 1) is about the same order as that of untreated native membranes. The average k_{app} following DNAse I trearment is also in the same range: (0.43 ± 0.2) *mN/m* (figure 5.1.5). Therefore, it is suggested that F-actin depolymerization has little or no effect on the linear membrane response recorded at low forces. Fluorescence investigation of the same membrane fragment, which was labeled with *Phalloidin*-Alexa546, shows a clear reduction in the fluorescence intensity after gelsolin treatment. This result supports a previous investigation of ventral membranes prepared from fibroblast cells and treated with the same concentration of gelsolin (Hirata et al. 2005). Figure 5.1.5 shows force indentation curves before and after gelsolin treatment recorded from the same pore. These curves show no difference in the k_{app} values. However at higher forces a clear difference with the curve shape is observed. The indentation curve, reported following gelsolin treatment, exhibits lower resistance to membrane deformation than that taken bedore treatment at the same force, suggesting that the effect of gelsolin treatment is detectable in the nonlinear regime of the curve which reflects stretching. In addition, the normalized hysteresis: 0.45 ± 0.049 , is not significantly different than that calculated from untreated membranes in PBS (figure 5.8). This suggests that there is no change in the viscoelasticity before and after treatment.

The slip between the membrane and the cytoskeleton is the most dominant contributor (Marcus and Hochmuth, 2002) to the effective membrane surface viscosity (η_{eff}). In addition, previous reports have shown that cells treated with F-actin disrupters exhibited lower effective membrane viscosity (Marcus and Hochmuth, 2002, Sun et al. 2007). Drag forces between the cantilever and the membrane are also related to the sample viscosity (Alcaraz et al. 2002). Therefore, it would be expected that the normalized hysteresis would decrease following F-actin depolymerization. No change in the membrane hysteresis suggests that actin filaments are still bound to the membrane.

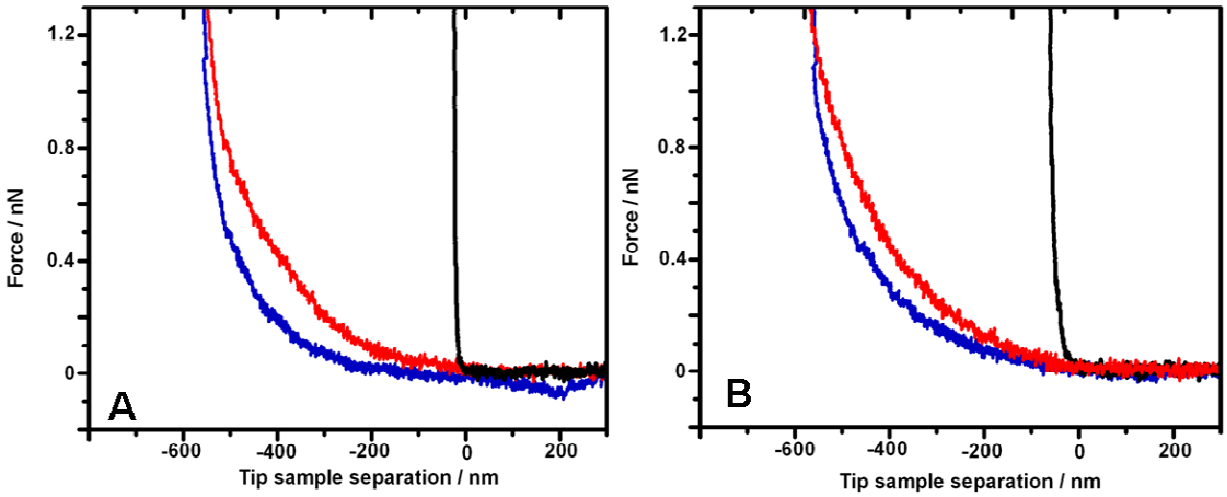

Figure 5.1.3: Force indentation curves were recorded from an apical membrane fragment incubated with 20 *µg/ml* gelsolin. The k_{app} values calculated from A and B are 0.1 *mN/m* and 0.5 *mN/m*, respectively.

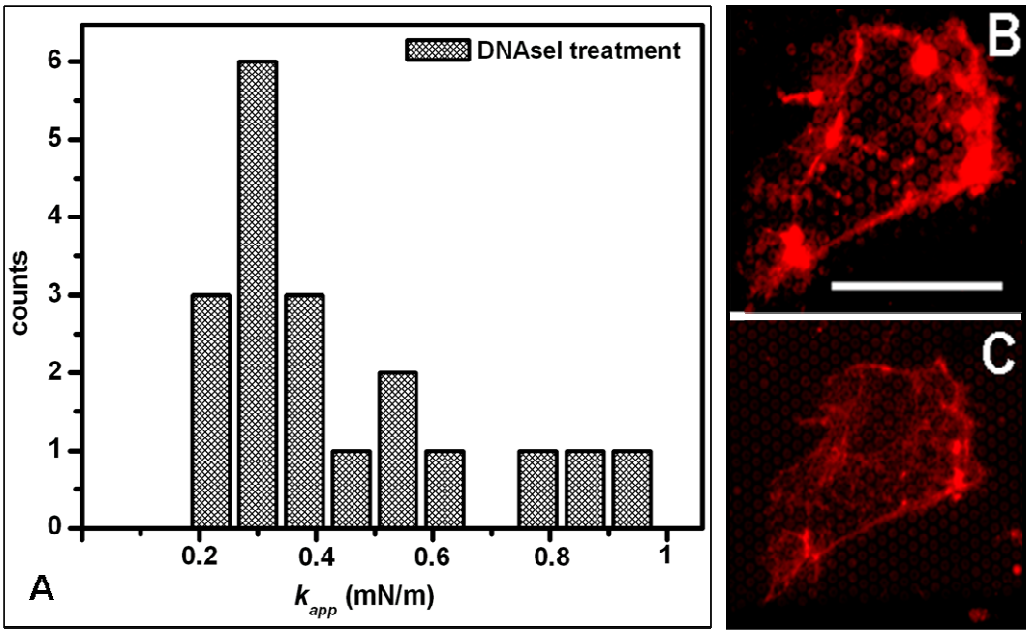

Figure 5.1.4: A: Histogram of the membrane apparent spring constant (k_{app}) following DNAse I treatment, reporting an average value of (0.43±0.2) *mN/*m. Fluorescence images recorded following F-actin labeling with *Phalloidin*-Alexa546 before (B) and after (C) DNAse I treatment at the same lamp intensity and camera exposure time. Scale bar is 20µm.

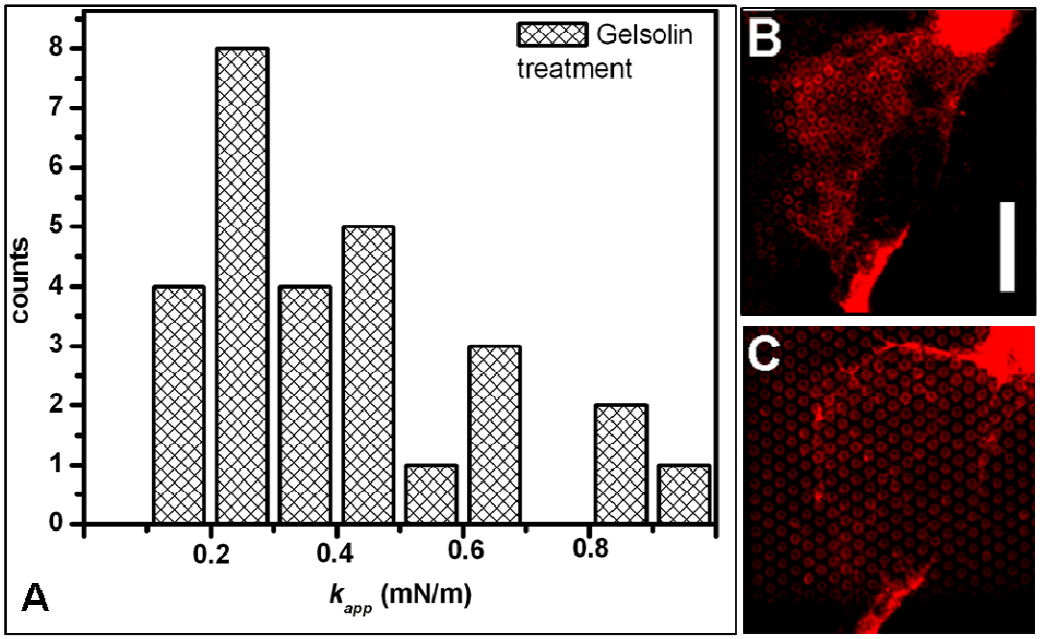

Figure 5.1.5: Histogram of the membrane apparent spring constant (k_{app}) following gelsolin treatment, reporting an average value of (0.39±0.2) *mN/m*. Fluorescence images recorded after F-actin labeling with *Phalloidin*-Alexa546 before (B) and after (C) gelsolin treatment at the same lamp intensity and camera exposure time. Scale bar is 10µm.

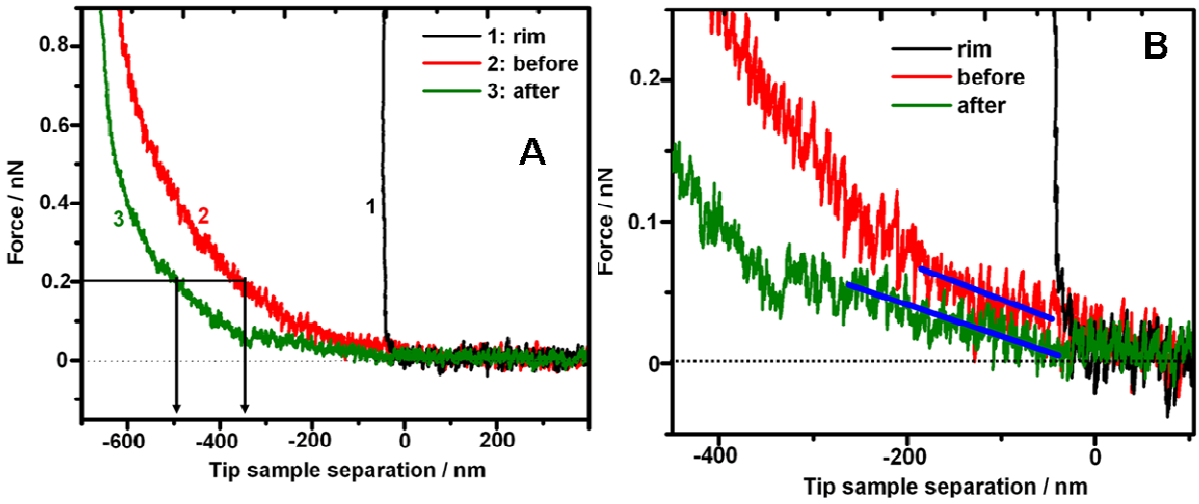

Figure 5.1.6: A: Comparison between force indentation curves recorded from the same pore before (red) and after (green) gelsolin treatment, showing no difference (B) in the k_{app} value (0.1 mN/m) of the initial slope. Significant difference between the curves is visible in the nonlinear part at higher forces reflecting membrane stretching.

5.7 Cholesterol extraction

Cholesterol is a major component of the membrane lipid bilayer (Yeagle 1985), contributing to its permeability, elasticity (Evans and Needham 1998), ordering degree (Stockton and Smith 1978) and fluidity (Xu and London 2000). Elevation of the cholesterol level in lipid bilayers results in a higher order degree of lipids thus decreased entropy. Cholesterol depletion leads to reduced lateral mobility of membrane proteins (Kwik et al. 2003). Together with PIP_2 and sphingolipids, cholesterol is also

one of the components of lipid rafts (Simons and Ikonen 1997, Brown and London, 2000, Eiddin 2003). Previous studies have shown that elevation of cholesterol in artificial lipid bilayers increased the membrane stiffness whereas cholesterol depletion decreased the membrane stiffness (Lundbaek et al. 1996, Evans and Needham 1987, Needham and Nunn 1990). However, recent studies with living adherent aortic endothelial cells taking also into account the underlying cytoskeleton have shown the opposite effect. Elasticity experiments performed with micropipette aspiration (Byfield et al. 2004) and AFM tether pulling experiments (Sun et al. 2007) reported that cholesterol depletion resulted in higher elastic modulus values thus higher stiffness, whereas cholesterol enrichments had no effect at all on the membrane stiffness. To investigate the effect of cholesterol on the elastic response of apical membranes, force indentation measurements were performed on the same membrane fragment before and after cholesterol extraction. In this case apical membrane fragmants were first measured in native conditions (PBS) and then were incubated with 20 µM cyclodextrin dissolved in PBS for 30 min. Force indentation curves were recorded again from the same fragment in order to compare the change in stiffness from the same pores. Figure 5.1.7 shows that cholesterol depletion resulted in membrane stiffening since the indentation slopes, k_{app}, over the first 100 nm of deformation increase by 2 and 5 fold, respectively.

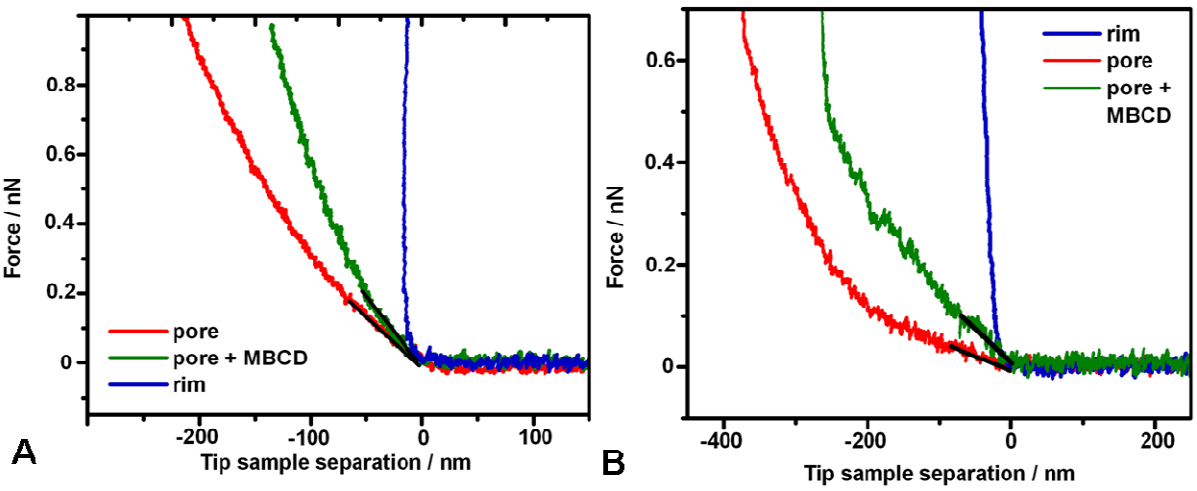

Figure 5.1.7: Force indentation recorded from the same pores before (red curves) and after (green curve) cholesterol extraction with 20µm MBCD.

The histogram in Figure 5.1.8 shows the stiffness distribution (k_{app}) recorded from the overall force indentation curves after cholesterol depletion. The average value of k_{app}: (2.1 ± 1.3) *mN/m* suggests the cholesterol depletion has the same effect as that of protein cross linking on the membrane stiffness. The increase in membrane stiffness following cholesterol depletion from living endothelail cells was related to the increase in the adhesion energy between the membrane and the underlying cytoskeleton (Sun et al. 2007). Cholesterol extraction from living MDCK II cells resulted in cell detachment. Therefore, it was not possible to prepare apical membrane fragments from MBCD treated cells or to measure the cells' elasticity following this treatment.

Although, the exact mechanism of membrane stiffening following treatment with cyclodextin is unkonwn, it was previously suggested that cholesterol depletion from the cell membrane increases the stability of actin filaments by decreasing the level of PIP_2. This leads to the formation of stronger interactions between the membrane and the underlying cytoskeleton (Kwik et al. 2003, Raucher et al. 2001). The increase in the stability of F-actin is also related to the reduction in lateral diffusion of transmembrane proteins observed following cholesterol extraction (Kwik et al. 2003).

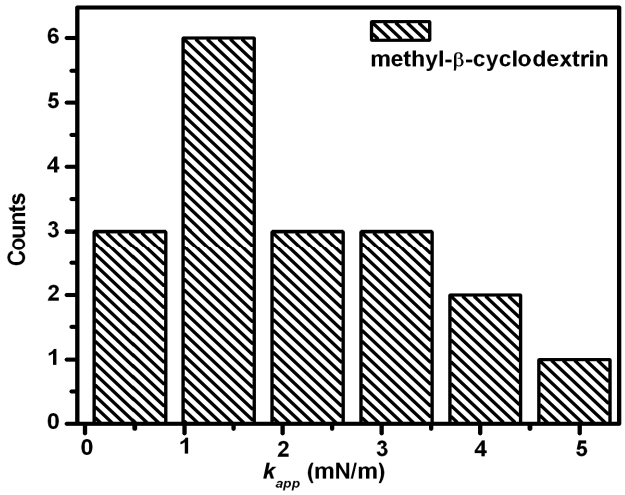

Figure 5.1.8: Histogram of the membrane apparent spring constant (k_{app}) following cholesterol extraction, reporting an average value of (2.1±1.3) *mN/m*.

In comparison to native membranes, protein crosslinking with PFA and GDA as well as cholesterol extraction with MBCD resulted in membrane stiffening. Removal of F-actin was not detectable within the linear regime of membrane indentation, but at higher forces relating to the non-linear regime.

Treatment	**Biological effect**	K_{app} / *mN/m*
PBS	physiological buffer	0.56 ± 0.3
PFA	protein cross linking	1.45 ± 0.9
GDA	protein cross linking	1.97 ± 0.8
DNAseI	F-actin disrupter	0.43 ± 0.2
Gelsolin	F-actin disrupter	0.39 ± 0.2
MBCD	cholesterol extraction	2.1 ± 1.3

Table 1: Summary of averaged k_{app} values calculated as a linear regression over the first 100 nm of indentation of native and chemically treated apical membranes.

5.8 Force mapping

Local force mapping is mostly suitable for characterizing the elastic response of free standing native membranes due to the membrane heterogeneity (Norouzi et al. 2006, Lorenz et al. 2009). Figure 5.1.9 shows AFM (A) and fluorescence (B) images of 4% PFA fixated membranes. The borders of the membranes are clearly defined by thick layers of F-actin, enclosing membrane covered pores h. These pores were used as a matrix to locally map the elastic response. Elasticity Maps were obtained by site specific force indentation measurements from a maximum scan size of 15x15 µm. In order to avoid thermal drift thus high forces, the setpoint was routinely zeroed between two sequential indentation measurements. To confirm correlation between the topographic domains and the occurrence of *Phalloidin* Alexa546 labeled actin filaments, both images were superimposed in an overlay image (C). A collection of force indentation curves (G-J) were recorded in the centre of the pores (red curves) as well as on the adjacent pore rims, (blue curves).

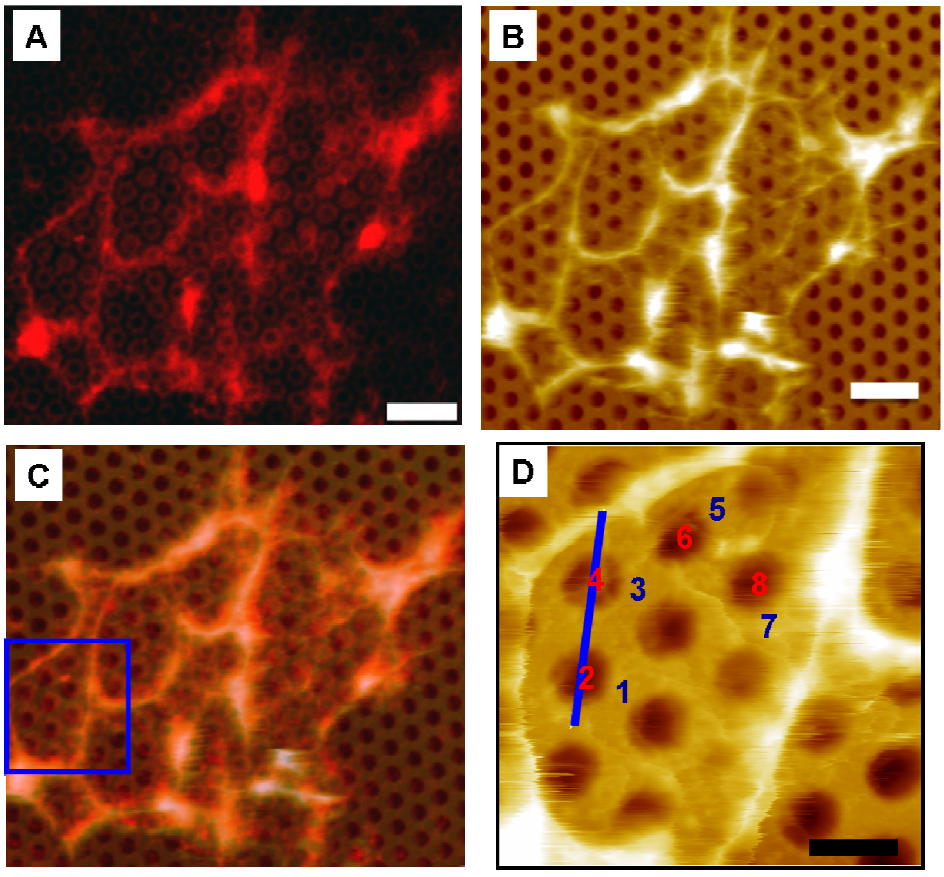

Figure 5.1.9: Apical membrane mapping. AFM height image (A) and the corresponding fluorescence image recorded by F-actin labeling with *Phalloidin*-alexa546. Scale bar is 6 µm. C: Merge of A and B. D: Zoom in to the selected force mapping area. The numbers indicate where the force indentation curves (F-I) were recorded. Scale bar is 2 µm.

The difference between covered pores (G-I) and an empty pore (J) is revealed with the shape of the indentation curve. In the latter case (J), the tip "falls" into the pore until it hits the edge, resulting in hard repulsion. In contrast, apical membrane fragments display extremely soft response if indented in

the centre of the pore. Notably, the mechanical response of the membrane fragments is strongly dependent on the location emphasizing the heterogeneous elastic nature of the cell membrane, which we attribute to differences in the Young's modulus and thickness of the membrane. The difference in the membrane stiffness: 1.3 mN/m and 2.4 mN/m recorded from force indentation curves 2 and 4, respectively, is correlated to the height profile (E) indicating a two fold higher indentation depth from pore 2.

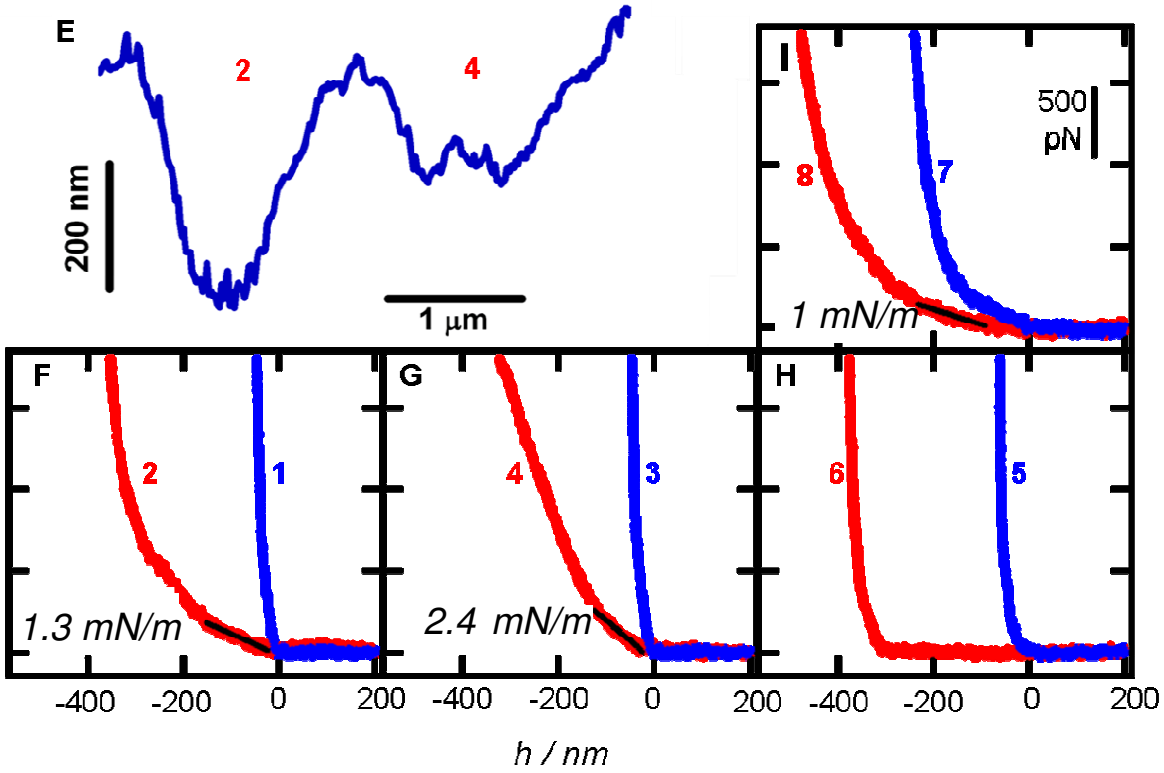

E: Height profile recorded over and referred to the pore numbers: 2 and 4, demonstrating different indentation depths. F-I: Force indentation curves recorded from the height image in D. The blue curves were taken on the pore rims, while the red indentation curves originate from the centre of the pores. The black lines are linear regression curves to determine the apparent spring constant k_{app} of the cell membrane.

In order to investigate whether there is correlation between the density of F-actin filaments and the stiffness of the membrane, an overlay (figure 5.2.0A1) of AFM and fluorescence images displaying *Phalloidin* Alexa488 labeled F-actin were generated and the obtained membrane's spring constant were plotted as a function of fluorescence intensity (A2). This plot shows a clear correlation between fluorescence intensity and k_{app}. It is expected that fixation/cross linking of proteins with glutardialdehyde (GDA) considerably impacts the stiffness of the membrane as observed for basolateral (Lorenz et al. 2009). To prove this, force indentation curves (B-G) were taken on individual membrane covered pores before (red) and after fixation with GDA (black). The blue force distance curves were taken from the adjacent pore rims. Obviously, the stiffness of the membrane increases substantially after fixation with GDA. Native apical membranes (non-fixated) reported a

mean stiffness, k_{app} = (0.56± 0.3) *mN/m*, in very good agreement with apparent spring constants found for non-fixated basolateral membranes: k_{app} = (0.8± 0.4) *mN/m*.

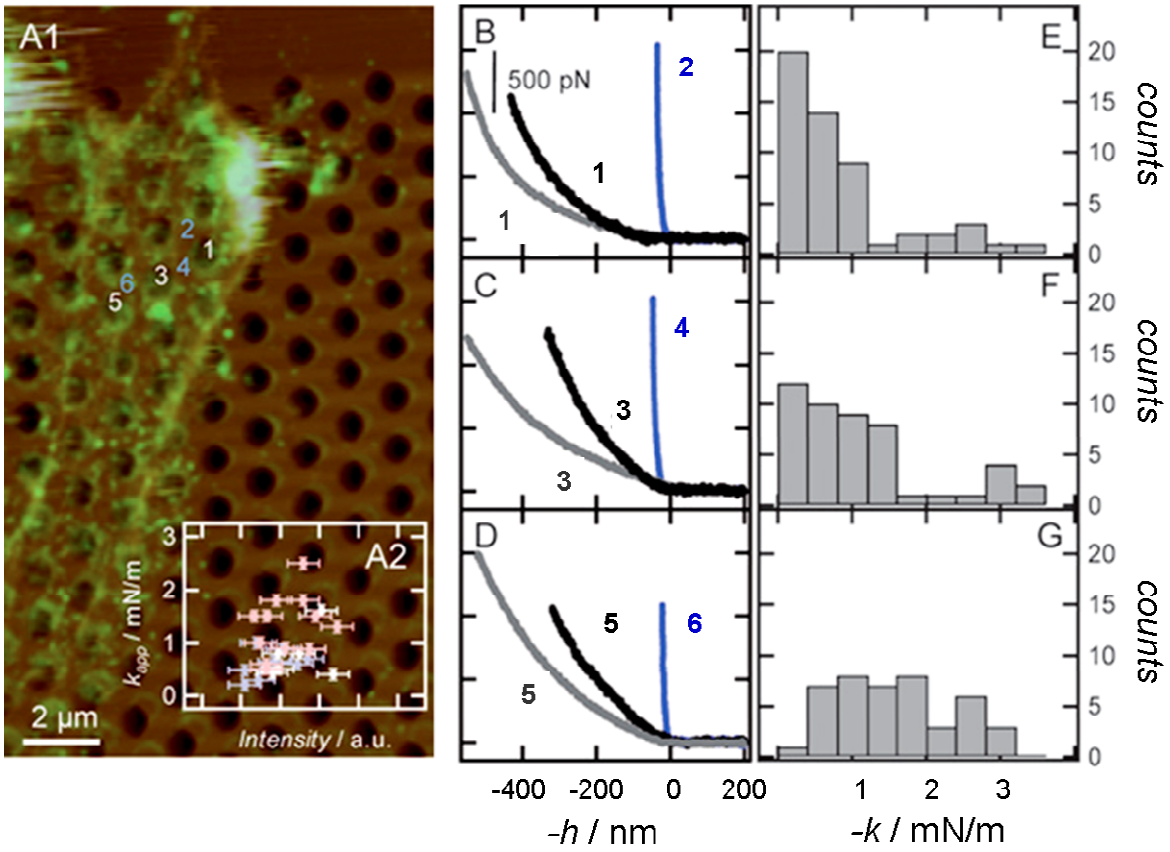

Figure 5.2.0: An overlay (A1) of a fluorescence image of *Phalloidin* Alexa488 labeled F-actin and the corresponding topographic AFM image of a fixated apical membrane. A2 indicates a correlation between fluorescence intensity and the apparent spring constant, representing the membrane stiffness. Three different colors refer to independent experiments: pink: GDA fixated membranes, purple and white: non-fixated membranes. Force indentation curves (B-D) were taken at the positions numbered in A1 before (grey) and after (black) fixation with glutardialdehyde. Histograms of the apparent spring constant (k_{app}) refer to native (E), paraformaldehyde fixated (F) and glutardialdehyde fixated (G) fixated apical membranes.

5.9 Model system

To correlate the reported membrane elastic response to mathematical equations, a model of a thin elastic shell (Landau and Lifshitz, 1970) is used. The ratio between thin and thick plates (shells) refers to the ratio between a given side of plate length (a) and its thickness (t). For a thin plate, this ratio obeys the following proportion as: 8< *a/t* <80. According to the thin plate theory, the bending rigidity (κ_b) of a thin isotropic plate is proportional to the cubic power of the membrane thickness (d) as follows:

$$\kappa_b = \frac{Et^3}{12\left(1-\nu^2\right)}$$

In this expression, E is the Young's modulus, t is the membrane thickness and ν is the Poisson's ratio. The extension rigidity (stretching) is proportional to the first power of the membrane thickness (~ Et). This indicates that if the thickness is very small as it is with cell membranes, the bending rigidity is much smaller than the extension rigidity.

There are three main forces that contribute to a lipid bilayer deformation suspended across 1.2 μm size pores: (1) Bending at small indentation forces which are modeled by a linear thin plate membrane theory. (2) Stretching at large indentation forces which is explained by non linear membrane theory. (3) Lateral tension due to membrane attachment to the pore rim.

Local point indentation (h) of a thin elastic shell with a finite geometry leads to a nonlinear elastic response of $F_{shell}(h)$ versus h. However, the force is linearly proportional to indentation near the zero contact point with a stiffness constant k_{shell}. Since a linear relationship between force and indentation was found at low load in the first 100 nm of membrane deformation, the following linear relationship between force and indentation depth is used (Komaragiri and Begley 2005):

$$F(h) = \frac{4\pi E t^3}{3\left(1-\nu^2\right)R_{pore}^2}$$

This equation relates the force (F) linearly to the indentation depth as two elastic objects are pressed against each other with sphere geometry. The Poisson ratio used is (ν = 0.33) and R_{pore} is the pore radius (600 nm). Based on the thin plate theory, this equation shows a strong dependency between the force and the membrane thickness: ($F \sim t^3$). The force to indent the membrane decreases with increasing pore radius as it was previously shown with free standing lipid bilayer (Steltenkamp et al. 2006). In addition, the contribution of the tip radius is negligible at low indentation forces. Bending rigidity values for cell membranes range from $1.3 \cdot 10^{-20}$J to $7 \cdot 10^{-19}$J (Evans and Rawitz, 1990, 1997, Scheffer et al. 2001, Döbereiher et al. 2001). The smaller the bending rigidity constant, κ_B, the lower is the membrane resistance to deformation (Fan and Fedorov 2003). This dependency is consistent with higher membrane stiffness values (k_{app}) following fixation with glutardialdehyde and after cholesterol extraction with MBCD. As bending represents linear elastic response of the cell membrane at small forces, the bending equation can be regarded as the equivalence of Hook's law. The apparent membrane spring constant (k_{app}) can be calculated and compared to that obtained experimentally according to the following term:

$$k_{app} = \frac{4\pi E t^3}{3\left(1-\nu^2\right)R_{pore}^2}$$

Since rupture events were generally not observed upon indentation, it is very likely that lipid material is withdrawn from the adjacent rim upon indentation giving rise to a constant lateral tension. In addition, calculations of the apparent spring constant, k_{app}, as a function of lateral tension, σ_{app}, and bending modulus, κ_B, showed that meaningful variation in the lateral tension do not change significantly the slope, $k_{app,}$ of the force indentation curves following fixation (Lorenz et al. 2009).

In case that Stretching is the main contributor to the membrane elastic response, an equation based on the non linear membrane theory can be used (Begley et al. 2004):

$$F(h) = \frac{9\pi Et}{16R_{tip}^2\left(\frac{R_{pore}}{R_{tip}}\right)^{9/4}}h^3$$

This equation is valid for a spherical indenter and the case of zero pre-stress. According to this equation, the stretching force varies nonlinearly as the cube of the indentation ($F \sim h^3$) and it matches the non-linear elastic response observed experimentally at higher forces and a higher indentation depth. Taking into account that both bending and stretching were observed with the indentation of free standing apical membranes, an additive combination of both bending and stretching is suggested as follows:

$$F(h) = \frac{4\pi Et^3}{3(1-\nu^2)R_{pore}^2}h + \frac{9\pi Et}{16R_{tip}^2\left(\frac{R_{pore}}{R_{tip}}\right)^{9/4}}h^3$$

This linear combination provides a mean to fit the data in order to obtain values for E and t. Figure 5.2.1A shows computed force indentation curves based on the bending (1:blue curve), stretching (2: red curve) and combined (1+2: green curve) equations. The values used for these equations are: R_{pore} = 600 nm, R_{tip} = 20 nm, E = 15.2 kPa, $\kappa = 7 \cdot 10^{-19}$J and t = 85 nm. A fit of this equation to a force indentation curve obtained experimentally is shown in figure 5.2.1B. It demonstrates that only combination of both bending and stretching fits to the experimental indentation curves.

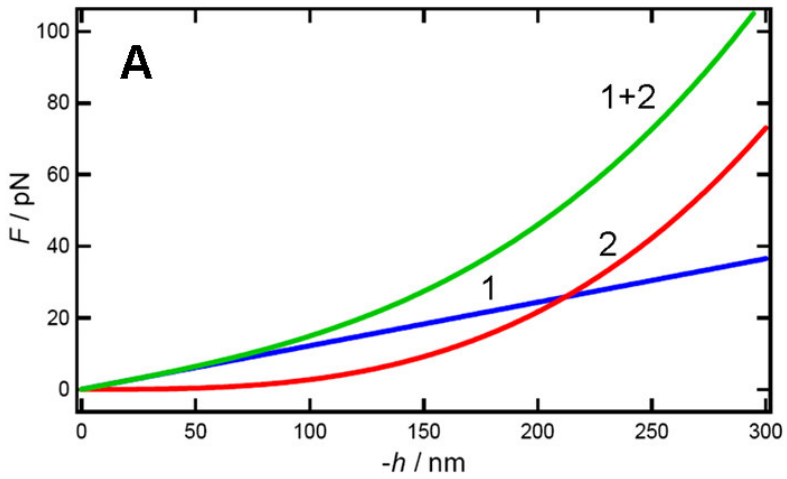

Figure 5.2.1: A: Computed force indentation curves matching to the equation of bending rigidity, κ_B, (1: blue curve), stretching (2: red), and both bending and stretching (1+2: green).

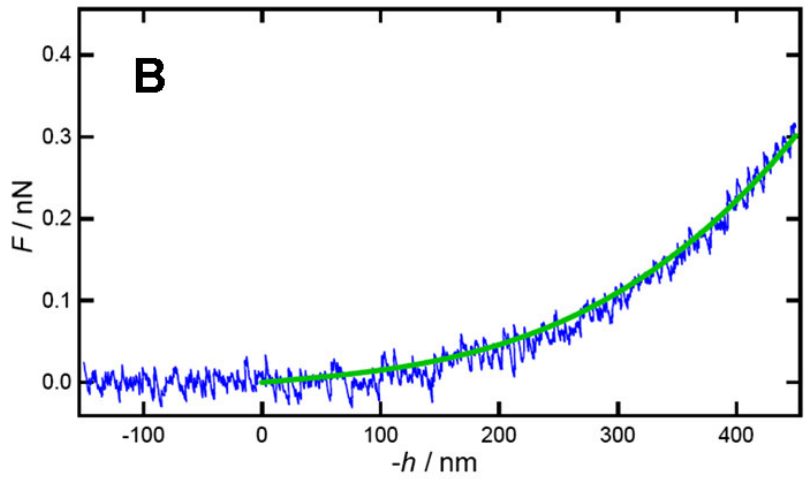

B: Force indentation curve (blue), taken from a membrane covered por, was fitted with equation 1+2 (green).

To summarize, an elastic model of a thin shell was used to explain the deformation of free standing apical membrane across 1.2 µm size pores. This model has been previously applied with various biological samples to explain membrane deformation (Arnoldi et al., 2000, de Pablo et al., 2003, Ivanovska et al., 2004, Zelelskaya et al., 2006) and herein it is used for the first time to model the elastic response of MDCK II epithelial apical membranes. The bending rigidity value ($\kappa_B = 7 \cdot 10^{-19}$J), used for the fit equation, is consistent with the range previously suggested for MDCK II cell membrane fragments to reproduce the experimentally measured k_{app} (Lorenz et al. 2009).

5.1.0 Friction force effect

To estimate the influence of drag forces on the apical membrane elastic response during indentation, sequential force indentation curves with increasing loading rates were performed on pore/rim covered membrane in PBS and following fixation with glutardialdehyde (Figure 5.2.2). Hysteresis, represented as the area enclosed between the indentation (green) and the relaxation (black) curves, reflects the membrane friction forces acting on the cantilever. Force indentation curves taken from native membranes resulted in increasing hysteresis from cantilever velociy 2.5 µm/s to 25 µm/s indicating a viscoelastic response. Hysteresis at the non-contact regime is a result of the friction of the measuring fluid (PBS) acting on the cantilever before it contacts the membrane (Hoh and Engel 1993). To eliminate this hydrodynamic effect, force indentation curves were graphically corrected to the baseline. No hysteresis was observed at lower velocity (0.25 µm/s), suggesting that force indentation curves recorded at this time scale are dominated by the elastic response and the influence of the membrane viscosity is minimal. The linear slope, k_{app}, did not change with the increasing velocity (figure 5.2.3), indicating that the observed hysteresis did not lead to plastic irreversible deformation and there is no effect on the membrane elastic response at the examined velocity range. In contrast, force indentation curves taken from living MDCK II cells (figure 5.2.4) at cantilver velocity greater than 10 µm/s show smaller indentation depth in comparison

to those taken at lower velocities at the same small force, which results in an increase of the Young's modulus (Sneddon 1965, Steltenkamp et al. 2006).

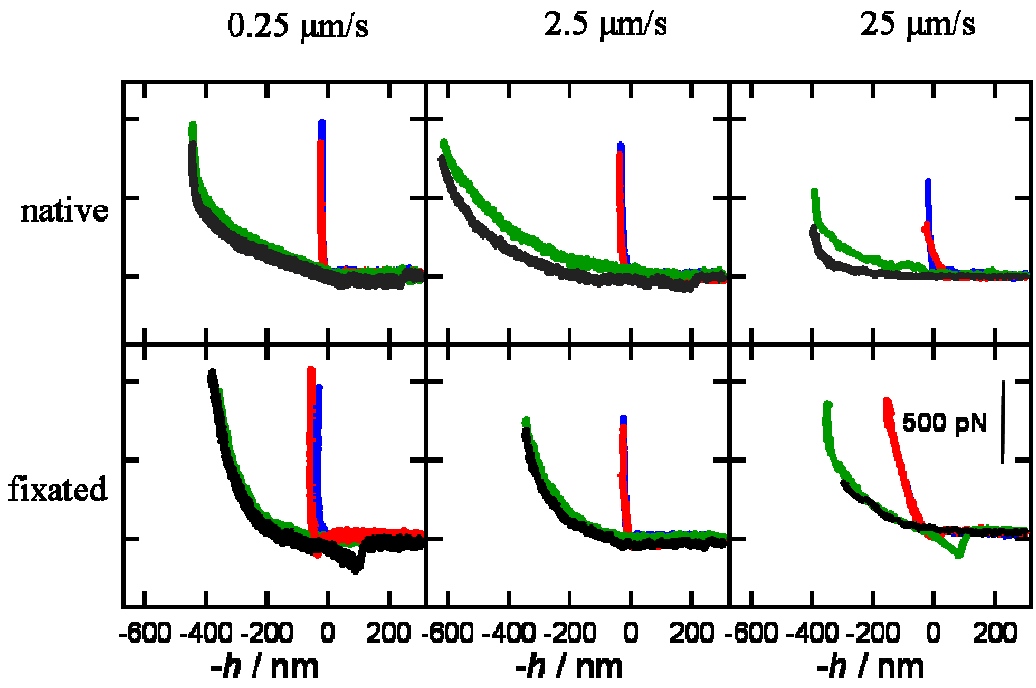

Figure 5.2.2: Force indentation curves taken on free standing native (PBS) and glutardialdehyde fixated (GDA) apical membranes (1.2 µm size pores) at different z scan rates. Indentation curves on the pore centre are presented in black and relaxation curves are in green. Approach curves on the adjacent pore rims are shown in blue, while the corresponding retraction curves are shown in red.

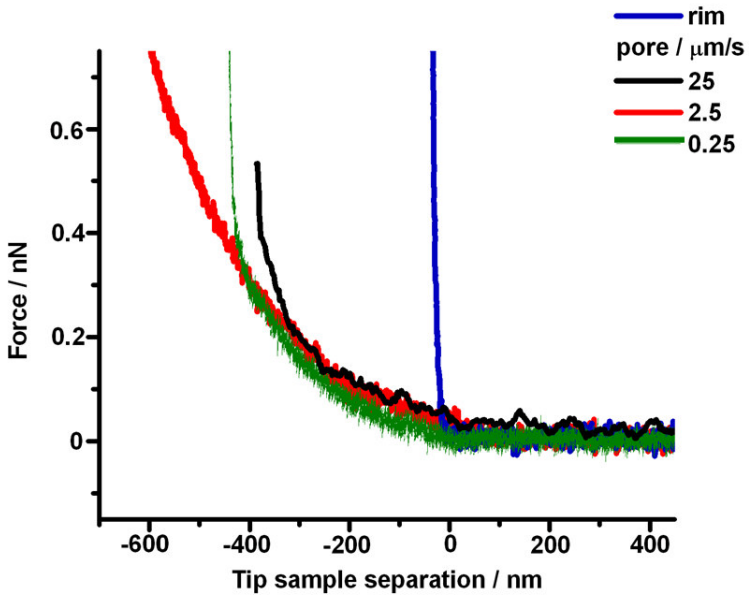

Figure 5.2.3: consecutive indentation curves recorded with native membrane from the same pore at different z scan rates. With the increasing velocity, the membrane stiffness, reflected by the membrane spring constant: 0.5 *mN/m*, was kept the same, indicating no change in the linear regime of the membrane elastic response.

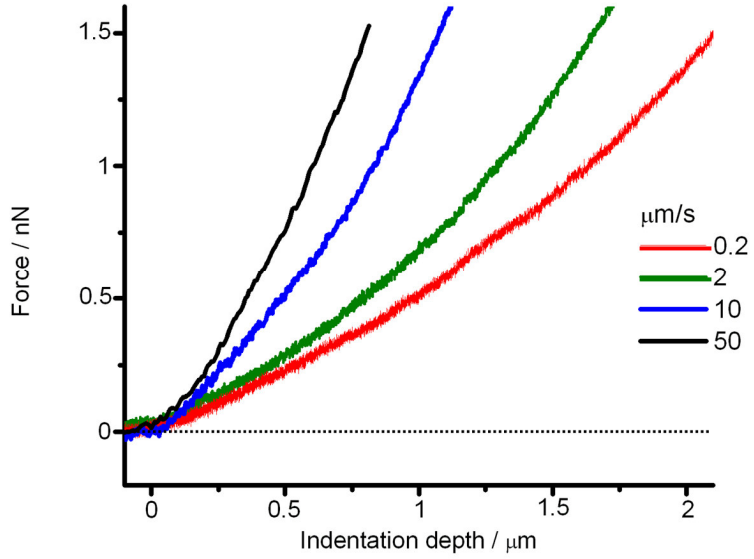

Figure 5.2.4.: A: Force indentation curves reported from the nuclear region of a living MDCK II cell at increasing cantilever velocity (μm/s). Cantilever velocity greater than 10 μm/s leads to an increase of the Young's modulus in comparison to smaller velocites at the same small force.

Force indentation curves recorded with artificial lipid membranes (Mey et al. 2009) reported no hysteresis, implying that a substantial contribution of viscosity stems from the microfilaments (F-actin) attached to the apical membrane fragments and the flow on the rim. Force indentation curves recorded from glutardialdehyde fixated membranes at the same cantilever velocity range revealed no change in the membrane elastic response. The friction forces acting on the cantilever are reduced as no hysteresis was reported. This indicates that protein cross linking changes the chemical property of the attached microfilaments leading to a reduction in the fragment viscosity. Significant decrease in energy dissipation was also reported with MDCK II cells following chemical fixation with glutardialdehyde.

To qualitatively understand the observed hysteresis, a three-body viscoelastic model (Xu and Shao 2008, Hochmuth et al. 1979) was used. It is based on a modified version of the Kelvin-Voigt mechanical model illustrated in figure 5.2.5 (Zhang 2005). It consists of a spring element representing the initial linear elastic response of the membrane (bending) which is connected in series to a second non linear spring, demonstrating the nonlinear elastic response (stretching). Both springs are connected in series to a Kevin-Voigt model, demonstrating the viscoelastic response reported from native membranes with increasing cantilever velocity. The spring refers to the elastic response and the piston immersed in the viscous liquid relates to the membrane viscosity resulting in energy dissipation depending on the cantilever velocity. According to this model, the following force indentation, $F^{ind}(h)$ and force relaxation, $F^{relax}(h)$, equations are suggested:

$$F^{ind} = \frac{4\pi E t^3}{3\left(1-\nu^2\right)R_{pore}^2}h + ER_{pore}\frac{\pi}{3}t\left(\frac{h}{R_{pore}}\right)^3 + F_{KV}^{ind}\left(h\right)$$

$$F^{relax} = \frac{4\pi E t^3}{3(1-\nu^2)R_{pore}^2} h + E R_{pore} \frac{\pi}{3} t \left(\frac{h}{R_{pore}} \right)^3 + F_{KV}^{relax}(h)$$

The first and the second terms of this equation refer to membrane bending and membrane stretching, respectively. $F^{ind}(h)$ and $F^{relax}(h)$ represent the solutions of the Kelvin-Voigt model:

$$F(t) = kh + \eta \frac{dh}{dt}$$

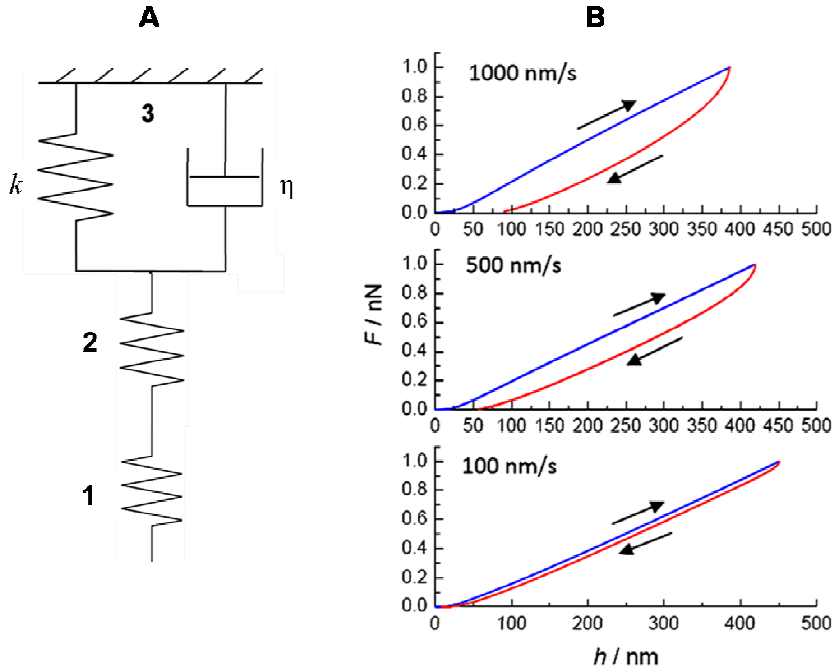

Figure 5.2.5: A: Schematic of the three parameter solid model. The first spring (1) refers to a Hookean spring representing the linear regime of membrane deformation at low forces and low indentation depth which is governed by bending (κ_b). The second spring (2) illustrates a nonlinear spring demonstrating membrane stretching at high forces and high indentation depth. The third parameter is a Kelvin-Voigt model representing viscoelasticity reported with native membranes. The spring illustrates the elastic part and the piston connected in parallel to a piston immersed in liquid representing the membrane viscosity leading to energy dissipation with increasing cantilever velocity. B: Simulated indentation and relaxation curves of a nonlinear Kelvin-Voigt model as a function of indentation velocity. Due to the small time constant (0.04 s) the hysteresis increases with increasing velocity as reported with free standing apical membranes.

Figure 5.2.5B illustrates the membrane elastic response based on a simulation of a nonlinear Kelvin-Voigt model as a function of indentation velocity. This simulation, computed with a small relaxation time (τ = 0.04 s), reports an increasing hysteresis with the increasing indentation velocity as it was recorded with the experimental data. Small relaxation time (τ < 1s) indicates that time required for the membrane to return to its initial shape is longer than the indentation time. In order to minimize energy dissipation, the indentation time must be increased which means smaller cantilever velocity. This behavior is opposed to polymer films which exhibit a decreasing hysteresis with increasing indentation velocity (Zhang and Zhang 2007).

5.1.1 Pulse force modulation of apical membranes

To expand the possibilities of apical membrane imaging with an AFM, the digital Pulse Force Mode was used. This setup is similar to contact mode with three main differences: 1) the cantilever oscillates over the surface and it is not in constant contact with the sample. As a result, lateral forces are reduced. 2) A stiff contact mode cantilever with a spring constant of 0.1 N/m was used. 3) The signal used to form the image is the amplitude of the cantilever motion and the obtained images (maps) are based on the recorded force cycles (Maganov and Reneker 1997). Figure 5.2.6 displays a typical force modulation cycle in PBS reported from a rim (D) of a porous Si/SiO_2 substrate. In this curve the cantilever deflection is plotted against the time required to complete one cycle (4 ms). The cantilever is in contact with the sample from point a (snap on) to point c (snap off). The drag forces at the non contact region are clearly visible and they originate from the liquid motion. Force curve based maps (A-C) of the same membrane fragment recorded by contact mode and PFM imaging, respectively. Membrane borders are visible both with the height image (A) and the topography map (B). The color contrast between the membrane fragment and the uncovered pores in C is based on the adhesion property. Dark areas in the image indicate more adhesion. The PFM cycles shown in E and F relate to a membrane covered rim and pore (points 2 and 3 from the PFM topography map (C). The maximal cantilever deflection reported from a membrane covered pore is 50 nm less than that reported from the rim. This indicates that the membrane is indented into the pore, so the cantilever deflection is reduced. A rigid surface, a membrane covered rim, does not allow the tip to freely indent the membrane, thus the maximal deflection is about the same as that recorded from an uncovered rim.

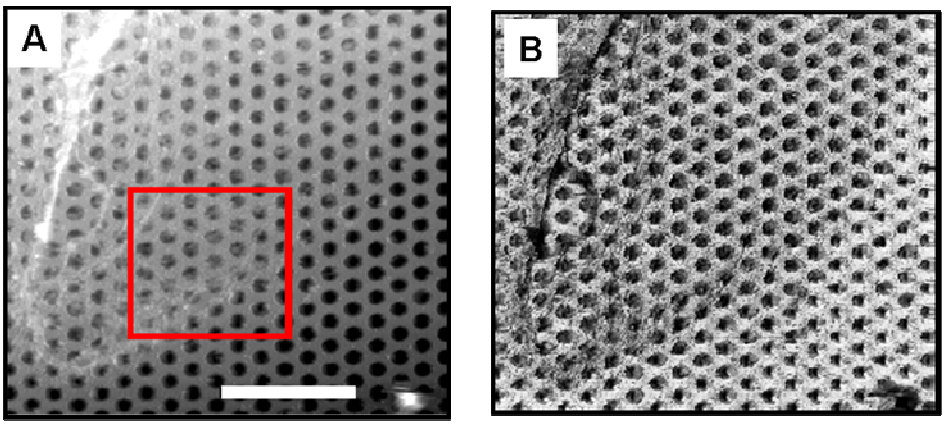

Figure 5.2.6: Free standing apical membrane fragment. A: Height image. Scale bar: 10 µm. B: The matching adhesion image recorded with Pulse Force Mode. Scale bar: 10 µm.

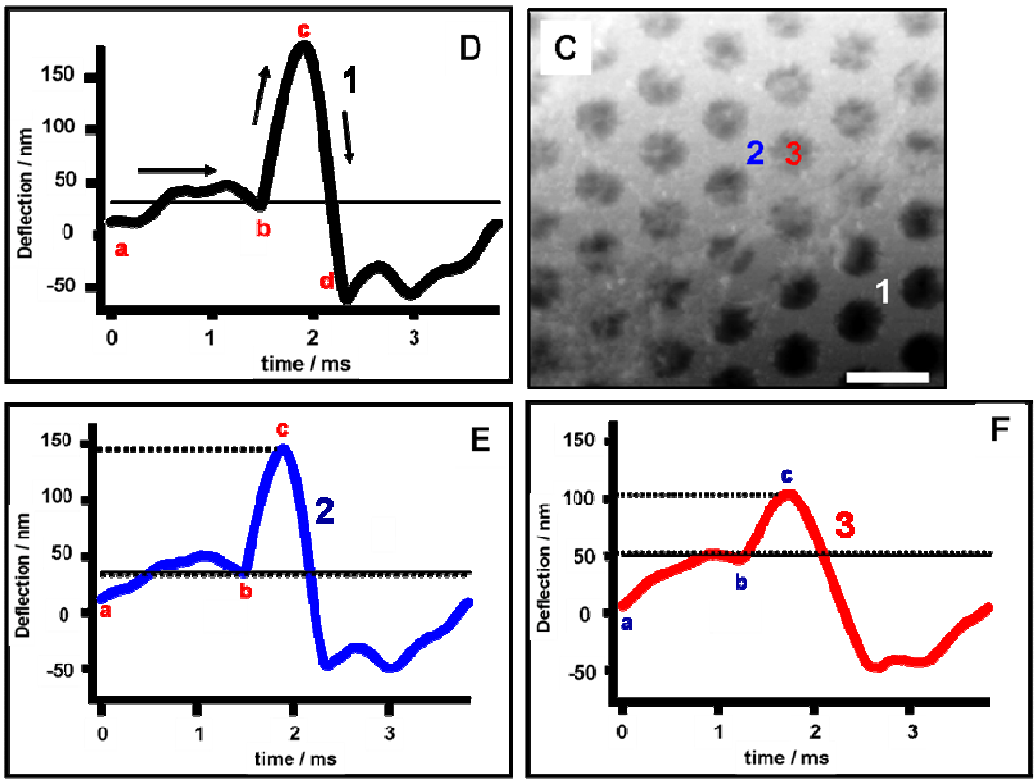

C: Height image refers to the maked area in B. Scale bar is 2 µm. Pulse Force Mode cycles were recorded from an empty rim (D), membrane covered rim (E), and membrane covered pore (F). The location of these PFM curves is shown in C (1: empty rim, 2: covered rim, 3: covered pore).

5.1.2 Conclusions

Successful preparations of apical membrane sheets resulted in functional free standing native membrane fragments. Force mapping of these fragments reveals a soft elastic response of the membrane indented in the centre of a pore in comparison to hard repulsion reported from the adjacent rim. A linear force versus indentation regime over the first 100 nm of membrane deformation was fitted by a linear regression in order to calculate the membrane stiffness. Protein cross linking of native membranes with GDA chemical fixation resulted in membrane stiffening. Removal of F-actin by DNAse I and gelsolin was mostly detectable at high forces in the nonlinear regime of the elastic response. An increase of the membrane stiffness was reported following cholesterol depletion from membrane fragments with MBCD. This finding is in good agreement with measurments carried out with living cell by micropipette aspiration, suggesting an increase of the adhesion energy between the lipid bilayer and the underlying cytoskeleton following cholesterol extraction. However, elasticity measurement of living MDCK II cells after cholesterol extraction was not possible with an AFM due to cell detachment from the porous substrate. The origin of the restoring forces recorded by force indentation curves is related both to membrane bending and stretching. To explain this behavior, a thin elastic shell model was applied suggesting a linear proportion (membrane bending) between the applied force and the membrane indentation depth close to the contact point at small forces.

Membrane stretching is related to a nonlinear elastic response observed at higher forces. A bending modulus of $\kappa_b = 7 \cdot 10^{-19}$ J and Young's modulus of 15.2 kPa was obtained by fitting an experimental indentation curve with a combination of bending-stretching equation. Adhesion map of free standing apical membrane fragment, recorded with the PFM measurement mode, revealed a clear contrast between covered and uncovered pores based on the adhesion properties of the membrane surface.

6. SUMMARY AND PRESPECTIVES

The mechanical properties of cells are governed by three main factors: 1) cell membrane 2) Cytoskeleton 3) Cytosol.

In the first part of this thesis it was shown that MDCK II epithelial cells cultivated on a porous substrate exhibit lower distribution of actin stress fibers than those on the rim. According to the tensegrity model (Ingber et al. 1981) cellular forces generated mainly by F-actin and intermediate filaments are responsible for the prestress existed in the cells functioning as load bearing elements. These forces, maintaining the structural integrity of the cell, are partially balanced by anchoring points of integrin transmembrane receptors which bind the cytoskeleton to the underlying substrate (Stamenović and Ingber 2006). Any disturbance of this force balance would lead to structural rearrangement of the cytoskeleton influencing the cell's deformability. Therefore, it is suggested that cultivating of cells on a porous substrate with 1.2 μm size pores, providing less attachment points for the cells to the underlying substrate, leads to cytoskeleton rearrangement effecting on the cell deformability. The calculated Young's modulus from the nucleus region was 4 fold lower than that previously reported for cells on a non porous substrate. It was recently shown that the higher the cell substrate stiffness, the denser is the distribution of F-actin stress fibers (Byfield et al. 2009). To confirm the obtained results, further investigation must be carried out, such as elasticity measurement before and after incubation with cytoskeleton disrupters. In addition, more fluorescent markers should be used in order to evaluate the distribution of other cytoskeletal filaments: intermediate filaments and microtubules. However, fluorescence investigation provides only qualitative information and small changes in F-actin distribution cannot be quantified. More cell lines should be cultivated on porous substrate in order to check if low distribution of F-actin is specific only to epithelial MDCK II cells.

The advantage of a porous substrate over a planar surface is clearly demonstrated by force indentation of thin films, such as the cell edge. As the cell edge is indented into the pores, the contribution of a stiff rim is avoided.

In addition to elasticity measurements, the AFM is also a powerful tool to characterize the morphology of biological surfaces, such as those of epithelial cells which can be described in terms of microvilli and planar subdomains. AFM height images of fixated and dehydrated MDCK II cells were carried out to shed light on the organization of apical microvilli. These images reveal an increase in length, whereas the density is kept the same. Since this elongation process is ATP dependent, additional investigation can be done by using toxicants which lead to ATP depletion. Microvilli height images can also be applied in pathological diagnostics. In contrast to SEM, the measurement with AFM is carried out at room temperature which does not require extreme conditions, such as vacuum and an electron beam. Importantly, sample preparation is minimal which avoids possible artifacts.

The second part of the thesis was dedicated to elasticity measurement of apical membrane fragments in order to avoid the influence of the cell's osmotic pressure and internal organelle on the recorded elastic response. To detach native apical membranes from a cell monolayer, a new protocol was established. AFM and fluorescence images indicate that intact membrane sheets containing F-actin cover the pores. Since these fragments were not firmly bound to the poly-D-lysine coated chip, the main difficulty was to avoid their removal by the cantilever tip during contact mode imaging. Force mapping of free standing apical membranes reveal soft elastic response due to indentation into the pores in comparison to a hard repulsion recorded from the rim. The elastic response of free standing apical membrane to a point load force can be divided into three main contributions: 1) bending resistance upon indentation. 2) Area dilatation due to stretching of the lipid bilayer plus the attached cytoskeletal filaments. 3) Lateral tension as a result of the attachment of the membrane to the rim, providing material reservoir. Assuming a point load in the centre of an axisymmetric pore, the expected force indentation curves are linear for small forces and indentation depth. Since rupture events were mostly not observed upon indentation at high forces, it is suggested that lipid material serving as membrane reservoir is withdrawn into the pores, leading to a constant lateral tension. Moreover, relative area change greater than 5% (Boal 2002) results in membrane rupture. Previous investigation with free standing basolateral membranes has shown that reasonable variations in the lateral tension do not change the slope of the force indentation curves (k_{app}) significantly enough to explain the changes in stiffness after protein cross linking by chemical fixation (Lorenz et al. 2009). In addition, force indentation curves are insensitive to variations in the tip-radius as proven by seminumerical calculations (Steltenkamp et al. 2006). Removal of F-actin was detected at high forces at the non linear regime of the force indentation curve, reflecting membrane stretching. However, the efficacy of actin disrupters on F-actin depolymerization was mainly tested on whole living cells (Rotsch and Radmacher 2000). In addition, the variation of membrane thickness obtained by each preparation and the lack of a quantitative assay to calculate the amount of F-actin in intact membrane fragments before and after treatment do not allow accurate estimation of small changes in elasticity.

Native apical membranes exhibit a velocity dependent hysteresis between the indentation and relaxation, indicating a viscoelastic response that is also typical for living MDCK II cells.

To summarize, it was possible, for the first time, to investigate the local mechanical properties of isolated apical cell membranes on porous support. The heterogeneous elastic response is governed by bending which is a function of cytoskeleton and cross linked proteins.

A. A-Hassan, W.F. Heinz, M.D. Antonik, N.P. D'Costa, S. Nageswaran, C.-A. Schoennenberg, J.H. Hoh (1998). Relative microelastic maping of living cells by atomic force microscopy. *Biophys. J.* 74: 1564-1578.

J.C. Adams, F.M. Watt (1993). Regulation of development and differentiation by the extracellular matrix. *Development*.117: 1183-1198.

B.M. Aizenbud, N.D. Gershon (1982) Diffusion of molecules on biological membranes of nonplananr form. *Biophys. J.* 38: 287-293.

B. Alberts, A. Johnson, J. Lewis, M. Raff, K. Roberts, P. Walter (2005). *Molecular biology of the cell*. Fourth edition. Garland Science, New York.

J. Alcaraz, L. Buscemi, M. Puig-de-Morales, J. Colchero, A. Baró, D. Navajas (2002). Correction of microrheological measurements of soft samples with atomic force microscope for the hydrodynamic drag on the cantilever. *Langmuir*. 18: 716-721.

C.T. Anderson, A.B. Castillo, S.A. Brugmann, J.A. Helms, C.R. Jacobs, T. Stearns (2008). Primary cilia: cellular sensors for the cytoskeleton. *Anat. Rec.* 291: 1074-1078.

M. Arnoldi, M. Fritz, E. Bäuerlein, M. Radmacher, E. Sackmann, A. Boulbitch (2000) Bacterial turgor pressure can be measured by atomic force microscopy. *Phys. Rev E*. 62(1) 1034-1044.

A. Atala, R. Lanza, R. Nerem, J.A. Thomson (2008). *Principles of regenerative medicine.* 2nd edition, MA, USA.

Y. Barenholz (2002). Cholesterol and other membrane active sterols: from membrane evolution to "rafts". *Prog. Lipid Res.* 41: 1-5.

A.R. Bausch, F. Ziemann, A.A. Boulbitch, K. Jacobson, E. Sackmann (1998). Local measurements of viscoelastic parameters of adherent cell surfaces by magnetic bead microrheometry. *Biophys. J.* 75: 2038-2049.

R. Begley, T.J. Mackin (2004). Spherical indentation of freestanding circular thin filmsin the membrane regime. *J. Mech. Phys. Solids*. 52: 2005-2023.

B. Bhushan (2008). *Nannotribology and nanomechanics: An introduction*. Springer, Berlin, 2nd edition

G. Binnig, C.F. Quate, C. Gerber (1986). Atomic force microscope. *Phys. Rev. Lett*. 56: 930-933.

D. Boal (2002). *Mechanics of the cell*, Cambridge University Press, Cambridge.

M. Bomsel, A. Alfsen (2003). Entry of viruses through the epithelial barrier: pathogenic trickery. *Nat. Rev. Mol. Cell Biol.* 41(1): 57-68.

E. Boschung, M. Heuberger, G. Dietler (1994). Energy dissipation during nanoscale indentation of polymers with an atomic force microscope. *Appl. Phys. Lett.* 64: 1794

F. Braet et al. (1998). Imaging surfaces and submembranous structures with the atomic force microscope: a study on living cancer cells fibroblasts and macrophages. *J. Microscopy.* 190: 328-338.

D.A. Brown, E. London (2000). Structure and function of sphingolipid and cholesterol-rich membrane rafts. *J. Biol. Chem*. 275: 17221-17224.

G.R. Bushell et al. (1999). Imaging and force-distance analysis of human fibroblasts *in vitro* by atomic force microscopy. *Cytometry.* 36: 254
C. Bustamante, D. Keller (1995). Scanning force microscopy in biology. *Phys. Today.* 48(12): 32-38.

H.-J. Butt et al. (1990). Imaging cells with the atomic force microscope. *J. Struct. Biol.* 105: 54-61.

H.-J. Butt, B. Cappella, M. Kappel (2005). Force measurements with the atomic force micrcoscope: Technique, interpretation and applications. *Surf. Sci. Rep*. 59: 1-152.

F.J. Byfield, H. Aranda-Espinoza, V.G. Romanenko, G.H. Rothblat, I. Levitan (2004). Cholesterol depletion increases membrane stiffness of aortic endothelial cells. *Biophys. J.* 87: 3336-3343.

F.J. Byfield, R.K. Reen et al. (2009). Endothelial actin and cell stiffnessis modulated by substrate stiffness in 2D and 3D. *J. Biomechn* 42: 1114-1119.

A. Cattelino, C. Albertinazzi, M. Bossi, D.R. Critchley, I. De Curtis (1999). A cell free system to study regulation of focal adhesions and of the connected actin cytoskeleton. *Mol. Biol. Cell.* 10: 373-391.

D. Choquet, D.P. Felsenfeld, M.P. Sheetz (1997). Extracellular matrix rigidity causes strengthening of integrin-cytoskeleton linkages. *Cell* 88(1): 39-48.

P. Colarusso, K.R. Spring (2002). Reticulated lipid probe fluorescence reveals MDCK cell apical membrane topography. *Biophys. J*. 82:752-761.

A.E. Cremesti, F.M. Goni, R. Kulesnick (2002). Role of sphingomyelinase and ceramide in modulating rafts: do biophysicalproperties determine biological outcome? *FEBS Lett.* 531: 47-53.

E. Cukierman, R. Pankov et al. (2002). Taking cell-matrix adhesions to the third dimension. *Science* 294(5547): 1708-1712.

J. Dai, M.P. Sheetz (1995). Mechanical properties of neuronal growth cone membranes studied by tether formation with laser optical tweezers. *Biophys. J.* 68: 988-996.

B. Daily, E.L. Elson, G.I. Zahalak (1984). Cell poking. Determination of the elastic area compressibility modulus of the erythrocyte membrane. *Biophys. J.* 45: 671-682.

C. Danelon, J.B. Perez, C. Santschi,, J. Brugger, H. Vogel H (2006). Cell membranes suspended across nanoaperture arrays. *Langmuir* 22:22–25.

D.J. DeRosier, L.G. Tilney (2000). F-actin bundles are derivatives of microvilli: what does this tell us about how bundles might form? *J. Cell Biol.* 148: 1-6.

E.K. Dimitriadis, F. Horkay, J. Maresca, B. Kachar, R.S. Chadwick (2002) Determination of elastic moduli of thin layers of soft material using the atomic force microscope. *Biophys. J.* 82: 2798-2810.

J. Domke, M. Radmacher (1998). Measuring the elastic properties of thin polymer films with the atomic force microscope. *Langmuir*. 14: 3320-3325.

D. Drenckhahn, R. Dermitzel (1988). Organization of the actin filament cytoskeleton in the intestinal brush border: a quantitative and qualitative immunoelectron microscope study. *J. Cell Biol.* 107: 1037-1048.

D.G. Drubin, W.J. Nelson (1996). Origins of cell polarity. *Cell* 84: 335-344.

Y.F. Dufrêne (2008). Towards nanomicrobiology using atomic force microscopy. *Nat. Rev. Microbiol.* 6: 674-680.

A.J. Engler et al. (2004). Surface probe measurements of the elasticity of sectioned tissues, thin gels and polyelectrolyte multilayer films: correlations between substrate stiffness and cell adhesion. *Surf. Sci.* 570: 142.

J. Evangelides, D.N. Sheppard, T.J. Mcmaster (2009). New developments in the structural and functional investigation of primary cilia using AFM and confocal microscopy. *Biophys. J.* 96(3) Supp.1: 396.

J. Evangelides, D.N. Sheppard, T.J. Mcmaster (2008). Imaging primary cilia on MDCK cells using atomic force microscopy. *Proc. Physiol.* Soc9, C4.

E.A. Evans (1974). Bending resistance and chemically induced moments in membrane bilayers. *Biophys. J.* 14: 923-931.

E. Evans, V. Heinrich, A. Leung, K. Kinoshita (2005). Nano-to microscale dynamics of P-selectin detachment from leukocyte interfaces. I. Membrane separation from the cytoskeleton. *Biophys. J.* 88: 2288-2298.

E. Evans, W. Rawitz (1997). Elasticity of "fuzzy" biomembranes. *Phys. Rev. Lett.* 79: 2379-2382.

E. Evans, D. Needham (1987). Physical properties of surfactant bilayer membranes: thermal transitions, elasticity, rigidity, cohesion, and colloidal interactions. *J. Phys. Chem.* 91: 4219-4218.

E. Evans, A. Yeung (1989). Apparent viscosity and cortical tension of blood granulocytes determined by micropipet aspiration. *Biophys J.* 56(1):151–160.

T.-H. Fan, A.G. Fedorov (2003). Analysis of hydrodynamic interactions during AFM imaging of biological membranes. *Langmuir*. 19: 1347-1356.

E. Farge, D.M. Ojcius, A. Subtil, A. Dautry-Versat (1999). Enhancement of endocytosis due to aminophospholipid transport across the plasma membrane of living cells. *Am. J. Physiol.* 27: C725-C733.

W.N. Findley, J.S. Lai, K. Onaran (1989). Creep and relaxation of nonlinear viscoelastic materials.

T. Fine, I. Mey, C. Rommel, J. Wegener, C. Steinem, A. Janshoff (2009). Elasticity mapping of apical cell membranes. *Soft Matter.* 5: 3262-3265.

M.G. Ford et al. (2002). Curvature of clathrin-coated pits driven by epsin. *Nature.* 419: 361-366.

D.J. Frankel, J.R. Pfeiffer, Z. Surviladze, A.E. Johnson, J.M.Oliver, B.S. Wilson, A.R. Burns, (2006). Revealing the topography of cellular membrane domains by combined atomic force microscopy/ fluorescence imaging. *Biophys. J.* 90(7): 2404-2413.

T. Funatsu, H. Higuchi, S. Ishiwata (1990). Elastic filaments in skeletal muscle revealed by selective removal of thin filaments with plasma gelsolin. *J. Cell Biol.* 110:53-62.

C. Gerber, H.P. Lang (2006). How the doors to the nanoworld were opened. *Nat. Nanotechnol.* 1:3-5.

F. Gittes, B. Mickey, J. Nettleton, J. Howard (1993). Flexural rigidity of microtubules and actin filaments measured from thermal fluctuations in shape. *J. Cell Biol.* 120: 923-934.

R.P. Gonçalves, G. Agnus, P. Sens, C. Houssin, B., Bartenlian, S. Scheuring (2006). Two-chamber AFM: probing membrane poteins separating two aqueous compartments. *Nature Methods*.3: 1007-1112.

J. Gorelik et al. (2003). Dynamic assembly of surface structures in living cells. *PNAS.* 100: 5819-5822.

U. Hartmann (1991). Van der Waals interactions between sharp probes and flat sample surfaces. *Phys. Rev. B43.* 2404-2407.

J. Helenius, C.P. Heisenberg, H.E. Gaub, D.J. Müller (2008). Single-cell force spectroscopy. *J. Cell Sci.* 121: 1785-1791.

H. Herrmann, J.R. Harris (1988). Intermediate filaments: *Subcellular biochemistry*, v.3.

H. Herz (1881). Über den Kontakt elastischer Körper. *J. Reine Angew. Mathematik*. 92: 156.

J.E. Hinshaw, S.L. Schmidt (1999). Dynamic self-assembles into rings suggesting a mechanism for coated vesicle budding. *Nature*. 374: 190-192.

H. Hirata, K. Ohki, H. Miyata (2005). Mobility of integrin α5β1 measured on the isolated ventral membranes of human skin fibroblasts. *Biochim. Et Biophys. Acta*. 1723: 100-105.

S.E. Hitchcock, L. Carlsson, U. Lindberg (1976). Depolymerization of F-actin by deoxyribomuclease I. *Cell*. 7:531-542.

R.M. Hochmuth, J. Shao, J. Dai, M.P. Sheetz (1996). Deformation and flow of membrane into tethers extracted from neuronal growth cones. *Biophys. J.* 70: 358-369.

R.M. Hochmuth, P.R. Worthy, E.A. Evans (1979). Red cell extensional recovery and the determination of membrane viscosity. *Biophys. J*. 26: 101-114.

J.H. Hoh, A. Engel (1993). Friction effects on force measurements with an atomic force microscope. *Langmuir*. 9: 3310-3312.

J.H. Hoh, C.-A. Schoenenberger (1994). Surface morphology and mechanical properties of MDCK monolayers by atomic force microscopy. *J. Cell Sci*. 107: 1105-1114.

C. Huet, M. Arpin, D. Louvard (1989). Villin induces MV growth and actin redistribution in transfected fibroblasts. *Cell.* 59: 461-475.

J.L. Hutter, J. Bechhoefer (1993). Calibration of atomic-force microscope tips. *Rev. Sci. Instrum.* 64(7): 1868-1873.

D.E. Ingber, J.A. Madri, J.D. Jameison (1981). Role of a basal lamina in the neoplastic disorganization of tissue architecture. *Proc. Natl. Acad. Sci. USA*. 78: 3901-3905

I.L. Ivanovska, P.J. de Pablo, B. Ibarra, G. Sgalari, F.C. MacKintosh, J.L. Carrascosa, C.F. Schmidt, G.J.L. Wuite (2004). Bacteriophage capsids: tough nanoshells with complex elastic properties. *Proc. Natl. Acad. Sci.* 101: 7600-7605.

P.A. Janmey (1996). Coping with cellular stress: The mechanical resistance of porous protein networks. *Biophys. J.* 71: 3-7.

P.A. Janmey, U. Euteneuer, P. Traub, M. Schliwa (1991). Viscoelastic properties of vimentin compared with other filamentous bipolymer networks. *J. Cell Biol.* 113: 155-160.
H. Janovjak J. Struckmeier, D.J. Müller (2005). Hydrodynamic effects in fast AFM single-moleculae force measurements. *Eur. Biophys. J*. 34: 91-96.

R.D. Kamm, M.R.K. Mofrad (2006). *Cytoskeleton mechanics: models and measurement.* Cambridge.

J. Käs et al. (1996). F-Actin, a model polymer for semiflexible chains in dilute,semidilute, and liquid crystalline solutions. *Biophys. J.* 70: 609-625.

S. Kidoaki, T. Matsuda, K. Yoshikawa (2006). Relationship between apical membrane elasticity and stress fiber organization in fibroblasts analyzed by fluorescence and atomic force microscopy. *Biomehcan. Model Mechanobiol* 5: 263-272.

A.R. Kirby, D.J. Fyfe, M.L. Parker et al. (1998). Structural studies on human coleretal adenocarcinoma HT29 cells by atomic force microscopy, transmission electron microscopy and scanning electron microscopy. *Probe Microscopy.* 1: 153-162.

S. Knutton, M.C.B.Summer, C.A.Pasternack (1975).Role of microvilli in surface changes of synchronized P815Y mastocytoma cells. *J. Cell Biol*. 66: 568-576.

R.N. Kolesnick, F.M. Goni, A. Alonso (2000). Compartmentalization of ceramide signaling. Physical foundation and biological effects. *J. Cell Physiol.* 184: 285-300.

O.N. Kovbasnjuk, K.R. Spring (2000). The apical membrane glycocalyx of MDCK cells. *Membrane Biol.* 176:19-29.

S. Krüger, D. Krüger, A. Janshoff (2004). Scanning force microscopy based rapid force curve acquisition on supported lipid bilayer: experiments and simulations using pulsed force mode. *Chem. Phys. Chem.* 5: 989-997.

M. Kuchařová et al. (2007). Viscoelasticity of biological materials- measurement and practical impact on biomedicine. *Physiol. Res.* 533-537.

J. Kwik, S. Boyle, D. Fooksman, L. Margolis, M.P. Sheetz, M. Edidin (2003). Membrane cholesterol, lateral mobility,, and the phosphatidylinositol 4,5-bisphosphate-dependent organization of cell actin. *PNAS*. 100: 13964-13969.

C. Le Grimellec et al. (1998). Imaging of the surface of living cells by low-force contact-mode atomic force microscopy. *Biophys. J.* 75: 695-703.

L.D. Landau, E.M. Lifshitz (1970). Theory of Elasticity. Pergamon Press, Oxford.

K. Lange J. Gartzke (2001). Microvillar cell surface as a natural defense system against xenobiotics: a new interpretation of multidrug resistance. *Am. J. Physiol*. 281: 369-385.

J. Lange, K. Schlipes, K. Lange, E. Knoll-Köhler (1996). Activation of calcium signaling in isolated rat hepatocytes is assocated with shape changes of MV. *Exp. Cell Res.* 234: 486-497.

P.A. Loomis et al. (2003). Espin cross-links cause the elongation of microvillus-type parallel actin bindles *in vivo*. *J. Cell Biol.* 163: 1045-1055.

B. Lorenz, I. Mey, S. Steltenkap, T. Fine, C. Rommel, M.M. Müller, A. Maiwald, J.Wegener, C. Steinem, A. Janshoff, (2009). Elasticity mapping of pore-suspending native cell membranes. *Small* 5(7): 832-838.

J.A. Lundbaek, P. Birn, A.J. Hansen, O.S. Andersen (1996). Membrane stiffness and channel function. *Biochemistry.* 35:3825–3830.

S.N. Maganov, D.H. Reneker (1997). Characterization of polymer surfaces with atomic force microscope. *Annu. Rev. Mater. Sci.* 27: 175-222.

R.E. Mahaffy et al. (2004). Quantitative analysis of the viscoelastic properties of thin regions of fibroblasts with atomic force microscopy. *Biophys. J.* 86: 1777-1793.

A. Mallavarapu, T. Mitchison (1999). Regulation of cell contraction and membrane ruffling by distinct signals in migratory cells. *J. Cell Biol.* 146: 1097-1106.

W.D. Marcus, R.M. Hochmuth (2002). Experimental studies of membrane tethers formed from human neutrophils. *Ann. Biomed. Eng*. 1273-1280.

E.N. Marieb (2000). *Human anatomy and physiology*.B. Cummnings, 5th edition.

C.J. Marrifield, D. Perrais, D. Zenisek (2005).Coupling between clathrin-coated-pit invaginaion, cortactin recruitment, and membrane scission observed in live cells.*Cell.* 121: 593-606.

O. Marti et al. (1988). Atomic force microscopy of an organic monolayer. *Science.* 239(4835): 50-52.

A.B. Mathur, A.M. Collinsworth, W.M. Reichert, W.E. Kraus (2001). Endothelial, cardiac muscle and skeletal muscle exhibit different viscous and elastic properties as determined by atomic force microscopy. *Biomech. J*. 34:1545-1553.

K.S. Matlin, M.J. Caplan (1992). Epithelial cell structure and polarity. *The Kidney: Physiology and pathophysiology.* D.W. Seldin and G. G.iebisch, editors. Raven Press, New-York. 447-473.

J.A. McAteer, G.S. Dougherty, K.D. Jr. Gardner, A.P. Evan (1986). Scanning electron microscopy of kidney cells in culture: surface features of polarized epithelia. *Scan. Electron. Microsc.* 3: 1135-1150.

H.T. McMahon, J.L. Gallop (2005) Membrane curvature and mechanisms of dynamic cell membrane remodeling. *Nature*. 438: 590-596.

D. Meder, A. Shevchenko, K. Simons, J. Füllekrug (2005). GP135/ podocalyxin and NHERF-2 participate in the formation of a preapical domain during polarization of MDCK cells. *J. Cell Biol*. 168: 303-313.

G. van Meer, K. Simons (1988). Lipid polarity and sorting in epithelial cells. *J. Cell Biol*. 36: 51-58.

A.H. Merrill et al. (2001). Sphingolipid metabolism: roles in signal transduction and disruption by fumonisins. *Environ. Health Perspect.* 109: 283-289.

V.J. Morris, A.R. Kirby, A.P. Gunning (1999). *Atomic Force Microscopy for Biologists.* Imperial College Press, London.

D.J. Müller, Y.F. Dufrêne (2008). Atomic force microscopy as a multifunctional molecular toolbox in nanobiotechnology. *Nat. Nanotechnol.* 3: 261-269.

D.J. Müller, A. Engel (2007). Atomic force microscopy and spectroscopy of native membrane proteins. *Nat. Protoc.* 2: 2191-2197.

D.J. Müller, D. Fotiadis, A. Engel (1998). Mapping flexible protein domains at subnanometer resolution with the atomic force microscope. *FEBS LETT.* 430: 105-111.

D.J. Müller, D. Fotiadis, S. Scheuring, S.A. Müller, A. Engel (1999). Electrostatically balanced subnanometer imaging of biological specimens by atomic force microscope. *Biophys. J.* 76: 1101-1111.

D.J. Müller, J. Helenius, D. Alsteens, Y.F. Dufrêne (2009). Force probing surfaces of living cells to molecular resolution. *Nature Chem. Biol*. 5: 383-386.

D. Needham, R.S. Nunn (1990). Elastic deformation and failure of lipid bilayer membranes containing cholesterol. *Biophys. J.* 58: 997-1009.

W.J. Nelson, P.J. Veshnock (1986). Dynamics of membrane-skeleton (fodrin) organization during development of polarity in Madin-Darby canine kidney epithelial cells. *J. Cell Biol.* 103: 1751-1765.

M.V. Nermut (1989). Strategy and tactics in electron microscopy of cell surfaces. *Electron Microsc Rev*. 171-196.

D. Norouzi, M.M. Müller, M. Deserno (2006). How to determine local elastic properties of lipid bilayer membranes from atomic force microscope. *Phys. Rev.* 74: 06914.

F.M. Ohnesorge et al. (1997). AFM review study on Pox viruses and living cells. *Biophys. J.* 73: 2183-2194.

G.K., Ojakian, R. Schwimmer (1998). The polarized distribution of an apicalcell surface glycoprotein is maintained by interactions with the cytoskeleton of Madin-Darby canine kidney cells. *J. Cell Biol*. 107:2377-2387.

G. Oster (1989). Cell motility and tissue morphogenesis. In: *Cell Shape: Determinants, Regulation, and Regulatory Role*. Ed. W. Stein and F. Bronner New York:Academic Press. 33-61.

W. Osten (2007). *Optical inspection of microsystems.* CRC Press.

P.J. de Pablo, I.I. Schaap, F.C. MacKintosh, C.F. Schmidt (2003). Deformation and collapse of microtubles on the nanometer scale. *Phys. Rev. Lett.* 91: 098101.

P. Pacini, G.E. Orlandini, A.F. Holstein (1980). Scanning electron microscopy of the human male genital tract. *Bull. Assoc. Anat. (Nancy).* 64:561-566.

R. Parthasarathy, J.T. Groves (2007). Curvature and spatial organization in biological membranes. *Soft Matter*. 3(1): 24-33.

A.E. Pelling, B.M. Nicholls, Y.R. Silberberg, M.A. Horton (2007). Approaches for investigating mechanobiological dynamics in living cells with fluorescence and atomic force microscopy, in Méndez-Vilas, A. and Díáz, *J. Eds. Modern Research and Educational Topics on Microscopy.* Formatex, pg. 3-10.

J.-B. Perez, K.L. Martinez, J.M. Segura, H. Vogel (2006). Supported cell-membrane sheets for functional fluorescence imaging of membrane proteins. *Adv. Funct. Mater.* 16: 306-312.

J.B. Pethica, W.C. Oliver (1987). Tip surface interactions in STM and AFM. *Physica Scripta* T19: 61-66.

J.B. Pethica, A.P. Sutton (1988). On the stability of a tip and flat at very small separations. *J. Vac. Sci. Technol.* A6: 2490-2494.

J.L. Podolski, T.L. Steck (1988). Association of deoxyribonuclease I with the pointed ends of actin filaments in human red blood cell membrane cytoskeleton.*J. Biol. Chem.* 263: 638-645.

K. Poole, D. Meder, K. Simons, D. Müller (2004). The effect of raft lipid depletion on microvilli formation in MDCK cells, visualized by atomic force microscopy. *FEBS Lett.* 565: 53-58.

J. Pourati, A. Maniotis, D. Spiegel, J.L. Schaffer, J.P. Butler, J.J. Fredberg, D.E. Ingber, D. Stamenovic, N. Wang (1998). Is cytoskeletal tension a major determinant of cell deformability in adherent endothelial cells? *Am. J. Cell Physiol.* 274: C1283-C1289.

H.A. Praetorius, K.R. Spring (2001). Removal of the MDCK cell primary cilium abolishes flow sensing. *J. Membrane Biol.* 191: 69-76.

E.M. Puchner et al. (2008). Mechanoenzymatics of titin kinase. *Proc. Natl. Acad. Sci. USA.* 105: 13385-13390.

M. Radmacher, J.P. Cleaveland, M. Fritz, H.G. Hansama, P.K. Hansama (1994). Mapping interaction forces with the atomic force microscope. *Biophys. J.* 66: 2159-2165.

D. Raucher, M.P. Sheetz (2001). Phospholipase C activation by anesthetics decreases membrane-cytoskeleton adhesion. *J. Cell Sci.* 114: 3759-3766.

D. Raucher, M.P. Sheetz (2000). Cell spreading and lamellipodial extension rate is regulated by membrane tension. *J. Cell Biol.* 148: 127-136.

D. Raucher, M.P. Sheetz (1999). Characteristics of a membrane reservoir buffering membrane tension. *Biophys. J.* 77: 1992-2002.

A. del Rio et al. (2009). Stretching single talin rod molecules activates vinculin binding. *Science*. 323: 638-641.

F. Rosso, A. Giordano, M. Barbarisi, A. Barbarisi (2004). From cell-ECM interactions to tissue engineering. *Cell Phys. J*. 199: 174-180.

A. Roters, D. Johannsmann (1996). Distance dependent noise measurements in scanning force microscopy. *J. Phys. Condens. Matter.* 8: 7561.

C. Rotsch, F. Braet, E. Wisse, M. Radmacher (1997). AFM imaging andelasicity measurements on living rat liver machrophages. *Cell Biol. Int.* 21: 685-696.

C. Rotsch, M. Radmacher (2000). Drug-induced changes of cytoskeletal structure and mechanics in fibroblasts: an atomic force microscopy study. *Biophys J*. 78:520–535.

Y. Sambuy, E. Rodriguez-Boulan (1988). Isolation and characterization of the apical surface of polarized Madin-Darby canine kidney epithelial cells. *Proc. Natl. Acad. Sci. USA.* Cell Biology 85: 1529-1533.

D. Semwogerere, E.R. Weeks, *Confocal microscopy*, *Encyclopedia of biomaterials and biomedical enginnering* (2005).

Z. Shao, J. Mou, D.M. Czajkowsky, J. Yang, J.-Y. Yuan (1996). Biological atomic force microscopy: what is achieved and what is needed. *Advan. Phys*. 45: 1-86.

A.J. Shaw (2002). *Epithelial cell culture: A practical approach.* Oxford University Press.

T. Shepard, H.W. Park (1994). Neural plate microvillus lengthening in rat embryos grown in various concentrations of glucose and further study of the mechanism. *Teratology.* 50: 340-347.

K. Simons, E. Ikonen (1997). How cells handle cholesterol. *Nature*. 387: 569-572.

K. Simons, A. Wandinger-Ness (1990). Polarized sorting in epithelia. *Cell.* 62:207-210.

S. Singer, G. Nicolson (1972). The fluid mosaic model of the structure of cell membranes. *Science*. 175:720-731.

I.N. Sneddon (1965). The relation between load and penetration in the axissymmetric boussinesq problem for a punch of arbitrary profile. *Int. J. Eng. Sci*. 3:47-57.

D. Stamenović, D.E. Ingber (2002). Models of cytoskeletal mechanics and adherent cells. *Biomechanics and Modellind in Mechanobilogy.* 1: 95-108.

D. Stamenović, N. Wang, D.E. Ingber (2006). *Principles of Cellular Engineering*: Tensegrity models and cell-substrate interactions, 4: 81-101.

S. Steltenkamp (2006). Mechanische Eigenschaften von freitragenden artifiziellen und nativen Membranen. PhD thesis.

S. Steltenkamp, C. Rommel, J. Wegener, A. Janshoff (2006). Membrnae stiffness of animal cells challenged by osmotic stress. *Small*. 2: 1016-1020.

S. Steltenkamp, M.M. Müller, M. Deserno, C. Hennesthal, C. Steinem, A. Janshoff (2006). Mechanical properties of pore-spanning lipid bilayers probed by atomic force microscopy. *Biophys. J*. 91:217-226.

T. Sugitate, T. Kihara, X.-U. Liu, J. Miyake (2009). Mechanical role of the nucleus in a cell in terms of elastic modulus. *Curr. Appl. Phys.* (in press).

V.L. Sukhorukov, W.M. Arnold, U. Zimmermann (1993). Hypotonically induced changes in the plasma membrane of cultured mammalian cells. *J. Membr. Biol.*132: 27-40.

M. Sun, N. Northup, F. Marga, T. Huber, F.J. Byfield, I. Levitan, G. Forgacs (2007). The effect of cellular cholesterol on membrane cytoskeleton adhesion. *J. Cell Sci.* 120: 2223-2231.

N.J. Tao, N.M. Lindsay, S. Lees (1992). Measuring the microelastic properties of biological material. *Biophys. J.* 63:1165-1169.

N. Unwin (2005). Refined structure of the nicotinic acetylcholine receptor at 4Å resolution. *J. Mol. Biol.* 346: 967-989.

O.I. Wagner et al. (2007). Softness, strength and self-repair in intermediate filament networks. *Exp. Cell Res.* 313(10): 2228-2235.

H.B. Wang, M. Dembo et al. (2000). Substrate flexibility regulates growth and apoptosis of normal but not transformed cells. *Am. J. Physiol. Cell Physiol.* 279(5): C1345-C1350.

N. Wang, I.M. Tolic-Norrelykke (2002). Cell prestress .I. Stiffness and prestress are closely associated in adherent contractile cells. *Am. J. Physiol. Cell Physiol.* 282(3): C606-C616.

T.P. Weihs, Z. Nawaz, S.P. Jaruis, B. Pethica (1991). Limits of imaging resolution for atomic forcemicroscopy of molecules. *Appl. Phys. Lett.* 59: 3536

A.L. Weisenhorn, M. Khorsandi, S. Kasas, V. Gotzost, H.-J. Butt (1993). Deformation and height anomaly of soft surfaces studied with an AFM. *Nanotech*. 4: 106-113.

H.W. Wu, T. Kuhn, M.T. Moy (1998). Mechanical properties of L929 cells measured by atomic force microscopy: effects of anticytoskeletal drugs and membrane crosslinking. *Scanning* 20:389–397.

X. Xu, E. London (2000). The effect of sterol structure on membrane lipid domains reveal how cholesterol can induce lipid domain formation. *Biochem*. 39: 843-849.

G. Xu, J.Y. Shao (2008). Human neutrophil surface protrusion under a point load: location independence and viscoelasticity. *Am. J. Phsiol. Cell Physiol*. 295: C1434-1444.

J. Yang et al. (1993). Promises and problems of biological atomic force microscopy. *J. Microscopy.* 171: 183-189.

P. L. Yeagle (2005). *The structure of biological membranes.* CRC Press, 2nd edition.

P. L. Yeagle (1985). Cholesterol and the cell membrane. *Biochim. Biophys. Acta.* 822: 267-287.

C. Yeaman, K.K. Grindstaff, W.J. Nelson. (1999). New perspectives on mechanisms involved in generating epithelail cell polarity. *Physiol. Rev*. 79: 73-98.

E.K.F. Yim, K.W. Leong (2005b). Significance of synthetic nanostructures in dictating cellular response. *Nanomedicine: Nanotechnology, Biology and Medicine* 1: 10-21.

H.L.Yin, T.P. Stossel (1979). Control of cytoplasmic actin gel-sol transformation by gelsolin, a calcium-dependent regulatory protein. *Nature*. 281, 583−586.

B.K. Yoder (2007). Role of primary cilia in the pathogenesis of poly-cystic kidney disease. *J. Am. Soc. Nephrol.* 18: 1381-1388.

D. Zahor, A. Radko, R. Vago, L.A. Gheber (2007).Organization of mesenchymal stem cells is controlled by micropatterned silicon substrates. *Materials Science & Engineering.* C 27: 117-121.

A. Zelenskaya, J. Boutet de Monvel, D. Pesen, M. Radmacher, J.-H. Hoh, M. Ulfendahl (2005). Evidance for a highly elastic shell-core organizaion of cochlear outer hair cells by local membrane indentation. *Biophys. J*. 88: 2982-2993.

G. Zhang (2005). Evalulating the viscoelastic properties of biological tissues in a new way. *J. Musculoskelet Neuronal Interact*. 5(1): 85-90.

C.Y. Zhang, Y.W. Zhang (2007). Effects of membrane pre-stress and intrinsic viscoelasticity on nanoindentation of cells using AFM. *Phil. Magaz.* 87 (23): 3415-3435.

U. Ziegler, A. Vinckier, P. Kernen, D. Zeisel, J. Biber, G. Semanza, H. Murer, P. Groscurth (1998). Preparation of basal cell membranes for scanning probe microscopy. *FEBS Lett.* 432(2): 179-184.

ABBREVIATIONS

AFM: Atomic Force Microscope

PBS: Phosphate Buffered Saline

CLSM: Confocal Laser Scanning Microscope

$DiIC_{18}$: 1,1′-dioctadecyl-3,3,3′,3′-tetramethylindocarbocyanine

DNase I: Deoxyribonuclease I

ECM: Extra Cellular Matrix

F-Actin: Filamentous Actin

FCS: Fetal Calf Serum

G-Actin: Globular Actin

GDA: Glutardialdehyde

gp135: glycoprotein 135

mAb: Monoclonal Antibody

MDCK II: Madin Darby Canine Kidney strain II

MEM: Modified Eagle Medium

SEM: Scanning Electron Microscope

PBS: Phosphate Buffer Salt

PDL: Poly-D-Lysine

PFA: Paraformdialdehyde

PFM: Pulse Force Mode